TIME-RESOLVED FLOWFIELD MEASUREMENTS IN A

TURBINE STAGE

by

JEFFREY LYNN HOLT
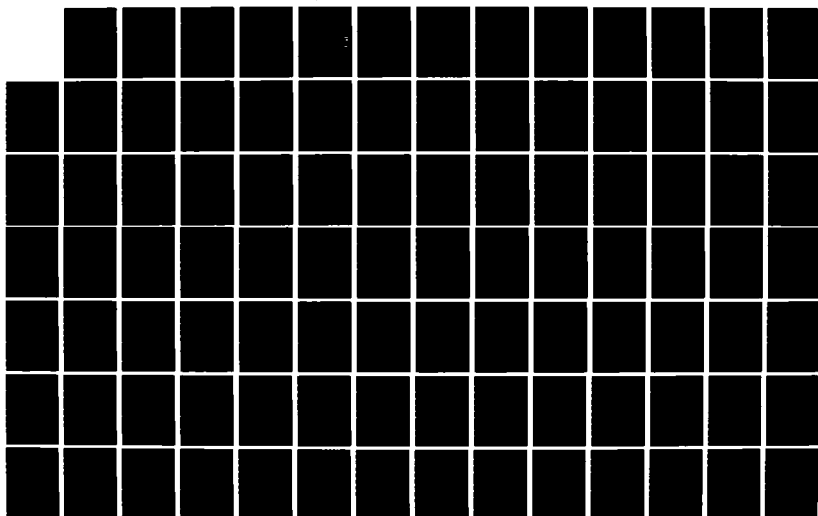
B.S., United States Air Force Academy (1980)

SUBMITTED IN PARTIAL FULFILLMENT

OF THE REQUIREMENTS OF THE

DEGREE OF

MASTER OF SCIENCE

IN AERONAUTICS AND ASTRONAUTICS

at the

MASSACHUSETTS INSTITUTE OF TECHNOLOGY

June 1985

© Massachusetts Institute of Technology, 1985

Signature of Author _____
Department of Aeronautics and Astronautics
June 3, 1985

Certified by _____
Professor Alan H. Epstein
Thesis Supervisor
Department of Aeronautics and Astronautics

Accepted by _____
Professor Harold Y. Wachman
Chairman, Departmental Graduate Committee

This do[cument has been approved]
for pu[blic release and sale; its]
distribu[tion is unlimited.]

REPORT DOCUMENTATION PAGE	READ INSTRUCTIONS BEFORE COMPLETING FORM

1. REPORT NUMBER	2. GOVT ACCESSION NO.	3. RECIPIENT'S CATALOG NUMBER
AFIT/CI/NR 85-77T	AD-A158092	

4. TITLE *(and Subtitle)*	5. TYPE OF REPORT & PERIOD COVERED
Time-Resolved Flowfield Measurements in a Turbine Stage	THESIS/DISSERTATION
	6. PERFORMING ORG. REPORT NUMBER

7. AUTHOR(s)	8. CONTRACT OR GRANT NUMBER(s)
Jeffrey Lynn Holt	

9. PERFORMING ORGANIZATION NAME AND ADDRESS	10. PROGRAM ELEMENT, PROJECT, TASK AREA & WORK UNIT NUMBERS
AFIT STUDENT AT: Massachusetts Institute of Technology	

11. CONTROLLING OFFICE NAME AND ADDRESS	12. REPORT DATE
AFIT/NR WPAFB OH 45433	June 1985
	13. NUMBER OF PAGES
	163

14. MONITORING AGENCY NAME & ADDRESS(If different from Controlling Office)	15. SECURITY CLASS. (of this report)
	UNCLASS
	15a. DECLASSIFICATION/DOWNGRADING SCHEDULE

16. DISTRIBUTION STATEMENT *(of this Report)*

APPROVED FOR PUBLIC RELEASE; DISTRIBUTION UNLIMITED

17. DISTRIBUTION STATEMENT *(of the abstract entered in Block 20, if different from Report)*

18. SUPPLEMENTARY NOTES

APPROVED FOR PUBLIC RELEASE: IAW AFR 190-1

LYNN E. WOLAVER
Dean for Research and
Professional Development
5 AUG 1985 AFIT, Wright-Patterson AFB OH

19. KEY WORDS *(Continue on reverse side if necessary and identify by block number)*

20. ABSTRACT *(Continue on reverse side if necessary and identify by block number)*

ATTACHED

A-1

DD _{1 JAN 73} FORM 1473 EDITION OF 1 NOV 65 IS OBSOLETE

UNCLASS

85 8 13 085

AFIT RESEARCH ASSESSMENT

The purpose of this questionnaire is to ascertain the value and/or contribution of research accomplished by students or faculty of the Air Force Institute of Technology (AU). It would be greatly appreciated if you would complete the following questionnaire and return it to:

AFIT/NR
Wright-Patterson AFB OH 45433

RESEARCH TITLE: Time-Resolved Flowfield Measurements in a Turbine Stage

AUTHOR: Jeffrey Lynn Holt

RESEARCH ASSESSMENT QUESTIONS:

1. Did this research contribute to a current Air Force project?

( ) a. YES   ( ) b. NO

2. Do you believe this research topic is significant enough that it would have been researched (or contracted) by your organization or another agency if AFIT had not?

( ) a. YES   ( ) b. NO

3. The benefits of AFIT research can often be expressed by the equivalent value that your agency achieved/received by virtue of AFIT performing the research. Can you estimate what this research would have cost if it had been accomplished under contract or if it had been done in-house in terms of manpower and/or dollars?

( ) a. MAN-YEARS _____   ( ) b. $_____

4. Often it is not possible to attach equivalent dollar values to research, although the results of the research may, in fact, be important. Whether or not you were able to establish an equivalent value for this research (3. above), what is your estimate of its significance?

( ) a. HIGHLY   ( ) b. SIGNIFICANT   ( ) c. SLIGHTLY   ( ) d. OF NO
      SIGNIFICANT   SIGNIFICANT   SIGNIFICANCE

5. AFIT welcomes any further comments you may have on the above questions, or any additional details concerning the current application, future potential, or other value of this research. Please use the bottom part of this questionnaire for your statement(s).

NAME   GRADE   POSITION

ORGANIZATION   LOCATION

STATEMENT(s):

AFIT/NR
WRIGHT-PATTERSON AFB OH 45433

OFFICIAL BUSINESS
PENALTY FOR PRIVATE USE. $300

NO POSTAGE
NECESSARY
IF MAILED
IN THE
UNITED STATES

BUSINESS REPLY MAIL
FIRST CLASS   PERMIT NO. 73236   WASHINGTON D.C.

POSTAGE WILL BE PAID BY ADDRESSEE

AFIT/ DAA
Wright-Patterson AFB OH 45433

TIME-RESOLVED FLOWFIELD MEASUREMENTS IN A TURBINE STAGE

by

JEFFREY LYNN HOLT

Submitted to the Department of Aeronautics and Astronautics
on June 3, 1985 in partial fulfillment of the
requirements for the degree of Master of Science in
Aeronautics and Astronautics

ABSTRACT

Time-resolved flowfield measurements for a 0.5-meter diameter, high work transonic turbine have been completed in the MIT Turbine Blowdown Facility (TBF). The measurements were taken: to determine the blade-to-blade total temperature profile for comparison with predictions from the Euler turbine equation; to determine the effect of using time-averaged pressures to calculate turbine performance; and to provide a complete set of time-resolved turbine stage data. A preliminary objective of the work (given a 6 kHz blade passing frequency) was to determimine the frequency response characteristics of the instrumentation employed to make the flowfield measurements. A shock tube was built for this purpose.

The measurements were taken with high-frequency response instrumentation including a dual-hot-wire aspirating probe, a 'four-way' angle probe, and two cobra head total pressure probes incorporating silicon diaphragm pressure transducers (Kulite models XCQ-093 and XCQ-062). The probes were positioned 0.5 axial chord lengths downstream of the turbine midspan and traversed circumferentially. The properties measured include total temperature, total pressure, Mach number, and tangential flow angle. Experiments were done at 125%, 100% and 80% corrected speeds.

The aspirating probe is found to have a natural frequency of 15.5 kHz in the test gas with a damping ratio of 0.36; the angle probe a characteristic frequency of 45 kHz with a settling time of 18 usec. Both results are satisfactory for application in the TBF. The measured total temperature profile shows a peak-to-peak variation of 65 C (20%) and a characteristic frequency twice that of the blade passing frequency. The peak total temperature is out of phase with the peak total pressure, and suggests hot wakes. The predicted temperature profile, made with the Euler turbine equation and angle probe data, varies at the blade passing frequency only and is more in phase with the pressure. Further, it is DC shifted upward 20% from the measured profile. The error associated with using the time-averaged pressure from a standard pitot probe (instead of the actual time-resolved signal) to calculate turbine adiabatic efficiency is shown to be 0.25%.

Thesis Supervisor: Dr. Alan H. Epstein
Title: Associate Professor of Aeronautics and Astronautics

ACKNOWLEDGEMENTS

BIOGRAPHICAL NOTE

Jeffrey Lynn Holt was born January 28, 1958 in Fairborn, Ohio to Franklin and Jessie Holt, and is their second of four sons. After graduation in June 1976 from Plymouth High School in Plymouth, Ohio as valedictorian, he entered the United States Air Force Academy. There, his studies emphasized Aeropropulsion and, at the conclusion of his senior year, he was selected as one of the two top aeronautics graduates in Thermodynamics and Propulsion. Upon graduation from the Academy in May 1980, he was commissioned into the United States Air Force and assigned to the USAF Wright Aeronautical Laboratories, Aero Propulsion Laboratory at Wright-Patterson AFB in Dayton, Ohio. At the Aero Propulsion Laboratory, he served as the Air Force project engineer for a program employing a short-duration shock tunnel facility to measure heat transfer distributions in an aircraft turbine stage. In June 1983, he completed his tour at the Aero Propulsion Laboratory and entered the Massachusetts Institute of Technology under the supervision of Dr. Alan H. Epstein.

Permanent address: 223 Plymouth Street
                    Plymouth, Ohio 44865

TABLE OF CONTENTS

LIST OF FIGURES

speed channels can be multiplexed onto 8 of the high speed channels. Programmable multispeed clocks control the data sampling rate over the test time. During the test, the data are stored in a 32 million byte solid state random access memory. After the test, the data are transmitted to a DEC PDP 11/70 for reduction, analysis, and storage.

In summary, the TBF is a versatile, rigorously scaled vehicle for investigating the performance and flowfield characteristics of large gas turbines. The facility is particularly well suited for the study of unsteady turbine flowfield phenomena, especially as outlined in the present works' objective statement. The instrumention necessary to investigate the turbine flowfield are now discussed.

2.2 Instrumentation Description, Performance, and Calibration

The aspirating probe, angle probe, silicon diaphragm pressure transducers, and instrumentation traverser are discussed in the following sections. The physics of operation, performance characteristics, calibration procedures, and data reduction schemes are addressed for each probe. First, however, the temporal and spatial resolution aspects of the instrumentation are discussed relative to the characteristic times and lengths associated with the test turbine.

2.2.1 Instrumentation Spatial and Temperoral Resolution

Blade passing frequency of the test turbine in the TBF is slightly higher than 6 kHz when operated at 100% corrected

section Reynolds number. An argon-freon-12 gas mixture
(freon-12 mass fraction of 51%) is used as the facility test
gas and was chosen to accommodate turbine scaling. This test
gas possesses a low gas constant and therefore a
correspondingly low sonic speed. As such, the design point
corrected speed (tip Mach number) can be achieved with
relatively low mechanical speeds. This in turn lowers the
minimum frequency response requirements of the
instrumentation.

The design point corrected speed and mass flow for this
turbine are achieved with initial supply tank conditions of
478 K temperature and 4.2 atm pressure. The initial rotor
speed is approximately 100 rev/sec. Both the pressure and
temperature drop isentropically as the supply tank 'blows
down' during the test, but the mechanical speed of the rotor
is controlled by an eddy current brake to maintain the 100%
value of corrected speed. The eddy brake serves to absorb the
energy extracted from the flow by the turbine during the test.

Instrumentation access is provided by three 13 cm wide
windows spaced 120 degrees apart around the outer case of the
turbine. Each window extends from upstream of the vane row to
11 cm downstream of the rotor. A schematic of the test
section indicating the location of the access ports is shown
in Figure 2-2. The turbine blade and vane dimensions are also
indicated.

The TBF utilizes a digital data acquisition system
designed for 100 high speed, 12 bit channels with maximum
sampling rates of 200 kHz per channel. Eight groups of 16 low

CHAPTER 2

THE EXPERIMENT -- FACILITY, INSTRUMENTATION, AND TECHNIQUE

A brief description of the Turbine Blowdown Facility (TBF) is given in this chapter. Facility setup, the test turbine, and the data acquisition system are all addressed. The instrumentation employed for the experiments, including a dual-hot-wire aspirating probe, a four-pressure-transducer angle probe, silicon diaphragm pressure transducers, and a probe traverser, are discussed in detail along with their respective physics of operation, performance characteristics, and calibration procedures. Finally, the facility operation procedures and test techniques are reviewed.

2.1 The Facility, Test Turbine, and Data Acquisition System

The TBF is a short duration test facility presently configured with a 0.5 m diameter high work, transonic turbine of Rolls-Royce Limited design and manufacture. Figure 2-1 is a schematic of this facility. The TBF rigorously simulates actual turbine operating conditions over a test time of approximately 0.4 seconds. Design, construction and operational aspects of the facility are fully detailed in [1] so only a few relevant characteristics are noted here.

The facility is essentially composed of a large supply tank separated from the test turbine and dump tank by a fast acting valve. The supply tank is heated by an oil jacket to achieve the proper temperature ratios in the test section. The supply tank pressure is set to achieve the desired test

the literature with emphasis on the three-dimensionality and unsteady nature of the turbine flowfield. Features of the turbine flowfield described above, as well as the results of the work outlined, will be referred to again throughout this thesis.

of the rotor airfoils and upstream vanes. In this regard, they describe two flow regimes corresponding to 'maximim interaction' or 'minimum interaction' betweem the rotor leading edges and upstream vane wakes. In the case of maximum interaction, the vane wakes and rotor wakes are said to merge with the consequence of leaving the blade passage uniform except for two strong secondary flow vortices. In the minimum interaction case, the vane wakes are said to enter the blade passage, thereby increasing its non-uniformity and masking to some degree the secondary flow vortices.

In the paper above, a nondimensional parameter in the form of a Strouhal number is used to indicate the degree of interaction between the vane and rotor flowfield, and will be borrowed for use in Chapter 4. This parameter is defined as follows:

$$S = \frac{U}{t} \frac{bx}{Cx} \qquad [1.1]$$

where S is a reduced frequency or Strouhal number, U the rotor speed, t the vane gap, bx the rotor axial chord, and Cx the throughflow velocity. The term t/U is a time scale associated with the blade traversal of the upstream vane gap. The term bx/Cx is a time scale associated with the passage of fluid through the rotor. The ratio of these terms, S, thus gives an indication of the number of upstream wakes in the rotor passage at any time.

In summary, the purpose of this section has been to give a limited overview of recent turbine flowfield measurements in

near the hub. The analyses presented in these papers can essentially be extended to wake transport phenomena in turbines.

Binder et al. [6] employ a Laser-Two-Focus velocimeter to make flowfield measurements and show that the wake fluid is highly turbulent. Hodson [7] mounts hot wires on a turbine rotor itself to measure the time dependent velocity field within the rotor passage and concludes that the rotor unsteadiness in dominated by the convection of the wake fluid through the rotor. Both papers tend to show that wake generated unsteadiness, at least at the midspan, can be explained with the wake cutting and migration theories mentioned above. Oldfield and Doorly [8] show that in addition to the wake, shock-wave passing can be a major source of flow unsteadiness and may also affect the rotor exit blade-to-blade profile via the boundary layer. Their Schlieren photographs indicate the upstream wakes migrate to the blade suction side as they pass through the blade row, as predicted from the results of [4].

Finally, one of the most complete sets of turbine flowfield data is given by Sharma, Butler, Joslyn, and Dring [9]. They give profiles of turbulent energy, total pressure, static pressure, absolute velocity magnitude, and radial and circumferential flow angle taken downstream of both the vane and blade row. They show that the vane exit flowfield is steady but dominated by large Reynolds stresses in the wake regions. The rotor exit flowfield, in contrast, was found to be highly unsteady and dependent upon the relative positioning

It is clear from the discussion above that the turbine flowfield is exceedingly complex. In this thesis, however, we are interested only in mapping the blade-to-blade flowfield properties at the rotor exit midspan and, therefore, unsteadiness associated with the wake should be the most notable characteristic of the measurements. With this in mind, some recent turbine and relevant compressor flowfield measurements in the literature are now summarized.

The kinematic analysis presented by Kerrebrock and Mikolajczak [4] is a milestone toward understanding the effect of upstream wakes on the flow inside blade passages. They develop the concept of a 'slip velocity' in a transonic compressor to show how the wake fluid does not mix with the inviscid core fluid but, rather, is transported relative to the inviscid fluid as it is convected through the blade passage. The result, which is well supported by experiment, is a redistribution of stagnation enthalpy across the blade passage and is characterized by an excess of total temperature in the stator wakes. This same phenomena, as shown in Figure 1-1, will occur in a turbine except that the wake will be transported toward the suction side of the airfoil rather than the pressure side as in the compressor. Epstein and Ng [5] have extended the analysis of [4] to include quasi-three dimensional effects of the wakes. In particular, they show that the relative flow angle is not necessarily uniform through the wake and this, coupled with the wakes three-dimensionality, results in the rotor wake having a lower total temperature near the tip and higher total temperature

that include full-stage flowfield measurements and to the best of the author's knowledge, none which offer high-frequency response temperature and pressure measurements. So ostensibly, the temperature and pressure measurements given later in this thesis are the first such published.

As a common theme, the published turbine data reveal a flowfield dominated by secondary flows and unsteadiness, even in the rotor frame of reference [2]. The variety of secondary flow features serves as an example of this complexity: horseshoe vortices, formed by the rolling up of the endwall boundary layer at the leading edge of a turbine blade or vane; passage vortices, which consist of a leg of the horseshoe vortex that has migrated to the suction side of the airfoil as it is convected through the passage; and corner vortices, which rotate in the opposite sense of the passage vortex and are located always in the endwall/suction side corner of the passage [3]. Additionally, there are tip vortices in the rotor due to blade tip leakage plus the added influence of a centrifigal body force. Finally, separation bubbles are common on both the vane and blade suction side at the airfoil leading edge. Unsteadiness is also typical of the turbine stage and, in fact, one can show that for a given particle in isentopic flow the flow must be unsteady for the stagnation enthalpy to change [2]. Hence, by their very nature, turbines possess unsteady flowfields. Summarized, turbine unsteadiness is associated with turbulence, potential field interactions between the blade rows, inlet profile from a combustor, and wakes generated by both the vanes and blades.

Measurements taken in this facility form the basis of the effort described in this thesis.

The objective of the work reported herein is to make time-resolved measurements of flowfield properties in a full-turbine stage. The measurements are taken: to determine the blade-to-blade total temperature profile for comparison with predictions from the Euler turbine equation; to determine the effect of using time-averaged pressures to calculate turbine performance; and to provide a new set of time-resolved turbine stage data. The properties measured include total temperature in particular, along with total pressure, static pressure, and radial and tangential flow angle. The measurements are time-resolved in the sense that data are taken at rates high enough to distinguish the blade-to-blade flowfield structure. To accomplish this objective, the frequency response characteristics of the instrumentation described above, primarily the dual-hot-wire aspirating probe and angle probe, and their suitability for making turbine flowfield measurements are investigated. The scope is limited to making measurements at three operating points: 125%, 100%, and 80% corrected speeds with their respective corrected mass flow conditions. The measurements are taken only at the rotor midspan but with circumferential translation.

1.2 Background

There are an enormous number of papers in the literature describing both measured and predicted flowfield characteristics in turbine cascades. But there are much fewer

matched similarity parameters, and which utilize high frequency response instrumentation, are much less common, however. Flowfield data from the latter facilities are very limited.

One such facility which rigorously simulates engine conditions (with a simulation capability extending to 40 atm inlet pressure and 2500 K turbine inlet temperature) has been recently developed, constructed, and tested at the Massachusetts Institute of Technology [1]. This facility operates as a short duration blowdown tunnel, having test times of approximately 0.4 seconds, and is configured with a 0.5 meter diameter, high work, transonic turbine designed and manufactured by Rolls-Royce Limited. High-frequency response instrumentation have also been developed and complement the utility of the MIT blowdown facility. These include a dual-hot-wire aspirating probe which yields a simultaneous measurement of flowfield total temperature and total pressure in the frequency range of DC to 21 kHz in air, and an angle probe incorporating four silicon diaphragm pressure transducers. The angle probe provides measurements of flowfield static pressure, total pressure and radial and circumferential flow angle and has a frequency response of DC to 45 kHz. Independent measures of total pressure can be made with cobra head impact probes. Together, the MIT blowdown facility coupled with the high-frequency response instrumentation provide a flexible vehicle for investigating the complex flowfield of aircraft gas turbines and extending the limited pool of turbine flowfield information.

CHAPTER 1

THE INTRODUCTION -- OBJECTIVE, SCOPE, AND BACKGROUND

This thesis deals with making time-resolved flowfield measurements in a full gas turbine stage. Properties measured include total temperature, total pressure, static pressure, Mach number, and tangential flow angle. In this Chapter, some motivation and background for the measurements are given. In Chapter 2, the test vehicle employed for the measurements, the MIT Turbine Blowdown Facility, and its high-frequency response instrumentation are described. Chapter 3 gives the design and operating procedures for a shock tube facility constructed to measure the frequency response characteristics of the instrumentation employed for the turbine measurements. In Chapter 4, the measurements taken in the turbine facility are presented and briefly analyzed. And finally, in Chapter 6, conclusions from the work accomplished are summarized.

1.1 Thesis Objective and Scope

The aircraft high pressure turbine flowfield is characteristically three-dimensional, unsteady, and compressible, hence making it exceedingly difficult to describe analytically. Accordingly, to refine performance or empiricize design codes, the turbine designer must rely on experiments to determine the structure of this spatially non-uniform flowfield. Turbine cascade data are relatively abundant since facility costs are low and the flowfield is benign compared to actual turbine operating environments. Facilities employing full-stage test turbines with rigorously

```
w    -   frequency in Hertz
wn   -   undamped natural frequency in Hertz
X    -   mole fraction
x    -   ellipse coordinate
y    -   ellipse coordinate
z    -   damping ratio
```

Greek

```
η    -   turbine adiabatic efficiency
μ    -   test gas viscosity
ρ    -   density
γ    -   ratio of specific heats
θ    -   absolute frame of reference
B    -   relative frame of reference
```

Superscript

```
'    -   reference variable, incompressible variable
```

Subscript

```
1    -   first component of binary gas mixture, angle
         probe transducer 1
2    -   second component of binary gas mixture, angle
         probe transducer 2
3    -   turbine inlet station, angle probe transducer 3
4    -   turbine exit station, angle probe transducer 4
i    -   refers to freestream value
n    -   refers to local value
θ    -   tangential direction
s    -   refers to static conditions
t    -   refers to total conditions
```

LIST OF SYMBOLS

A	-	ellipse semi-major axis; second order instrument response to step input, zero to final value
a	-	King's Law coefficient; second order instrument response to step input, final value to peak value
ac	-	aspirating probe channel area
a*	-	aspirating probe choked orifice area
B	-	ellipse semi-minor axis
b	-	King's Law coefficient
bx	-	rotor axial chord
C	-	aspirating probe calibration coefficient; sonic speed based on ambient conditions
CP	-	angle probe coefficient
Cx	-	rotor throughflow velocity
cp	-	specific heat at constant pressure
D	-	aspirating probe calibration coefficient; derivative with respect to time, d /dt
d	-	hot wire diameter
e	-	temperature coefficient of resistance
F	-	angle probe coefficient
f	-	undamped natural frequency in Hertz
H	-	angle probe coefficient
K	-	static sensitivity of second order instrument
KP	-	angle probe coefficient
k	-	test gas thermal conductivity; summation index
L	-	aspirating probe channel length
l	-	hot wire length
M	-	molecular weight; Mach number
Ma	-	absolute frame Mach number
Mr	-	relative frame Mach number
N	-	aspirating probe calibration exponent
NC	-	corrected speed
Nu	-	Nusselt number
n	-	King's Law exponent; summation index
P	-	pressure
Pavg	-	direct time-averaged pressure
Pbar	-	probe averaged pressure
Q	-	internal angle of ellipse
qi	-	input quantity of second order system
q0	-	output quantity of second order system
R	-	Gas constant
Rc	-	hot wire cold resistance
Re	-	Reynolds number
Rh	-	hot wire hot resistance, same as Rw
Rs	-	anemometer series resistance
Rw	-	hot wire operating resistance
r	-	hot wire recovery factor; turbine radius
S	-	reduced frequency or Strouhal number
T	-	temperature; period of oscillation
Tw	-	hot wire temperature
t	-	vane gap
U	-	rotor speed, fluid velocity
V	-	anemometer bridge output voltage; absolute frame velocity

LIST OF TABLES

speed. The wakes generated by turbine blades are thin, being on the order of twice the blade trailing edge thickness. In fact, data obtained by Joslyn, Dring and Sharma [9] suggest turbine blade wakes occupy less than 10% of the rotor blade spacing. Accordingly, to measure flowfield property variations in the region of the wake (or in some similarly small region where property gradients are large) the instrumentation employed must have frequency responses well above the blade passing frequency. In the present case, a frequency response of something greater than 6 kHz is the bottom limit for distinguishing blade-to-blade variations while ten times 6 kHz is necessary to distinguish property variations through a wake. Hence the temporal resolution of the instrumentation used is a critical item which one must reliably determine. For these reasons, a shock tube facility was designed and constructed to investigate the frequency response characteristics of the instrumentation used in the TBF. The shock tube design and operating procedures along with test results for the aspirating probe and angle probe are presented in Chapter 3.

Likewise, the spatial resolution of the instrumentation is critical since their characteristic dimensions are essentially the dimensions of the smallest flowfield structure measureable by that instrumentation. And as mentioned above, length scales associated with the blade-to-blade flowfield structure are relatively small, especially in the region of the wake. We would therefore like very small sensors and probes. The size of the aspirating probe and angle probe

relative to the TBF turbine blades and vanes are shown in Figure 2-3. The blade trailing edge span is 48.4 mm, the blade spacing is 27.9 mm, and trailing edge thickness is approximately 0.8 mm. The corresponding characteristic lengths of the aspirating probe and angle probe are 3.0 mm and 3.3 mm respectively. Since turbine wake thicknesses are on the order of twice the trailing edge thickness, we cannot distinguish internal wake flow structure with the probes at hand. We can however distinguish blade-to-blade structure since both probes occupy only 11%, or less, of the blade spacing. From here on we shall consider each probes spatial resolution acceptable for making measurements in the TBF.

2.2.2 The Dual-Hot-Wire Aspirating Probe

The aspirating probe provides a simultaneous measurement of total pressure and total temperature in an unsteady compressible flowfield. This probe, shcən in Figure 2-4, was developed to investigate the unsteady flowfield downstream of a transonic fan [10] and has the advantage of high frequency response. Its development and full description are detailed in [11]. Application of the aspirating probe to a turbine environment is a direct extension of its previous employment in a transonic compressor; however, certain aspects of the probe's performance differ between the two applications. In particular, the probe's resolution and frequency response are different. These differences stem from the varying test gases and flow conditions encountered with the respective component test facilities, along with choice of hot wire dimensions.

The aspirating probe as configured for application in the TBF is now described along with a review of its operating principles. Subsequently, the probe's performance characteristics, calibration procedures and results, and data reduction procedures are given.

2.2.2.1 Description and Physics of Operation

A complete description of the aspirating probe is given in [11] but is summarized here for reference. The aspirating probe consists essentially of two coplanar hot wires placed in a 1.5 mm diameter constant cross-sectional area channel, as indicated in Figure 2-4. The convergent exit of the channel leads to a vacuum source and is choked during probe operation. The two hot wires are set at different overheat ratios, and hence different wire temperatures, and in this mode allow the simultaneous measurement of both total temperature and total pressure, as will be shown. A total pressure impact probe incorporating a Kulite XCQ-093 silicon diaphragm pressure transducer is installed 'piggyback' to the aspirating probe. The pressure transducer gives a redundant measure of total pressure and allows for separate measures of total temperature from each hot wire. The pressure transducer has the added benefit of reducing the probe's measurement uncertainty but at the expense of reduced longitudinal spatial resolution [11]. The hot wires themselves are made from platinum plated tungsten with the sensing length defined by copper plating. The wires are soldered in place using multicore solder beads. Care is taken to ensure the wires are taut and as close to the

center of the channel as possible. A typical wire separation distance is 250 um. Typical wire dimensions are 1.27 mm in length and 5.1 um in diameter. The hot wires are operated with standard TSI-1050 constant temperature anemometers.

The classical governing equation for the anemometer bridge voltage of a constant temperature hot wire is:

$$\frac{V^2}{[Tw - r\ T]} = \left[\frac{Rs + Rw}{Rw}\right]^2 \pi\ l\ k\ Nu \qquad [2.1]$$

where V is the bridge output voltage, Tw the hot wire temperature, r the wire recovery factor, Rs the anemometer resistance in series with the hot wire, Rw the wire operating resistance, l the wire length, k the fluid thermal conductivity, and Nu the Nusselt number. This equation applies only when the hot wire is operated in a gas of uniform composition. The Nusselt number is a function of many fluid and wire properties [12], but is often expressed in the following form as a function of the hot wire Reynolds Number only:

$$Nu = a\left(Re_d\right)^N + b \qquad [2.2]$$

The coefficients of this equation, which is often referred to as King's Law, are determined by calibration. Since the channel of the aspirating probe is choked, we may represent the channel mass flux as a function of the fluid properties, total pressure, total temperature, and ratio of sonic-to-channel area ratio at the hot wire plane:

$$\rho U \;=\; \frac{P}{\sqrt{T}}\;\frac{A^*}{Ac}\;\sqrt{\frac{\gamma}{R}}\left(\frac{2}{\gamma+1}\right)^{\frac{\gamma+1}{2(\gamma-1)}} \qquad [2.3]$$

The corresponding Reynolds number is then given by:

$$Re_d \;=\; \frac{d}{\mu}\left[\frac{P}{\sqrt{T}}\;\frac{A^*}{Ac}\;\sqrt{\frac{\gamma}{R}}\left(\frac{2}{\gamma+1}\right)^{\frac{\gamma+1}{2(\gamma-1)}}\right] \qquad [2.4]$$

where d is the wire diameter, μ the fluid viscosity, P the total pressure, T the total temperature, A* the choked exit area, Ac the wire plane channel area, γ the fluid ratio of specific heats, and R the fluid gas constant. Finally, we may combine Equations 2.1, 2.2, and 2.4 to yield the governing equation for the aspirating probe:

$$\frac{V^2}{[Tw - r\,T]} \;=\; \left[\frac{Rs+Rw}{Rw}\right]^2 \pi\;l\;k\left\{a\;\;\frac{d}{\mu}\left[\frac{P}{\sqrt{T}}\;\frac{A^*}{Ac}\;\sqrt{\frac{\gamma}{R}}\left(\frac{2}{\gamma+1}\right)^{\frac{\gamma+1}{2(\gamma-1)}}\right]^N + b\right\} \qquad [2.5]$$

which can be reduced to the following form.

$$\frac{V^2}{[Tw - r\,T]} \;=\; C\left(\frac{P}{\sqrt{T}}\right)^N + D \qquad [2.6]$$

Equation 2.6 applies when the probe geometry and gas composition are fixed. By operating the two wires at different overheat ratios in separate anemometer circuits, two forms of Equation 2.6 are obtained from which we may determine

the unknown total pressure and total temperature. The coefficients C and D are found by calibration and, unfortunately, are a function of gas temperature. This functional relationship is driven by the sensitivity of the test gas viscosity and thermal conductivity to temperature. This characteristic of the aspirating probe is discussed further in Section 2.2.2.3.

The influence of the hot wire properties on the probe output voltage is evidenced by Equation 2.5. In particular, increasing wire resistance, length, and diameter all tend to increase the anemometer output voltage. The net effect is generally improved resolution. This aspect of the aspirating probe along with its other performance characteristics are now considered.

2.2.2.2 Performance Characteristics

As indicated above, the hot wire characteristics including length, diameter, and resistance dictate the aspirating probe output voltage for a given gas. Nominal wire conditions of 1.27 mm length, 5.1 um diameter, and 3.00 Ohms resistance give a temperature sensitivity of 12.5 mv/C at 0.86 atm and an overheat ratio of 1.8. At an overheat ratio of 2.0, the temperature sensitivity is 10.1 mv/C at 0.86 atm. At a temperature of 350 K, the probe's sensitivity to pressure is 0.88 V/atm at an overheat ratio of 1.8 and 1.00 V/atm at an overheat ratio of 2.0. These sensivities apply to an argon-freon-12 mixture typical of that used in the TBF and, further, the pressure of 0.86 atm and temperature of 350 K are

characteristic of the flowfield downstream of the facility's turbine.

The hot wires are operated with two separate TSI-1050 constant temperature anemometers. The noise levels are typically on the order of 2 mv peak-to-peak. The analog-to-digital converter employed has a resolution of 2.5 mv, and as such, sets the probe resolution at approximately 0.2 C in temperature and 0.003 atm in pressure. An error analysis at 1 atm and 290 K gives a pressure uncertainty of 0.4% and a temperature uncertainty of 0.4% (1.2C) when data are reduced with 1 wire and the pressure transducer [20]. For operation in dynamic flowfields, angle effects are negligible below 15 degrees and the response is symmetric about the probe axis [11]. Finally, for the TBF test gas, the aspirating probe natural frequency is 15.46 kHz with a damping ratio of 0.36. The determination of frequency response is detailed in Chapter 3.

2.2.2.3 Calibration Procedures and Results

The aspirating probe is calibrated against temperature and pressure in an argon-freon-12 gas mixture with a freon mass fraction of approximately 0.51 %. The temperatures and pressures surveyed include the operating range of the test turbine. The calibrations are accomplished in the TBF supply tank. Ideally, we would like to calibrate the probe while immersed in a steady flow (or well characterized dynamic flow) but no facility for accomplishing this type of calibration was available. The static calibration is fully acceptable,

though, given the high frequency response of the probe.

The coefficients C and D are determined from a least-squares linear regression of Equation 2.6, resubmitted below, for a set of voltage and pressure pairs at a constant calibration temperature and hot wire overheat ratio.

$$\frac{V^2}{[Tw - r\ T]} = C\left(\frac{P}{\sqrt{T}}\right)^N + D \qquad [2.6]$$

The exponent, N, is chosen and kept constant for the curve fit. Iteration gives a value of N, usually around 0.3, yielding the lowest standard deviation versus the calibration data. Typical values for the aspirating probe coefficients are given for two hot wire overheat ratios in Table 2-1 below. Hot wire properties and dimensions are also indicated.

Overheat Ratio		1.80	2.00
C [T**(N/2-1) V**2 / P**N]		0.3115	0.2752
D [V**2 / T]		-0.0231	-0.0226
N		0.30	0.30
Calibration Gas - Argon Freon-12 mixture with Freon mass fraction of 0.51%			
Wire Material - Platinum coated Tungsten			
Wire Temperature, Tw [K]		491.1	539.4
Wire Length, L [MM]		1.27	1.27
Wire Diameter, D [uM]		5.10	5.10
Temperature Coefficient of Resistance, a [OHMS/C]		0.004	0.004
T - Temperature in Kelvin			
P - Pressure in Atmospheres			
V - Volts			

Table 2-1: Aspirating Probe Calibration Coefficients
Versus Hot Wire Overheat Ratio

The gas mixture kinematic viscosity, μ, and thermal conductivity, k, are both functions of temperature and thus have the unfortunate effect of making C and D functions of temperature as well. The functional relationships between C and D and the fluid properites are clear from Equation 2.5. From Collis and Williams [13], the fluid properties take on values commensurate with the average of the freestream gas temperature and the hot wire operating temperature. This explains the variation of coefficients C and D with overheat ratio, and hence wire temperature, in Table 2-1. As long as the overheat ratio is kept constant, though, the wire temperature effect is not a problem. The coefficient sensitivity to the freestream gas temperature on the other hand is a problem since it is this temperature that we wish to measure. Accordingly, the coefficients must be corrected for fluid property variations with temperature.

Figures 2-5 A and B show calibration curves for the aspirating probe at overheat ratios of 1.8 and 2.0 respectively. Two sets of calibration data are shown on each figure for gas freestream temperatures of 321.7 K and 349.5 K. The data taken at 321.7 K, indicated by the squares, are curve fitted to Equation 2-6 yielding the coefficients shown. For purposes of illustration, these same coefficients along with Equation 2.9 are used to predict the second set of calibration data taken at 349.5 K, indicated by the triangles. For both overheat ratios the standard deviation increases from approximately 0.3 C in the curve fitted case to 4.0 C in the

predicted case.

Presumably, we can improve the prediction by accounting for the effects of freestream temperature on the gas mixture viscosity and thermal conductivity. Such corrections would take the following form where the primed variables indicate reference values.

$$C = C' \; \frac{k}{k'} \; \left[\frac{\mu'}{\mu} \right]^N \qquad\qquad [2.7]$$

$$D = D' \; \frac{k}{k'} \qquad\qquad [2.8]$$

Note we may use this same approach to correct for changes in the wire characteristics like resistance, length, and diameter. These corrections are straightforward and not addressed further.

As previously noted, the fluid properties are evaluated at the average of the freestream temperature and hot wire operating temperature. Values for the kinematic viscosity and thermal conductivity are taken from [14] for argon and [15] for freon-12. The empirical correlation proposed by Buddenberg and Wilke [16], developed to predict the constants in the Sutherland-Thiesen equation for binary gas mixtures, is used to determine the properties of the argon-freon-12 test gas mixture. This correlation is shown below for the test gas mixture's thermal conductivity; the same correlation applies for kinematic viscosity.

$$k \text{ mix} = \frac{k1}{1 + \frac{X2}{X1} Q12} + \frac{k2}{1 + \frac{X1}{X2} Q21} \qquad [2.9]$$

where

$$Q12 = \frac{\left(1 + \left[\frac{k1}{k2}\right]^{\frac{1}{2}} \left[\frac{M2}{M1}\right]^{\frac{1}{4}}\right)^2}{\sqrt{8 + 8 \frac{M1}{M2}}} \qquad [2.10]$$

$$Q21 = \frac{\left(1 + \left[\frac{k2}{k1}\right]^{\frac{1}{2}} \left[\frac{M1}{M2}\right]^{\frac{1}{4}}\right)^2}{\sqrt{8 + 8 \frac{M2}{M1}}} \qquad [2.11]$$

In the equations above, 1 and 2 refer to each component of the binary mixture with X representing mole fraction and M molecular weight.

Applying the corrections above results in a much improved prediction of the calibration data as is shown in Figures 2-5 C and D. These data are the same as discussed previously. In each case, the standard deviation of the predicted data is of the order of the curve fitted data. Clearly, the method for correcting the aspirating probe calibration coefficients works. Hence, using some iteration scheme to find C and D as functions of temperature relative to the calibration data, we may solve for both total temperature and total pressure in the turbine flowfield. The aspirating probe data reduction procedures, including this iteration scheme, are addressed in the following section.

2.2.2.4 Data Reduction Procedures

The three analog signals from the two hot wires and one total pressure probe are digitized during the test and subsequently stored on hard disk in a PDP 11/70 computer. The silicon diaphragm pressure transducers provide good measures of total pressure so we are primarily interested in measuring total temperature with the aspirating probe. There are two approaches to reducing the data.

The first approach utilizes the total pressure measurement made with the 'piggybacked' pressure transducer. The pressures measured by the attached probe and voltage from either wire is used to calculate temperature from Equation 2-6. For this calculation, the exponent N is chosen based on experience with the calibration data. A simple secant-type iteration scheme is then employed to solve for temperature while including the effects of the temperature on the coefficients C and D [17]. The value of tungsten's temperature coefficient of resistance, e, is input to calculate the wire temperature with the equation below:

$$\frac{Rh}{Rc} = \text{Overheat Ratio}$$

$$= 1 + e \, [Tw - r \, T] \qquad [2.12]$$

where Rh is the hot wire operating resistance, Rc the hot wire cold resistance, Tw the wire temperature, r the fluid recovery factor, and T the fluid temperature. Both the wire overheat ratio and recovery factor are input. For thin wires the

recovery factor, r, is always greater than 0.98 [12].

The second approach utilizes both wires to find temperature; the pressure transducer is not used. This approach takes advantage of the coefficient correction scheme addressed in the previous section. Based on the calibration data, curves of bridge output voltage for both wires can be constructed versus temperature and pressure as shown in Figure 2-6. Using the numerical equivalent of this grid and a simple interpolation routine, we can estimate the flowfield temperature given the voltage signals from the two hot wires.

2.2.3 The Four-Pressure-Transducer Angle Probe

The angle probe is a high-frequency response instrument which provides measurements of total pressure, static pressure, Mach number, and radial and tangential flow angles, and is shown in Figure 2-7. As with the aspirating probe, this probe was designed and constructed to investigate the flowfield downstream of a transonic compressor [10]. The original angle probe was spherical in shape and included five silicon pressure transducers from which the flowfield data were retrieved [18][19]. Subsequent designs incorporated four pressure transducers, instead of five, mounted on an elliptical stem. The later probes utilize water cooling to improve their temperature stability. The probe used in the present case is one of the latter designs and is now described. In addition, the probe's performance characteristics, calibration procedures and results, and data reduction procedures are presented.

2.2.3.1 Description and Physics of Operation

The angle probe consists of four silicon diaphragm pressure transducers located on an elliptical stem as shown in Figure 2-7. The transducers utilized are Kulite model XCQ-093 with abolute pressure reference, and are numbered on the figure for reference. Transducers 2 and 3 are offset from the center transducer by 45 degrees while transducer 4 is placed flat on the probe tip. The tip, as shown, is also set at a 45 degree angle. Cooling water is supplied through the base of the probe and circulated around the backside of the transducers, thus enhancing their thermal stability.

As was done with the spherical probe [19], we may define coefficients based upon the four pressures measured by the angle probe. These are:

$$F23 = \frac{P2 - P3}{(P2-P1) + (P3-P1)} \qquad [2.13]$$

$$H23 = \frac{Pt - Ps}{(P2-P1) + (P3-P1)} \qquad [2.14]$$

$$KP2 = \frac{P2 - Ps}{(P2-P1) + (P3-P1)} \qquad [2.15]$$

$$KP3 = \frac{P3 - Ps}{(P2-P1) + (P3-P1)} \qquad [2.16]$$

$$CP1 = \frac{P1 - Ps}{Pt - Ps} \qquad [2.17]$$

$$CP4 = \frac{P4 - Ps}{Pt - Ps} \qquad [2.18]$$

and results given. Finally, measurements taken in the TBF
coupled with their brief analysis are presented.

traverse velocity by the 3ØØ ms point. The full traverse takes place over approximately 12Ø ms.

All the probes described above operate throughout the full test time with the exception of the aspirating probe. This probe's hot wires handle dynamic gas loads well but not particulates in the test gas. The wires are susceptible to particulate deposits which may weaken the wires or otherwise invalidate their calibrations. Though the facility test gas is considered clean, care is taken to operate the probe's suction only for the test time (note the wires are left on continuously). A small pneumatically activated fast acting valve is used for this purpose. The valve is spliced into the flexible hose connecting the aspirating probe to a small mechanical vacuum pump. The valve is opened at 15Ø ms and flow through the probe is immediately established. The valve closes 1ØØ ms later but it takes approximately 4 seconds for the flow into the aspirating probe to stop. The probe does not unchoke until the 1 second point, well after the test time. By this method, dangers to the aspirating probe's hot wires are minimized.

In summary, we have reviewed the TBF setup and operating procedures, paying particular attention to the operation of the aspirating probe. Elsewhere in this chapter, the TBF facility, turbine, and data acquisition system have been described. The various probes and probe traverser, along with their descriptions and modes of operation, have also been addressed. In the following chapters, a shock tube facility for measuring instrumentation frequency response is described

oil through the flow control valve and against the drive piston. The magnitude and steadiness of the piston velocity is controlled by both the gas cylinder pressure and control valve setting. The probes are attached directly to the drive piston. The travel of the device is 60 mm and takes place nominally in 0.1 seconds. A typical traverse is depicted in Figure 4-1.

2.3 Facility Operation Procedures and Experimental Technique

Operation of the TBF is now reviewed. A more detailed discussion of the facilities operating procedures are given in [1]. Once the instrumentation required for a test is installed, the valve is closed between the supply and dump tanks and both are evacuated (<0.1 torr). The supply tank is then heated to the desired temperature, typically 478 K. The heating is done slowly to ensure thermal equilibrium. Once at temperature, the supply tank is filled with the test gas mixture of argon-freon-12 to the desired pressure, typically 4.2 atm. The gas assumes the supply tank temperature by the end of the fill. Finally, the rotor, which is still in vacuum, is brought up to speed by a small electric motor. When the desired initial rotor speed is achieved, the valve and eddy current brake are simultaneously triggered and flow of the test gas from the supply tank is established.

The high-speed data acquisition phase begins at approximately 250 ms into the test, by which time the flowfield is fully established, and lasts 100 ms. The traverser is activated at 260 ms and achieves a constant

transducers which are normally referenced to vacuum. Calibrations are performed immediately before and after each test by alternating the reference pressure from vacuum to atmosphere.

2.2.5 The Traverser Mechanism

Short test times characterisitic of the TBF complicate the radial and circumferential traversal of instrumentation during a test. The traversal must be timed to occur during the high-speed data acquisition phase and, preferably, take place with constant velocity to facilitate data reduction. Cao [24] designed and constructed such a traverser for use in the TBF; it is detailed in Figure 2-13. The traverser can move probes both circumferentially and radially downstream of either the rotor or vane row. Circumferential traverses alone were utilized in the present set of experiments so only this function of the traverser is described.

The circumferential traversing mechanism has as its essential component a hydraulically driven piston. The device's high pressure cylinder is charged with argon (or other gas) to approximately 21 atmospheres. This cylinder, by way of a solenoid valve, is connected to an oil cylinder. This in turn is connected to the device's drive piston through a flow control valve (used to maintain constant linear velocity. A linear differential variable transformer (LDVT) attached to the piston is used to indicate position.

Actuation of the device occurs when the solenoid valve is triggered, thus allowing the high pressure gas to force the

The scheme then corrects theta and phi for a new Mach number calculated from the new static pressure and total pressure calculated from Equation 2.25. The coefficients H23, CP1, and KP2 (or KP3) are subsequently updated and the scheme continues until convergence of the static pressure is achieved. Upon convergence the Mach number is re-calculated based upon the test gas ratio of specific heats as previously indicated. The final values of the current iteration are then stored and used as initial guesses for the follow-on data set. Typically, five iterations are required before convergence is achieved.

2.2.4 The Silicon Diaphragm Total Pressure Transducers

Two silicon diaphragm pressure transducers, Kulite models XCQ-Ø93 and XCQ-Ø62, provide high-frequency total pressure measurements. The XCQ-Ø93 is carried piggyback with the aspirating probe and is similar to the ones used in the angle probe. With a diameter of approximately 1.6 mm (Ø.Ø32 inches), the XCQ-Ø62 subminiature pressure transducer is the smallest Kulite pressure transducer available providing both static and dynamic flowfield measurements. The XCQ-Ø62 has a natural frequency in excess of 5ØØ kHz and has an operating temperature range of -55 C to 12Ø C. Its nominal sensitivity is 26.5 mv/atm. Both transducers are constructed similarly to pitot probes with cobra head designs, as shown in Figure 2-4 for the XCQ-Ø93. Each transducer diaphragm is recessed approximately one diameter from the cobra head entrance to negate the probe's sensitivity to flow angle variations in the +2Ø degree range. Both total pressure probes use differential

the tangential angle, theta, is found by linear interpolation. Initial guesses for the total and static pressure are made with P1 taken as the total pressure and the lesser of P2 and P3 as the static pressure. From these an 'air equivalent' Mach number is calculated using the isentropic pressure ratio relation. The term air equivalent is used to indicate that the Mach number is based on air's value of the ratio of specific heats since the calibrations were done in air. Upon convergence of the iteration scheme, the true value of the Mach number based upon the test gas properties is found. The next coefficient calculated is CP4 which in turn is used to find phi as a function of theta. Having initial values for Mach number, theta, and phi the coefficients H23, CP1, and KP2 (or KP3 depending on which of P2 or P3 was used as an initial guess for static pressure) are determined by interpolation. The static and total pressures are then calculated with the following relations based upon the coefficient definitions:

$$Ps \quad = \quad P2,3 - P2P3 \ KP2,3 \qquad\qquad [2.24]$$

$$Pt \quad = \quad Ps + H \ (1-CP1) \ P2P3 \qquad\qquad [2.25]$$

$$where \quad P2P3 \quad = \quad (P2-P1) + (P3-P1) \qquad [2.26]$$

If the static pressure calculated from Equation 2.24 differs from the inital assumed static pressure, a new value of static pressure is chosen. This new value of static pressure is taken as the average of the assumed and calculated pressures.

test flowfield. Coefficient F23 is least sensitive to the radial angle showing virtually no effect until theta reaches ± 20 degrees. The remaining coefficients show consistant but only moderate reactions to phi.

In summary, the calibration results are supported by the simple prediction model detailed above. It is clear, however, that the angle probe's unique geometry influences the calibration coefficients. It is noted that the pneumatic model of the angle probe used for the calibrations is suppossed to be an accurate replica of the instrument used in the TBF. If variations exist, the calibration data may not be fully applicable. Unfortunately, comparative calibrations were not accomplished. The geometry related aspects of the angle probe are important and, accordingly, are included in the data reduction schemes. These are now addressed.

2.2.3.4 Data Reduction Procedures

The angle probe yields a rather complex set of coefficients influenced both by the flowfield and probe geometry, as was seen in the calibration section. The data reduction scheme outlined below has been used for both the original spherical probe and earlier four-transducer models. It relies heavily upon linear interpolation and, thus, all of the geometry related nuances of the calibration data are retained. The procedure for the current probe and most of the data reduction software has been developed by Gertz [23], and is summarized in Figure 2-12.

The scheme begins with the calculation of F23 from which

since in each case the coefficients vary consistantly with the progression of the two independent parameters. The peculiar 'bumps' and shifts in the curves are taken to be associated with the unique geometry of the angle probe and are accounted for in the data reduction schemes.

Angle probe coefficients F23, H23, KP2, CP1, and CP4 are depicted in Figures 2-10A through 2-10E versus tangential angle for Mach numbers of 0.35, 0.5, 0.6, and 0.85. The calibration data were taken for zero radial angle. Coefficient F23 is relatively unaffected by Mach number except in the +8 degree regions. The 'bumps' at these locations are not born out by the flowfield prediction and are most likely tied into the probe geometry. Coefficient H is strongly affected by Mach number via the total pressure, as expected. Coefficient KP2 (as well as KP3) is also strongly affected and, as seen with F23, shows a peculiar anomaly at -8 degrees which becomes more pronounced with decreasing Mach number. Again, this is most likely associated with the placement of the pressure transducer on the probe shaft and its attendant flat face. KP3, though not shown, exhibits the same behavior as KP2.

The same angle probe coefficients as above are depicted in Figures 2-11A through 2-11E versus tangential angle. For these coefficients, the Mach number is set at 0.6 and the radial angle is varied from -10 degrees to +10 degrees in 5 degree increments. Coefficient CP4 is strongly affected by the radial angle variation and, as discussed in the data reduction section, is key to retrieving this property of the

to the expected turbine midspan exit Mach number. The
prediction and data agree well considering the difference in
the actual probe geometry and that of an ideal two-dimensional
elliptical cylinder. In particular, the transducer faces on
the angle probe are flat and thus maintain a higher stagnation
pressure than would an ideal ellipse at the same location.
This is evidenced by CP1 where the calibration data is
consistantly higher than the prediction. This coefficient's
insensitivity to theta values in the $\pm$ 5 degree range is
clear. Likewise, the data and predictions for CP2 and CP3 are
of the same form as CP1 but offset by the transducer
separation angles of $\pm$45 degrees from center. Coefficient F23
is determined from P1, P2, and P3 in such a way that the
difference in the calibration data and prediction is
nullified, resulting in a suprisingly good fit. Coefficents
H23 and KP2, unlike F23, include the freestream static
pressure in their definitions and therefore show a difference
beteen the measured and predicted cases. For both
coefficients the data are lower than the predictions but
clearly show identical trends. The difference can be traced
to the larger values of P1, P2 and P3 used to normalize the
coefficients. KP3, the mirror image of KP2, exhibits the same
behavior as KP2. Based on these results, the method for
calibrating the probe in the freejet is deemed acceptable.
This being the case, the effects of Mach number and radial
angle on the angle probe coefficients are now shown. These
calibration data are presented to illustrate the effects of
Mach number and radial angle; only brief remarks are made

these velocities, we can solve for the local Mach number, Mn, given the freestream Mach number, Mi, as follows:

$$Mn^2 = \frac{Un^2}{(\gamma R \, Tn)} \tag{2.22}$$

$$= \left(\frac{Un}{Ui}\right)^2 \frac{Mi^2}{\left\{\left[1 + \frac{\gamma-1}{2} Mi^2\right] - \left[\frac{\gamma-1}{2}\left(\frac{Un}{Ui}\right)^2 Mi^2\right]\right\}}$$

Finally, we may solve for the local static-to-total pressure ratio using the standard isentropic form as a function of local Mach number:

$$\frac{Pn}{Pt} = \left[1 + \frac{\gamma-1}{2} Mn^2\right]^{\frac{\gamma-1}{\gamma}} \tag{2.23}$$

Thus we can determine the local static pressure at each transducer location and, except for CP4, predict all the angle probe coefficients once the freestream Mach number and tangential flow angle, theta, are specified and the radial angle, phi, is set at zero.

Measured and predicted angle probe coefficients F23, H23, KP2, CP1, CP2, and CP3 for a Mach number of 0.6 and zero radial angle are shown in Figures 2-9A through 2-9F. This Mach number was chosen for the predictions since it is close

range of calibration Mach numbers is 0.35 to 0.85 so
compressibility effects should be considered. For this case
we can apply a subsonic Prandtl-Glauert correction as follows
where the primed variables apply to the incompressible case
[22]:

$$\frac{B}{A} = \frac{B'}{A'} \sqrt{1-M^2} \qquad [2.20]$$

Applying this correction to Equation 2.19 and rearranging
yields:

$$\frac{Un}{UT} = \frac{\left[1 + \frac{B}{A}\right] \sin Q}{\left[\frac{B}{A}\right]^2 + \left[1 - \left(\frac{B}{A}\right)^2\right] \sin^2 Q} \qquad [2.21]$$

Thus, Equation 2.21 provides the local tangential velocity
distribution over an elliptical cylinder once given the
ellipse fineness ratio, A/B, and the freestream velocity. We
are only interested in the local velocity at each transducer
relative to the freestream angle of attack and, therefore,
require definitions for determining the appropriate internal
angles, Q. These definitions, shown in Figure 2.8, apply only
to a circular cylinder but the error in applying the
prediction to the angle probe is small since it has a low
fineness ratio (A/B is approximately 1.35). Additionally, the
results only apply when the the radial angle is zero. Using

blockage effects were small. Given this result, the small nozzle was utilized for all the angle probe calibrations and allowed measurements to be recorded over the full Mach number range of interest.

To increase confidence in the calibration data, predictions can be made for the coefficients F23, H23, KP3, KP2, CP1, CP2, and CP3 by modelling the angle probe as a two-dimensional elliptical cylinder. By using the potential solution for such an elliptical cylinder, we can calculate the local surface velocity and, given the freestream total temperature, determine the local Mach Number. Finally, we can determine the ratio of local static-to-total pressure ratio at each transducer location, thus allowing direct calculation of the coefficients. The equations for this procedure now follow.

The potential solution for the surface flow velocity over a two-dimensional elliptical cylinder is [21]:

$$\frac{Un}{Ui} = \frac{2 \sin Q}{\left[1 - \frac{A-B}{A+B}\right]^2 + 4 \left[\frac{A-B}{A+B}\right]^2 \sin^2 Q} \qquad [2.19]$$

where   A - ellipse semi-major axis
         B - ellipse semi-minor axis
         Q - ellipse internal ⌐ le

and   x = A cosQ
         y = B cosQ

The axes and coordinate system are defined in Figure 2-8. The

nominal thermal zero shifts are on the order of 3% per full scale per 55.5 C (100 F) while the nominal sensitivity shifts are less than 1.5% per full scale per 55.5 C (100 F). Finally, the compensated temperature range is 275 K to 422 K (35 to 300 F).

2.2.3.3 Calibration Procedures and Results

The angle probe is calibrated in a freejet against radial angle, tangential angle, and Mach number. The calibration test gas is air. The calibrations are accomplished with a precisely duplicated pneumatic model of the instrument used in the TBF. This is done to avoid damaging the relatively fragile and expensive probe constructed with the silicon diaphragm pressure transducers. All of the calibrations are done statically. As discussed later in Chapter 3, we would like to know the response of the angle probe to dynamic flowfields but no means are currently available to produce well-characterized dynamic flowfields with frequencies above 5 kHz [20]. Accordingly, only the static response of the angle probe has been incorporated into the data reduction schemes.

Probe blockage errors must be considered when freejets are used for calibrations. Accordingly, two freejet nozzles of 2.54 cm and 5.08 cm diameter were employed for the angle probe calibrations. Due to facility constraints, the maximum steady Mach number achievable with the large nozzle was only 0.4, well below the desired maximum calibration value of 0.85. Comparsion of coefficient values taken by both nozzles at the same Mach number showed no differences, suggesting that probe

Pt and Ps refer to the freestream total and static pressures respectively. Two additional coefficents, CP2 and CP3, can be defined similarly to CP1. These coefficients are not used in the data reduction but are considered in the calibration section presented later.

Based on the definitions, F23 and CP4 provide directional sensitivity, H23 Mach number sensitivity, and KP2 and KP3 static pressure sensitivity. Coefficient CP1 aids in determining the total pressure. In theory then, we may use the set of coefficients to retrieve flowfield property information including the radial and tangential flow angles, total pressure, static pressure, and Mach number once the probe is fully calibrated.

2.2.3.2 Performance Characteristics

We are particularly interested in the frequency response of the angle probe. The Kulite model XCQ-093 pressure transducers used in the instrument have natural frequencies in excess of 200 kHz. However in practice, the length scale characteristic of the probe, its diameter, coupled with the flowfield velocity sets the characteristic frequency of the probe. This frequency is approximately 45 kHz and therefore well above blade passing frequency. The angle probe's frequency response characteristics are addressed further in Chapter 3.

The pressure transducers are approximately 2.4 mm (0.093 inches) in diameter and have nominal sensitivities of 31.6 mv/atm with a nonlinearity of less than 0.5% full scale. The

CHAPTER 3

THE SHOCK TUBE -- MEASUREMENT OF PROBE FREQUENCY RESPONSE

This chapter details the development and construction of a shock tube test facility built for the purpose of measuring instrumentation frequency response. Predictions and measurements of frequency response are given for both the aspirating probe and angle probe.

3.1 Shock Tube Description and Operating Procedures

The design approach and description of the shock tube facility are detailed in this section. The operating procedures, shakedown results, and data acquisition system are also presented.

3.1.1 Shock Tube Design Approach and Desription

A shock tube test facility was designed and constructed for the purpose of measuring instrumentation frequency response. In particular, the frequency response characteristics of the aspirating probe and angle probe are desired since they both operate downstream of the TBF turbine rotor. In this turbine environment, as mentioned in Chapter 2, the probes are subjected to high frequency flowfield fluctuations which occur mostly at the blade passing frequency and its harmonics. In order to accurately measure or even distinguish the blade-to-blade flowfield structure, the probes natural frequencies must be well above the blade passing frequency. Therefore, we must determine each probes frequency

response in order to assess its applicability for use in the turbine facility. The shock tube is a vehicle for making this assessment.

Step function tests are commonly used to investigate instrumentation dynamic response. As a general rule for step testing, the rise time of the step function must be less than one-fourth of the natural period of the instrument tested [25]. This rule ensures excitation of the instruments natural oscillations. Shock tubes typically provide very sharp changes (on the order of 10^{-8} seconds) in pressure, temperature, and flow velocity, thus making them suitable for investigating natural frequencies well above one megahertz. Further, they can be designed for simple operation while still providing repeatable results. It was for these reasons that a shock tube test facility was selected for the frequency response measurements.

In approaching the shock tube design task several criteria were considered, the first being ease of operation. In particular it was felt the shock tube should operate without a diaphragm bursting mechanism. This was a point of concern since the anticipated test pressure ratios were low. Accordingly, any variance in the diaphragm material properties could result in very different burst pressures. Also, bursting could be ragged, thus sending particles of diaphragm material into the driven tube which could potentially damage sensors. Secondly, the facility had to be flexible in the sense that any practical bottled gas could be used in either the driver or driven sections of the tube. This criterion

required that fill and vacuum lines be sent to both sides of the shock tube. Next, the device had to provide repeatable pressure rises on the order of the blade-to-blade pressure fluctuations downstream of the turbine rotor. This criterion essentially dictated the diaphragm pressure ratio. Finally, the test time -- the time beginning with the passage of the initial shock wave and ending with the passage of either the reflected shock or gas interface -- had to be long enough to allow for several periods of a low order kilohertz signal. This criterion dealt primarily with the driven tube length and relative positioning of the instrumentation ports.

The shock tube was designed in accordance with the criteria above. Both the driver and driven sections of the device were set at lengths of 3.281 m (10 ft), and were constructed from shedule 40 (2 in i.d.) pipe made of 316 stainless steel. The opposite ends of each section were capped with 304 stainless steel blind flanges while the mating ends were capped with similar socket welded flanges. A double O-ring and groove configuration was machined into the mating flanges. This arrangement proved successful in holding the diaphragms taut while the driver side of the facility was charged. No diaphragm breaking mechanism was required, as discussed later. Additionally, stainless steel dowel pins were placed into the mating flanges to help with alignment. The pins also served to hold the diaphragms in place while the facility was recycled between tests. To allow for operation with any bottled gas, fill and vacuum lines were lead to the opposite ends of each section. Standard one-quarter inch

copper tubing was used for the fill lines; one-half inch copper tubing for the vacuum lines. Between the driver and driven sections, the fill lines were connected with a flexible length of PVC tubing while the vacuum lines were connected with flexible vacuum hose. Valving was designed to allow filling and evacuation of either section independently from the other. Finally, facility instrumentation was minimized and included only a Type J thermocouple and vacuum and pressure gauges.

Positioning of the instrumentation mounts was accomplished by predicting the shock velocity, reflected shock velocity, and interface gas velocity as a function of diaphragm pressure ratio, gas temperature, and gas properties. Standard one-dimensional shock tube relations were employed for these calculations [26]. A map of time versus driven tube position can be constructed by dividing the velocities above by the chosen driven tube length, as shown in Figure 3-1 for air. The diaphragm pressure ratio for the case shown is approximately 1.48, yielding a pressure ratio across the shock of approximately 1.2. This pressure rise is on the order of what an instrument would experience downstream of the TBF's turbine rotor. The initial values for temperature and pressure in the driven tube are standard room conditions. As previously defined, the test time begins with the passing of the initial shock and its attendant step change in pressure, temperature, and velocity. The test time concludes with the passage of either the reflected shock wave or interface gas velocity and its respective muddling of the original step

function flow field. For the conditions of Figure 3-1, the maximum test time occurs at the 24% driven tube length and has a duration of approximately 13 milliseconds. This is an enormous amount of time for dynamic testing of instrumentation. Higher diaphragm pressure ratios would give higher shock velocities and, for the same driven tube length, have the dual effect of reducing overall test time and moving the maximum test time position farther down the tube. In anticipation of using higher pressure ratios at some future date, the instrumentation mount locations were set at the 30% and 40% driven tube positions. Test times for these positions in air are 12 and 10 milliseconds respectively.

The next step following the design and construction of the shock tube involved the determination of diaphragm materials and operating procedures. These aspects of the shock tube development along with initial shakedown results are now presented.

3.1.2 Shock Tube Operating Procedure and Shakedown Results

Operation of the shock tube proved to be very simple. For tests in air, the driven tube is simply filled with air from a regulated high pressure cylinder until the diaphragm breaks. Depending on the diaphragm, this process was surprisingly repeatable. For operation with other gases, both sides of the shock tube are initially evacuated and then filled with the test gas to some pre-determined pressure. The driven section fill line is then cut off from the supply while the driver continues to fill until the diaphragm breaks. This

process also proved to be repeatable. Separate gases could be used in the driver and driven sections but this permutation was not investigated. In all cases, the double O-ring and groove configuration of the mating flanges held the diaphragms secure until bursting occurred.

Several potential diaphragm materials were tested including cellophane, paper, vellum, and metal foil. Diaphragms that broke repeatably, cleanly, and at a pressure ratio of 1.2 to 2.0 (normalized by atmosphere) were desired. Cellophane (DuPont MSD-60, 220 gauge, 22.8 μm thick) was found to meet these desirable qualities the best. This material did have the occasional problem of releasing particles upon breaking, but no sensors were damaged. The repeatability on breaking was approximately 15% (typically 7 psia ± 1 psia, which was within the accuracy of the pressure gauge used).

Shock wave velocity measurements were conducted to confirm the device operated as standard shock tube relations would predict. The wave velocities were measured using two platinum thin-film gauges operated with TSI-1050 constant temperature anemometers. The thin-film gauges were placed on the shock tube inner wall surface at a known separation distance. The time between response to a passing shock wave was measured on an oscilloscope and used along with the separation distance to calculate the wave velocity. The velocities measured were consistantly within 10% of predictions. These results were considered good given that the diaphragm break pressure was read visually from a pressure gauge mounted to the driver tube. These results were later

confirmed using a hot wire to measure the post-shock flow field velocity and its characteristic steadiness over the test time. These data are discussed later in Section 3.3.2. Additionally, it was found the wave velocities from the diaphragm pressure ratio desired, approximately 1.5, were sufficient to excite the damped natural frequencies of Kulite XCQ-093 and XCQ-062 strain gauge pressure transducers. These frequencies were 250 kHz and 500 kHz respectively, well above those anticipated from either the aspirating probe or angle probe.

A Tekronics 468 digital recording oscilloscope is used to acquire the test data. The measuring instrument acts as the trigger. Once taken, the data are passed to an LSI 11/23 computer through an IEEE-488 GPIB and stored on floppy disk. The data are subsequently transferred to a DEC PDP 11/70 computer for reduction and analysis.

In summary, a shock tube facility for testing instrumentation frequency response was designed and constructed. Its operation was very simple while its results proved to be repeatable. Measured shock wave velocities and interface gas velocities were consistently within 10% of predictions from standard one-dimensional shock wave relations. With the shock tube operating as a viable tool for frequency response investigations, measurements were made with both the aspirating probe and angle probe. These results are now presented.

3.2 Aspirating Probe Frequency Response

In this section, the governing equations for the aspirating probe natural frequency and damping ratio are described. Subsequently, we employ the equations to predict the probe's natural frequency and damping in both air and Freon-12, and compare the predictions to shock tube test results. The instrument's predicted response in an argon-freon mixture, the gas utilized in the TBF, is then presented. Finally, we discuss means of improving the frequency response characteristics of the aspirating probe based on the shock tube results.

3.2.1 Governing Equations for Natural Frequency and Damping

The frequency response of compensated constant temperature hot wire anemometers is typically on the order of 100 kHz [12]. In the present case, however, frequencies associated with the gas flowing in the aspirating probe channel must be considered and, as will be shown in the next sections, are considerably lower than the hot wire anemometer frequency quoted above.

The aspirating probe channel can be modelled as a constant area duct with mass flow as shown in Figure 3-2. As with a number of fluid systems having tubing or ducts (pressure transducers with plumbing, for example), the aspirating probe can be shown to exhibit second-order instrument behavior. In particular, Whitehead [27] gives the relationships required to investigate a system as modelled above. These relationships are addressed in the next section, but first, a brief discussion of second-order instrument

behavior is given.

Using the definitions of [28], a second-order instrument is defined as one that follows the equation:

$$a1 \frac{dq}{dt} + a2 \frac{dq}{dt} + a0 \, q = b0qi \qquad [3.1]$$

where q is the output quantity, qi is the input quantity, t is time, and the a's and b's are system physical parameters which we shall assume to be constant. From equation 3.1, we may define three parameters:

$$K = \frac{b0}{a0} \qquad \text{static sensitivity}$$

$$wn = \sqrt{\frac{a0}{a2}} \qquad \begin{array}{l}\text{undamped natural frequency,}\\ \text{rad/time} \quad (\ f = w/2 \quad \text{Hertz} \ )\end{array}$$

$$z = \frac{a1}{2\sqrt{a0a2}} \qquad \text{damping ratio, dimensionless}$$

Rearranging equation 3.1 in terms of these three parameters yields:

$$\left[\frac{D^2}{wn^2} + \frac{2zD}{wn} + \right]1 \ q0 = K \ qi \qquad [3.2]$$

where D = d /dt.

From equation 3.2, then, we may define an operational transfer function applicable to all second-order instruments:

$$\frac{q0}{qi} (D) = \frac{K}{D^2/wn^2 + 2zD/wn + 1} \qquad [3.3]$$

It is evident from equation 3.3, that to determine the operating charactersitics of any second-order instrument, we need only determine its natural frequency and damping ratio.

To investigate the response of a second-order instrument to dynamic input conditions -- its frequency response -- we may use equation 3.3 along with a suitable sinusoidal transfer function representing some harmonic excitation. Following the analysis in [29], for the complex sinusoidal transfer function qØ/qi (iw), we obtain from equation 3.3:

$$\frac{q\emptyset}{qi}\ (iw)\ =\ \frac{K}{(iw/wn)^2 + 2z\,iw/wn\ +\ 1} \qquad [3.4]$$

$$\text{where}\quad i\ =\ -1$$
$$w\ =\ \text{frequency,}$$

which may be reduced to the following form:

$$\frac{q\emptyset}{Kqi}\ (iw)\ =\ \frac{1}{[\,1-(w/wn)^2\,]^2 + 4z^2 w^2/wn}\ \angle\ \phi \qquad [3.5]$$

$$\text{where}\quad \phi\ =\ \arctan\ \frac{2z}{w/wn\ -\ wn/w} \qquad [3.6]$$

For any chosen input frequency, w, the magnitude of equation 3.5 represents numerically the ratio of the output to input signal amplitudes. The angle of this complex number represents the phase angle by which the output leads the input signal. The term qØ/qiK is often referred to as the magnification ratio while the term w/wn is called the frequency ratio.

Using equations 3.5 and 3.6, we may construct

nondimensionalized frequency response curves by choosing values of frequency ratio and damping ratio, as shown in Figure 3-3. Curves of phase angle versus frequency ratio are also shown. These curves represent the frequency response characteristics of all second-order instruments. From the curves, we see that increasing natural frequency, wn, yields a greater range of frequencies, w, for which the magnification ratio is close to unity. Accordingly, a high natural frequency is required to accurately measure high frequency input signals. The effect of damping ratio, z, is also apparent as it can be seen that a value of approximately 0.6 to 0.7 gives the widest flat magnification ratio. In addition, for these values of damping ratio, we see that the phase angle varies almost linearly with frequency ratio. This linearity is important if we wish to obtain the correct shape of the input signal [29].

In summary, all second-order instruments are governed by the operational transfer function given by equation 3.3, which has as its essential variables the natural frequency, wn, and damping ratio, z. To determine the frequency response of these instruments, we may use a sinusoidal transfer function which is obtained by replacing iw for D in equation 3.3, thus obtaining equation 3.4. From equation 3.4, we can construct plots of magnification ratio and phase angle versus frequency ratio with the damping ratio as an independent variable. From these plots it can be seen that a high natural frequency is required to accurately measure high frequency input signals. Additionally, it is seen that damping ratios on the order of

0.6 to 0.7 give the widest range of flat magnification ratio
and phase angle linearity. Finally, since the aspirating
probe behaves as a second-order instrument, we can investigate
its frequency response by determining its natural frequency
and damping ratio. This is done in the following section.

3.2.2 Prediction of Probe Natural Frequency and Damping Ratio

As mentioned above, the aspirating probe can be modelled
as a constant area duct with mass flow. For the conditions of
subsonic mean flow and a choked exit, Whitehead [27] obtains
the following relation for the system undamped natural
frequency in Hertz, f, as a function of the mean flow Mach
number, M, gas sonic speed, C, and duct length, L:

$$f = \frac{(2n-1)(1-M^2)C}{4L} \qquad [3.7]$$

The variable n is an integer value defining the frequency mode
shape. For the analysis, Whitehead assumes the duct has a
uniform cross section and is fed at constant total pressure
through a short contraction. He also makes the assumptions of
one-dimensional flow, perfect gas, small flow oscillations,
and negligible fluid friction. To the extent that these
assumptions are realistic for the probe while operating
downstream of a turbine rotor, the result applies. The only
marginal assumption seems to be the one regarding constant
total pressure. In fact, total pressure will vary as a
minimum at the blade passing frequency. Nevertheless, as will

be shown, the probe's natural frequency is well above the blade passing frequency, so on the time scale of the natural frequency the total pressure can be considered quasi-steady. We shall assume from now on that Whitehead's result is applicable and represents the governing equation from which we may predict the aspirating probe's natural frequency.

In addition to the natural frequency, Whitehead gives the following relationship for determining the system damping ratio, z, as a function of Mach number, M, and ratio of specific heats, Gamma:

$$\frac{(2n-1)}{2} z = \ln \frac{(1+M)(1+kM)}{(1-M)(1-kM)} \qquad [3.8]$$

$$\text{where} \quad k = \frac{(Gamma-1)}{2}$$

Having relationships for both natural frequency and damping ratio, we can now make predictions.

It is reasonable but not certain that equations 3.7 and 3.8 apply to the aspirating probe; but by testing the probe in two different gases, thereby changing the gas constant and gamma and hence sonic speed, we can assess their applicability. If it is clear they do apply, then we can predict the probe's frequency response for the argon-freon-12 mixture used in the TBF with confidence. Measurements could be made in the appropriate argon-freon-12 mixture, but logistically and operationally it is more convenient (and equally valid) to make the measurements in two more readily available gases. Accordingly, air and freon-12 were chosen

for the shock tube tests. These gases have the added advantage of possessing greatly different gas constants, thus giving greatly different predictions for natural frequency. The predictions for these gases at room temperature and for the actual aspirating probe channel length are given below in Table 3-1.

Test Gas	Air	Freon-12
Channel length, L [MM]	3.886	3.886
Temperature, T [K]	305.0	305.0
Gas constant, R [J/KG K]	287.2	68.8
Gamma	1.40	1.14
Sonic speed, C [M/S]	350.2	146.3
Channel Mach number, M	0.199	0.2
Natural Frequency, f [kHz]	21.63	9.53
Damping Ratio, z	0.97	0.89

Table 3-1: Aspirating Probe Natural Frequency and Damping Ratio Prediction for Both Air and Freon-12

The channel Mach number noted in the table above is calculated using the channel cross-section to sonic orifice area ratio and the ratio of specific heats, gamma. In this calulation, growth of the thermal and momentum boundary layers are also considered. The predictions can now be compared to measurements made for the aspirating probe in the same set of gases.

3.2.3 Measurement of Probe Natural Frequency and Damping Ratio

of course, is due to the probe translation across the vane gap. Comparison of the 7 and 37 cycle ensembles indicate only small disrepancies despite the probe translation. Accordingly, the data presented in the following sections are ensembled over 37 cycles except where noted otherwise.

4.2.2 Aspirating Probe Measurements

Total temperature and pressure ratios measured with the aspirating probe are presented in this section. The measurements were taken at the 100%, 125%, and 80% corrected speed points. Table 4-3, below, gives a summary of the test conditions and reference values. Figures showing the test data at each test point are also indicated.

Test	Corrected Speed	Time	Tref [K]	Pref [atm]	Figure	
2	NC = 100%	292	461	3.43	4-7,	4-8
		360	459	3.36	4-9,	4-10
		430	456	3.26	4-11,	4-12
3	NC = 125%	292	476	3.50		4-13
		355	473	3.37		4-14
		430	470	3.26		4-15
4	NC = 80%	292	468	3.44		4-16
		365	465	3.36		4-17
		430	462	3.23		4-18

Table 4-3: Summary of Aspirating Probe Measurement Conditions

The data taken with the aspirating probe hot wires were reduced with the pressure signal obtained from the XCQ-092 pressure transducer, thus yielding two separate measures of

value for reduced frequency indicates there is at least one vane wake in a blade passage at any instant in time. Further, this implies that we can determine the predominant rotor exit profile with relatively few blade-passing cycles. This point is confirmed shortly.

Ensemble averages of total pressure are presented in Figures 4-3 A and B for the 292 msec test point. Each period of the ensembled traces shown are the same; seven periods are displayed only for comparison with the instantaneous traces. The measurements were taken at the 100% corrected speed condition with the aspirating probe's total pressure transducer (XCQ-092). Seven, 37, and 111 cycle ensemble averages are shown superimposed with the instantaneous pressure signal where, for reference, 61 cycles corresponds to one rotor revolution. The seven and 111 cycle ensembles are plotted togethor on the lower grid in Figure 4-3B. Their close agreement suggests that the periodic nature of the total pressure profile can be found with relatively few cycles. Ensemble averages of total temperature are shown in Figures 4-4 A and B for the 292 msec test point with results similar to those seen with total pressure.

Ensemble averages for total pressure and temperature are presented in the same format as above except at the 360 msec test point, i.e. during the traverse. Total pressure ratios are shown in Figures 4-5 A and B while the total temperature ratios are shown in Figures 4-6 A and B. For both pressure and temperature, the 111 cycle ensembles are seen to differ significantly from the 37 and 7 cycle traces. The difference,

the probe is located approximately in the core flow region of the upstream vane. In the second, at 360 msec, the probe is located in the wake region of the upstream vane as suggested by the low total pressure reading. In the third, at 430 msec, the probe is located roughly in the transition region between the vane core and wake flow. The data are presented in nondimensional form, being normalized by the vane inlet (supply tank) total temperature and pressure. These values change appreciably during the blowdown run, however, so the reference temperature and pressure must be corrected for each test time. These corrected reference values are given for each set of data presented. Finally, it is mentioned that the data presented in this Chapter are the first published set of high-frequency total temperature and pressure data taken in a turbine stage.

4.2 Experimental Measurements

High-frequency measurements taken in the Turbine Blowdown Facility by the aspirating probe, angle probe, and total pressure probes are now presented. First, however, the approach used to ensemble average the data is discussed.

4.2.1 Ensembling Technique

The data presented in the following sections are ensemble averaged to reveal the periodic nature of the flowfield structure. For the turbine design point corrected speed and mass flow, the reduced frequency defined in Chapter 1 equals 1.07 (U=158 m/s, t=0.045 m, bx=0.025m, and Cx=82.3 m/s). This

In Test 1, the XCQ-Ø62 total pressure probe was traversed circumferentially downstream of the turbine at the rotor exit midspan; in Tests 2-4, the aspirating probe was traversed. The traverse length was 6Ø mm, or approximately 1.33 vane gaps. Both the probe position and translation path for the traverses are shown in Figure 4-1 along with a typical time trace. The time trace indicates the traverse linearity. The angle probe was not traversed.

For later reference, values for the turbine midspan velocity triangle, obtained from a streamline curvature program, are given below in Table 4-2. These apply to the 1ØØ% corrected speed operating condition.

Corrected Speed, NC	1ØØ%
Blade Speed, wr or U [m/s]	161.9

Rotor Absolute Inlet Mach Number, M a3	1.189
Rotor Absolute Inlet Angle, O 3	73.69
Rotor Relative Inlet Mach Number, M r3	1.269
Rotor Relative Inlet Angle, B 3	59.52
Rotor Absolute Exit Mach Number, M a4	Ø.738
Rotor Absolute Exit Angle, O 4	-33.88
Rotor Relative Exit Mach Number, M r4	1.235
Rotor Relative Exit Angle, B 4	-6Ø.39

Total Pressure Ratio	Ø.2591
Total Temperature Ratio	Ø.7699

Table 4-2: Summary of Turbine Midspan Velocity
Triangle at 1ØØ% Corrected Speed

In the following section, we present data at three points during the tests, as indicated in Figure 4-2, corresponding to three traverse positions. In the first position, at 292 msec,

CHAPTER 4

THE RESULTS -- FLOWFIELD MEASUREMENTS AND ANALYSIS

High-frequency measurements taken in the Turbine Blowdown Facility are described in this chapter. After their description, the data are briefly analyzed in two ways. First, the effect of using time-resolved pressure measurements to estimate turbine performance (instead of using the time-averged pressure as measured by a Pitot probe) is investigated. Second, we derive the Euler turbine equation and use it in conjunction with the angle probe measurements to calculate the turbine temperature profile. Subsequently, this calculated profile is compared to the measured temperature profile taken with the aspirating probe. Before describing the measurements and presenting their analysis, however, the test matrix completed for this thesis is outlined.

4.1 Experiment Summary

The tests reported in this thesis are summarized in Table 4-1 below:

Test	Corrected Speed	Initial Temperature, K	Initial Pressure, atm
1	NC = 100%	475.5	4.134
2	NC = 100%	472.8	4.137
3	NC = 125%	486.7	4.137
4	NC = 80%	476.1	4.137

Table 4-1: Summary of Test Conditions

3.4 Summary of Shock Tube Results

The shock tube proved to be a usefull and easily implemented tool for determining the frequency response characteristics of both the aspirating probe and angle probe. The aspirating probe's undamped natural frequency was found to be 15.46 kHz for the turbine test conditions with a damping ratio of .36. The angle probe's characteristic frequency was estimated to be 45.5 kHz with a measured rise time of 5 usec. These results confirm each probe's applicability for use in the turbine facility. Measurements performed by the probes in the turbine facility, along with their analysis, are discussed in the following chapter.

is suitable for use in the turbine. (It is noted in [1], however, that this probe's 'reduced frequency' is only 12 kHz).

The characteristic frequency above notwithstanding, we must still determine the dynamic interaction of the probe's set of pressure transducers. In practice, the measurements of each transducer at some instant in time are reduced to obtain flowfield properities which are assigned to that instant in time. Clearly, errors will occur if, due to the probe's geometry and location of the stagnation point, unsteady flowfield conditions persist. Vortex shedding or intermittant flow separation are examples which might occur. Unfortunately, no techniques are currently available for generating well-characterized temperature and pressure fluctuations at frequencies greater than 10 kHz [20]; hence, we cannot investigate the probes response to a fluctuating flowfield. We can, however, measure the angle probes response to a step change in pressure and in so doing determine its rise time. These measurements are now presented.

3.3.2 Measurement of Angle Probe Frequency Response

The angle probe was placed in the shock tube and tested in air. In all cases, we were able to excite the natural frequency of the angle probe pressure transducers, which are on the order of 200 kHz. A typical pressure transducer response is illustrated in Figure 3-8. Rise times of the pressure transducers were found to be on the order of 5 usec with settling times on the order of 180 usec.

the angle probe pressure transducers are addressed and
followed by a brief presentation of the angle probe rise time
measurements.

3.3.1 Angle Probe Dynamic Coupling

Four miniature silicon diaphragm pressure transducers
(Kulite XCQ-093) are mounted on the angle probe as shown in
Figure 2-7. These transducers have natural frequencies on the
order of 200 kHz, or higher, depending on their rated
pressure. In using the probe for flowfield measurements,
however, we are more interested in the dynamic interaction of
the entire set of transducers since they are used together to
retrieve flowfield properties.

A characteristic frequency of the angle probe can be
found based on the probe diameter and anticipated flowfield
conditions downstream of the turbine rotor as shown in Table
3-4 below:

```
-----------------------------------------
Probe diameter, D          [MM]        3.30

Mach Number                            0.60
Temperature, T             [K]       355.0
Gamma                                  1.29
Gas Constant, R        [J/KG K]      137.0
Velocity, V                [M/S]     150.3
-----------------------------------------
Characteristic
Frequency, F = V/D      [kHz]         45.5
-----------------------------------------
```

Table 3-4: Angle Probe Characteristic
            Frequency

Based on this simple characteristic frequency, the angle probe

limiting characteristics associated with the hot wires themselves become important. The minimum wire length-to-diameter ratio required for negligible conduction losses to the probe body is 200 to 500 [32]. And given that the smallest available hot wires are 2.5 to 5.0 um in diameter, the minimum probe channel diameter becomes essentially set at 0.5 to 1.0 mm. We may then choose the area of the sonic orifice, consistant with construction limitations, so as to give a low channel Mach number. Thus, we can limit the adverse effect of the subsonic mean flow on the probe natural frequency. Though the applicability of equation 3.8 is questionable, it at least suggests that a low Mach number will also reduce the level of damping introduced by the flow.

In effect, the channel length of the probe is the primary variable controlling the natural frequency. Consideration must be given to the inlet design to ensure good off-angle performance and a smooth diffusion of the flow into the constant area channel. But in theory, it seems the designer need only chcose a length commensurate with construction constraints to obtain the desired natural frequency. In the present case, where we would like a natural frequency of 40 to 60 kHz, we would need to reduce the probe's channel length by one-half or more.

3.3 Angle Probe Frequency Response

Frequency response aspects of the angle probe are discussed in this section. In particular, dynamic coupling of

unreasonable, though, because at the blade passing frequency it yields a magnification ratio of only 1.2, approximately.

In summary, the natural frequency and damping ratio of the aspirating probe have been measured in both air and freon-12. The results confirm the applicability of equation 3.7 for predicting undamped natural frequency, but suggest that equation 3.8, the damping ratio prediction, is not applicable. From these results, the aspirating probe's predicted characteristics for the argon-freon-12 mixture used in the TBF are f=15.36 kHz and z=0.36. The damping ratio is an approximation based on the measured results. It is felt that these values of natural frequency and damping ratio are sufficient to measure the blade-to-blade temperature and pressure distributions downstream of a turbine rotor. Given these results, methods for improving the aspirating probe frequency response are now considered.

3.2.4 Design Considerations for Frequency Response Improvement

The aspirating probe natural frequency is a function of its channel length, the sonic speed, and the channel Mach number, as was shown in equation 3.7. The sonic speed is a function of the test gas and temperature, and therefore, more an application than design consideration. So on a next iteration of the aspirating probe design, we are left with only the channel length and channel Mach number (a function of channel-to-sonic-orifice area ratio) as design variables for improving the natural frequency.

In considering a design for improved frequency response,

0.32, is shown in Figure 3-7.

We may now predict the aspirating probe's frequency response for the TBF's argon-freon-12 test gas mixture. Results for a freon-12 mass fraction of 0.511% are shown in Table 3-3 below:

```
-------------------------------------------------
Test Gas                          Argon - Freon-12
-------------------------------------------------
Channel length, L        [MM]            3.886
Temperature, T           [K]            355.0
Freon mass fraction      [%]             0.511
Gas constant, R    [J/KG K]            137.0
Gamma                                    1.29
Sonic speed, C          [M/S]          250.4
Channel Mach number, M                   0.2
-------------------------------------------------
Natural Frequency, f [kHz]              15.46
Damping Ratio, z                         0.36
 (approximated from measurements)
-------------------------------------------------
```

Table 3-3:   Aspirating Probe Natural Frequency
             and Damping Ratio Prediction in an
             Argon-Freon-12 Mixture

The prediction above is based on the typical DC value for temperature downstream of the turbine rotor. The damping ratio shown is an approximation based on the values measured for air and freon-12. The natural frequency of 15.46 kHz is well above blade passing frequency, but is not nearly high enough to investigate wake structure. It is felt, though, that this natural frequency and damping ratio pair are sufficient to distingiush blade-to-blade variations in temperature and pressure. The damping ratio of 0.36 is rather less than the optimum value of 0.6 to 0.7. It is not

The predicted and measured undamped frequencies agree very well, thus giving credibility to equation 3.7. The variance in the freon-12 measurement and prediction is most likely associated with the presence of air in the driven tube during the test. The air would alter the driven gas properties, resulting in a higher natural frequency similar to that measured. Unfortuneately, the damping ratios do not agree. The prediction gives a damping ratio close to the critical value of $z=1$; a value for which we would expect to see no oscillations in the signal. Clearly the damping ratio prediction, equation 3.8, is not applicable to the aspirating probe.

The frequency response of a simple hot wire similar to that used in the aspirating probe was also measured in the shock tube. Tests were accomplished in air for the same diaphragm pressure ratio and temperature as used with the aspirating probe. This was done to ensure the measured frequencies were a function of the aspirating probe geometry and gas properties alone, and not associated with the hot wire circuitry or shock tube itself. Based on the stability setting of the anemometer circuit, damped natural frequencies of 45.0 to 65.0 kHz were observed for the simple hot wire. These values are well above those measured for the aspirating probe and further tend to verify Whiteheads result for predicting natural frequency. A typical hot wire response, a natural undamped frequency of 59 kHz and damping ratio of

frequency is always less than the undamped natural frequency. We can, however, extract the required information using the following relationships and definitions given in Figure 3-6 [31]:

$$z = \sqrt{\frac{1}{\left(\frac{\pi}{\ln a/A}\right)^2 + 1}} \qquad [3.10]$$

$$wn = \frac{2\pi}{T\sqrt{1-z^2}} \qquad [3.11]$$

Using the equations above and the measurements in Figures 3-4 and 3-5 , we obtain the results shown in Table 3-2 below.

Test Gas		Air	Freon-12
a	[Volts]	0.52	1.28
A	[Volts]	0.14	0.44
Period, T	[Microsec]	55.0	95.0
Predicted damping ratio, z, from 3.8		0.97	0.89
Measured damping ratio, z, from 3.10		0.39	0.32
Predicted undamped natural frequency, f from 3.7	[kHz]	21.63	9.53
Measured undamped natural frequency, f from 3.11	[kHz]	21.35	11.11

Table 3-2: Comparison of Predicted to Measured Aspirating Probe Natural Frequency and Damping Ratio

With the natural frequency and damping ratio predicted, the task is now to measure these characteristics of the probe and compare the measurements to the predictions. If they agree, we may use equations 3.7 and 3.8 to predict the probe's frequency response in argon-freon-12.

The aspirating probe was mounted in the shock tube test facility and subjected to step-function changes in both pressure and temperature. Separate tests were accomplished in both air and freon-12 at diaphragm pressure ratios of approximately 1.5, yielding pressure ratios at the probe of about 1.25. This level of pressure change is similar to what the probe would experience downstream of the turbine rotor in the TBF. Typical probe responses to the step change in properties, along with their respective power spectrums, are given in Figures 3-4 A and B for air and Figures 3-5 A and B for freon-12. Test conditions are noted on each figure.

We can determine the aspirating probe's natural frequency and damping ratio from Figures 3-4 and 3-5. First, it must be realized that a systems undamped natural frequency cannot be observed experimentally unless the system has zero damping. What is actually observed is the damped natural frequency which is related to the undamped natural frequency as follows [30]:

$$w \text{ damped} = w \text{ natural} \sqrt{1-z^2} \qquad [3.9]$$

This result applies only to underdamped systems where z < 1.0. From equation 3.9 it is clear that the experimentally observed

temperature. No attempt was made to determine the flowfield total temperature and pressure with the hot wires alone. On each figure listed in Table 4-3, the total pressure ratio and total temperature ratio measured from each wire are plotted against time. For the 100% corrected speed condition, an additional figure is given which compares the ensembled and instantaneous temperature signals. The second time point (360 msec) for each speed condition varies slightly. This is due to differences in the probe traversal from test to test--the probe position is the same for each data set.

In theory, the temperature reduced from each hot wire should be the same. In practice, they vary slightly. Maximum differences in temperature between the two wires is on the order of 18 C, but these occur in the peaks and valleys of the ensemble averages. Generally, the form of the ensembled temperature traces agree very well. The temperature sensitivities of the wires are different, as mentioned in Chapter 2, but the calibration data should negate this effect. Except that the wires are spatially separated (radially in reference to the blade trailing edge, and only 1% in blade span), no explanations for the differences in probe output are given here.

For the 100% corrected speed condition, the temperature ratio is seen to have a characteristic frequency twice that of blade passing. This is most clearly evidenced in the 292 msec and 430 msec test points. The peak-to-peak variation is typically 20%, or 65 C. The ensembles from these test points compare very favorably with their instantaneous temperature

traces. During the traverse, however, the temperatures are not so cleanly structured. Ensembling the data over seven cycles instead of 37 produces the same result, as is shown in Figure 4-7B. This suggests there is not a problem with the ensembling technique; rather, the temperature in the vane wake region has a more random structure. This random nature is seen in Figure 4-10, where it is clear that the ensemble averages do not agree well with the instantaneous measurements. For all the test points, the peak in total temperature ratio corresponds roughly with the trough in total pressure ratio. And assuming the wake is signalled by low total pressure, the data suggest the wakes are hot.

For the 125% operating condition, we see again the twice blade-passing frequency of the temperature profile. The amplitude of the second peak is less pronounced, however, than in the 100% speed case. The maximum peak-to-peak temperature variation for this speed is roughly 25%, or 70 C. The phase relationship between the pressure and temperature has changed from the 100% speed condition. Now, the trough in total temperature lines up more closely with the trough in total pressure.

Finally, for the 80% operating condition, we see temperature profiles which are much less consistant than those from the other operating conditions. The profiles contain frequency components at three times blade-passing and greater with a different structure at each test point. Further correlation is required for this data set, but it has not been accomplished for this thesis. Typical peak-to-peak

temperature variation is 11%, or 37 C. And like the 100% corrected speed case, the temperature ratio is seen to vary alternately with the pressure ratio.

4.2.3 Angle Probe Measurements

Total and static pressure ratios, Mach numbers, and tangential flow angles reduced from the angle probe pressure measurements are presented in this section. These measurements are used later with the Euler turbine equation to predict the rotor exit temperature profile. Unfortuneately, during the course of testing, the angle probe's transducer number 4 became intermittant. As a result, no radial flow information was obtained. The angle probe was not traversed during the tests. Its stationary position corresponds to the 360 msec test point for the traversed probes. Finally, only the measurements from the 100% corrected speed condition are presented here.

Both the absolute and relative tangential flow angles are plotted in Figure 4-19. The relative angle is calculated using the absolute Mach number and tangential angle measured by the angle probe, along with the wheel speed. The probe was offset from axial in the laboratory frame by 34 degrees so as to face directly into the flowfield. The streamline curvature program mentioned in Section 4-1 predicts values of 34.88 and -60.39 for the absolute and relative tangential angles respectively. From the Figure, it is seen that the absolute tangential flow angle has a peak-to-peak variation of 30 degrees, with the mean value corresponding to the streamline

curvature prediction. Likewise, the relative tangential angle has a significant peak-to-peak variation of 15 degrees. This is interesting since it is normally assumed that the relative tangetial flow angle is constant except for a small deviation angle at the blade trailing edge.

The total pressure ratio and absolute Mach number are shown in Figure 4-20. In Figures 4-21 and 4-22, the axial Mach number and tangential Mach number, respectively, are shown with the total pressure ratio. And in Figure 4-23, the axial and tangential Mach number components are plotted togethor. From Table 4-2, the predicted absolute exit Mach number is 0.738 for the blade midspan. This indicates the DC value for the measured absolute Mach number is low by approximately 10%. From Figure 4-20, we see the trough in absolute Mach number lines up with the minimum total pressure as one would expect. The Mach number trace, though generally increasing with time, .i.e from the blade pressure to suction side, is very non-uniform. This aspect of the Mach number profile was unexpected and requires further analysis. The axial and tangential Mach number components are seen to be 180 degrees out of phase, with the minimum in axial Mach number occurring at the minimum total pressure. In contrast, the maximum tangential Mach occurs at the pressure minimum.

Finally, the total pressure ratio and static pressure ratio are shown together in Figure 4-24. Surprisingly, the static pressure has roughly the same blade- to-blade profile as the total pressure. Clearly, the static pressure is not constant through the wake region as is normally assumed.

4.2.4 Total Pressure Probe Measurements

The Kulite XCQ-Ø62 is the smallest pressure transducer available which provides accurate DC and AC pressure measurements. A total pressure probe containing this transducer yields the pressure measurements shown in Figure 4-25. In this figure, both the ensembled and instantaneous traces are shown. On the figure's lower grid, the ensembled pressure ratio measured by the probe is superimposed on an ensembled trace taken by the aspirating probe's XCQ-Ø93 transducer. The measurements were taken in the same position and test time but in different tests. The form of the ensembled pressure traces are quite similar. Each show a strong pressure fluctuation at the blade passing frequency with a smaller amplitude frequency superimposed. This secondary frequency is most likely associated with the blade passage vortex. The time-resolved pressure measurement obtained with the XCQ-Ø62 is employed in the following section to investigate turbine performance.

4.3 Data Analysis

In this section, the practice of using time averaged pressures to calculate turbine performance is discussed in light of that component's characteristically unsteady flowfield. Comparison is made between the time-average of the time-resolved pressure signal described above, and the time-averaged pressure signal as might be measured by a Pitot probe. Next, the nondimensionalized Euler turbine equation is derived and used to show the dependence of the stage

temperature ratio on the blade turning angles, flow Mach numbers and rotor speed. Finally, comparison is made between the temperature profile calculated from the Euler turbine equation and that measured by the aspirating probe.

4.3.1 Fluctuating Pressure Influence on Performance Calculations

Adiabatic efficiency serves as a measure of turbine performance and can be defined as follows:

$$\eta_{ad} = \frac{\left\langle 1 - \frac{Tt4}{Tt3} \right\rangle}{\left\langle 1 - \frac{Pt4}{Pt3} \right\rangle} \qquad [4.1]$$

where Tt is the gas total temperature, Pt is the total pressure, and 3 and 4 refer to the rotor inlet and exit respectively. This formulation applies only for a mass-flow weighted average of the properties as indicated by the carats. If the variations in flow velocity and density are small then a time-weighted average of the properties may be used as an approximation to the mass-averaged values. Time-weighted averages will be used here.

Together, a Pitot tube, connecting lines, and an inert measuring instrument comprise an 'integrating pneumatic system' which can measure time-averaged pressures in fluctuating flows such as those downstream of a turbine rotor. In practice, such systems are commonly used in turbine test facilities to measure the time-averaged pressure which is then

used with Equation 4.1 to estimate the turbine performance. However, as shown by Weyer [33], measurements of this sort are subject to large errors which depend upon the strength of the pressure oscillations, the pressure wave shape, and probe construction. Figure 4-26 shows the deviation of an ordinary Pitot probe reading from the correct time- averaged pressure measured downstream of a transonic axial flow compressor. In this case, errors of up to 8% occur as the rotor speed, and hence flowfield fluctuations, increase (temperature measurement errors have also been noted but these are not addressed here). If taken on face value, the erroneous measurements would suggest a higher efficiency than the compressor actually possesses. We will investigate here the magnitude of similar errors which can occur in turbines.

The measuring system model described above, one consisting of a throttle point, connecting duct, and inert measuring instrument, will sense some time averaged pressure, Pbar, when immersed in a flowfield with fluctuating pressure, Pl(t). (Basically, Pbar is the 'probe averaged' pressure). A schematic of this measuring system is shown in Figure 4-27. A relationship between the mean pressure sensed by the measuring system, Pbar, and the actual time-varying pressure, Pl(t), is given by Weyer:

$$\emptyset = \sum_{i=1}^{i=k} \left\{ Pbar^{\frac{1}{\gamma}} \left[P1i^{\frac{2(\gamma-1)}{\gamma}} - (Pbar \; P1i)^{\frac{\gamma-1}{\gamma}} \right]^{\frac{1}{2}} \right\} \qquad [4.2]$$

$$- \sum_{i=k+1}^{i=2n} \left\{ P1i^{\frac{1}{\gamma}} \left[Pbar^{\frac{2(\gamma-1)}{\gamma}} - (Pbar \; P1i)^{\frac{\gamma-1}{\gamma}} \right]^{\frac{1}{2}} \right\}$$

where 2n is the number of identical time steps in a sampled
time interval, and k is the number of samples for which P1(t)
is greater than Pbar. As suggested by the definition of k,
the first term in Equation 4.2 applies when P1(t) is greater
than Pbar, the second when P1(t) is less than Pbar. Weyer's
derivation of this relationship is based essentially upon the
application of the Mass Conservation Principle across the
throttle plate shown in Figure 4-27, and is fully detailed in
[34].

Having measured the unsteady pressure downstream of the
test turbine, we can now time average it directly. Next, we
can use the same time-resolved signal to calculate Pbar from
Equation 4.2, with the result shown in Figure 4-28 [35]. For
this calculation, the pressure signal from the XCQ-062
pressure transducer is employed with averaging done over each
blade passing cycle. The difference between Pbar and the
correct time-averaged signal, Pavg, is also shown in Figure
4-28. Their difference is seen to fluctuate between $\pm$ 2.4%,
with a mean difference of -0.4%.

A streamline curvature program gives for the turbine
temperature and pressure ratios 0.7699 and 0.2591,
respectively, at 100% corrected speed. With these ratios and
1.3 for the test gas ratio of specific heats, we can use
Equation 4.1 to calculate the turbine adiabatic efficiency.
The result is 86.0%. Using the maximum difference between
Pbar and Pavg, we see that errors of 1.25 points in adiabatic
efficiency are possible. Realistically, though, the error

associated with the mean pressure difference is more likely to be realized. This error is only 0.25 points in adiabatic efficiency. It seems small, but is actually significant given the high premium on turbine adiabatic efficiency.

4.3.2 Euler Turbine Equation

The Euler turbine equation describes the energy transfer process in turbomachines and is obtained by equating the energy and momentum equations via the turbine power and torque. For the case of steady, two-dimensional, axisymmetric flow the Euler turbine equation takes the following form with the velocity triangle paramters defined in Table 4-2:

$$cp4\ T4 - cp3\ T3 = w\ (r4\ Vo4 - r3\ Vo3) \qquad [4.3]$$

where cp is the gas specific heat (a function of temperature), T the gas total temperature, w the rotor rotational speed, r the streamtube radius (which may shift with passage through the blade row), and Vo the tangential flow velocity. Stations upstream and downstream of the turbine rotor are denoted by 3 and 4 respectively.

We can redefine the rotor speeds, wr3 and wr4, and tangential flow velocities, Vo3 and Vo4, in Equation 4.3 in terms of Mach number:

$$\frac{wr4}{cp3\ T3} = \frac{Mtip\ (\gamma 3 - 1)\ \frac{r4}{rtip}}{\sqrt{\gamma 3\ R\ T3}} \qquad [4.4]$$

$$V_{\theta 3} = \frac{M3 \, \sin\theta 3 \, \sqrt{\gamma 3 \, R \, T3}}{\left(1 + \gamma\frac{3-1}{2} \, M3^2\right)^{1/2}} \qquad [4.5]$$

$$V_{\theta 4} = \frac{M4 \, \sin\theta 4 \, \sqrt{\gamma 4 \, R \, T4}}{\left(1 + \gamma\frac{4-1}{2} \, M4^2\right)^{1/2}} \qquad [4.6]$$

where M is the Mach number based on the local gas temperature, R the gas constant, and ν the ratio of specific heats. The blade tip Mach number, Mtip, is based on the vane inlet conditions. Incorporating these into Equation 4.3 yields:

$$1 - \frac{cp4}{cp3} \frac{T4}{T3} = \frac{Mtip \left(\gamma 3 - 1\right) \frac{r3}{rtip} \, M3 \, \sin\theta 3}{\left(1 + \gamma\frac{3-1}{2} \, M3^2\right)^{1/2}} \qquad [4.7]$$

$$+ \frac{Mtip \left(\gamma 3 - 1\right) \frac{r4}{rtip} \, M4 \, \sin\theta 4}{\left(1 + \gamma\frac{4-1}{2} \, M4^2\right)^{1/2}} \sqrt{\frac{T4}{T3}}$$

For a given set of flowfield conditions, the first term in the right hand side of Equation 4.7 can be considered a constant; the second a constant times the square root of the temperature ratio. After some manipulation, the equation can be reduced to the quadratic form from which the temperature ratio, T4/T3, is readily calculated. Clearly, we see the

turbine temperature ratio is a function of rotor speed, inlet and exit flow angle, and inlet and exit Mach number.

We can predict the rotor exit temperature profile with Equation 4.7 by using the Mach number and tangential flow angle measured by the angle probe. Unfortuneately, no vane exit measurements were taken, so the rotor inlet Mach number and tangential angle must be determined and input. These values, given in Table 4-2, are obtained with a streamline curvature program, input directly, and held constant.

The result of this calculation, the Euler total temperature ratio, is shown in Figure 4.29 along with the total pressure ratio measured by the angle probe. The Euler temperature profile varies at the blade passing frequency, unlike the measured profile which varies at twice that frequency. The amplitude of each is roughly the same, but the Euler profile is DC shifted upward 20% from the measured values. Finally, and again unlike the measured temperature, the Euler temperature ratio varies roughly in phase with the pressure ratio, with the lowest total temperature occurring approximately with the lowest total pressure. These discrepancies are only noted and not analyzed further in this thesis. Their occurrence, however, is not surprising since the Euler turbine equation as derived only applies to steady, two-dimensional, axisymmetric flow.

CHAPTER 5

THE CONCLUSIONS

Time-resolved flowfield measurements have been successfully taken in the MIT Turbine Blowdown Facility. The properties measured include total temperature, total pressure, static pressure, Mach number, and tangential flow angle. The original objectives were: to measure the blade-to-blade total temperature profile for subsequent comparision with a prediction by the Euler turbine equation; to determine the effect of using time-averaged pressures to calculate turbine performance; and to provide a complete set of time-resolved turbine stage data. No time-resolved turbine data are currently available in the literature. A preliminary objective was to determine the frequency response of the instrumentation employed to make the flowfield measurements. With these objectives in mind, the major results and conclusions of this thesis are now summarized.

First, we found the shock tube to be an easily implemented tool fo, investigating instrumentation frequency response characteristics. In particular, for the TBF test gas, the aspirating probe was found to have a natural frequency of 15.5 kHz with a damping ratio of 0.35. The angle probe was found to have a rise time of 5 μsec with a settling time of 18 usec. These characteristics of the aspirating probe and angle probe were satisfactory for attempting flowfield measurements in the turbine facility.

Second, the TBF and its complement of high-frequency response instrumentation allowed for detailed flowfield

measurements in a rigorously scaled test environment. As mentioned above, time-resolved measurements of total temperature, total pressure, static pressure, Mach number, and tangential flow angle were successfully obtained.

Third, the time-resolved pressure measured with a Kulite XCQ-062 pressure transducer was employed to investigate turbine performance calculations. Specifically, errors associated with using the time-averaged pressure from a standard pitot probe, instead of the true time-average, were shown to be on the order of 0.25 to 1.25 points in adiabatic efficiency.

Finally, the turbine exit total temperature was calculated using the Euler turbine equation in conjunction with the tangential angle and Mach number from the angle probe. The predicted profile varied only at the blade passing frequency, unlike the measured profile which had a characteristic frequency of twice blade passing. Further, the predicted profile was DC shifted upward 10%, although its peak-to-peak temperature change was roughly the same as that measured.

REFERENCES

1)   Epstein, A.H.,Guenette, G.R. and Norton R.J.G., "The MIT
     Blowdown Turbine Facility", ASME Paper 84-G -116, 1984.

2)   Greitzer, E.M., "An Introduction To Unsteady Flows in
     Turbomachines", NATO Advanced Study Institute on Thermo-
     dynamics and Fluid Mechanics of Turbomachinery, 17-28
     September 1984, Izmir, Turkey, pg. 8.1.1.

3)   Sieverding, C.H.,"Secondary Flows in Straight and Annular
     Turbine Cascades", NATO Advanced Study Institue on
     Thermodynamics and Fluid Mechanics of Turbomachinery, 17-
     28 September 1984, Izmir, Turkey, pg. 6.1.1.

4)   Kerrebrock, J.L., and Mikolajczak, A.A., "Intra-Stator
     Transport of Rotor Wakes and Its Effect on Compressor
     Performance", ASME Journal of Engineering for Power,
     Vol. 92, October 1970, pp. 359-368.

5)   Ng, W.F. and Epstein, A.H., "A Quasi-Three-Dimensional
     Model for Intra-Stator Transport of Rotor Wakes", Un-
     published Report, 1985.

6)   Binder, A., et al., "An Experimental Investigation Into
     the Effects of Wakes on the Unsteady Turbine Rotor Flow",
     ASME Journal of Engineering for Power, Vol. 105, No. 1,
     January 1983, pp. 40-46.

7)   Hodson,H.P., "Measurements of Wake-Generated Unsteadiness
     in the Rotor Passages of Axial Flow Turbines", ASME Paper
     84-GT-189, 1984.

8)   Doorly, D.J., and Oldfield, M.L.G., "Simulation of the
     Effects of Shock Wave Passing on a Turbine Rotor Blade",
     ASME Paper 85-GT-112, 1985.

9)   Sharma, O.P., et al., "An Experimental Investigation of
     the Three-Dimensional Unsteady Flow in an Axia. Flow
     Turbine", AIAA Paper 83-1170, 1983.

10) Ng, W.F., "Time-Resolved Stagnation Temperature Measure-
     ment in a Transonic Compressor Stage", MIT Gas Turbine
     Laboratory Report No. 177, October 1983.

11) Ng, W.F. and Epstein, A.H., "High-Frequency Temperature
     and Pressure Probe for Unsteady Compressible Flows",
     Review of Scientific Instruments, Vol. 54, No. 12.
     December 1983, pp. 1678-1683.

12) Goldstein, R.J, Fluid Mechanic Measurements, Chapter 4,
     "Thermal Anemometers", Hemisphere Publishing Corporation,
     1983.

13) Collis, D.C. and Williams, M.J., "Two-Dimensional Con-

AD-A158 092   TIME-RESOLVED FLOWFIELD MEASUREMENTS IN A TURBINE STAGE   2/2
               (U) AIR FORCE INST OF TECH WRIGHT-PATTERSON AFB OH
               J L HOLT JUN 85 AFIT/CI/NR-85-77T

UNCLASSIFIED   F/G 20/4   NL

END
FILMED

DTIC
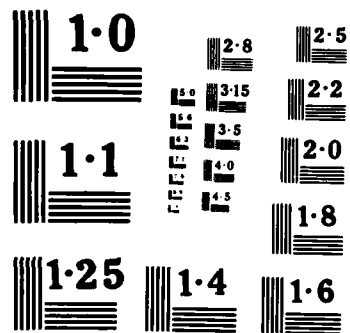
vection from Heated Wires at Low Reynolds Numbers",
Journal of Fluid Mechanics, Vol 6, 1959, p. 357.

14) Hilsenrath, NBS Cir 564, QC286.H655

15) "Thermophysical Properties of Refrigerants", ASHRAE 1976,
TP492.A54

16) Buddenberg, J.W. and Wilke, C.R., "Calculation of Gas
Mixture Viscosities", Industrial and Engineering Chem-
istry, Vol. 41, pp. 1345-1347.

17) Gertz, J.B., Private Communication.

18) Kerrebrock, J.L. et al, "A Miniature High Frequency
Sphere Probe", Proceedings of ASME Symposium, Measurement
Methods in Rotating Components of Turbomachinery, 1980.

19) Figueiredo, W.A., "Spherical Pressure Probe for Retriev-
ing Freestream Pressure and Directional Data", MIT Gas
Turbine Laboratory Report No. 137, August 1977.

20) Epstein, A.H., Private Communication.

21) Batchelor, G.K., An Introduction to Fluid Dynamics,
Section 6.6, Cambridge University Press, 1967.

22) Gamache, R.N., Private Communication.

23) Gertz, J.B., Private Communication, Angle Probe Data
Reduction Software.

24) Cao, Y., Radial and Circumferential Probe Traverser,
Unpublished Report.

25) Doebelin, E.O., Measurement Systems, Section 6.7,
"Dynamic Testing of Pressure-measuring Systems", McGraw-
Hill,Inc., 1975.

26) Anderson, J.D. Jr., Modern Compressible Flow, Chapter 7,
"Unsteady Wave Motion", McGraw-Hill, Inc., 1982.

27) Whitehead, D.S., "The Vibration of Air in a Duct with a
Subsonic Mean Flow", The Aeronautical Quarterly, Febru-
ary 1961, pp. 34-40.

28) Doebelin, E.O., Measurement Systems, Section 3.3,
"Dynamic Characteristics", McGraw-Hill,Inc., 1975, p.127.

29) Doebelin, E.O., Measurement Systems, Section 3.3,
"Dynamic Characteristics", McGraw-Hill,Inc., 1975, p.134.

30) Ogata, K., Modern Control Engineering, Section 6.4,
"Second-Order Systems", Prentice-Hall, Inc., 1970.

31) Doebelin, E.O., Measurement Systems, Section 3.3,
"Dynamic Characteristics", McGraw-Hill,Inc., 1975, p.195.

32) Blackwelder, R.J., "Hot-Wire and Hot-Film Anemometers", Methods of Experimental Physics: Fluid Dynamics, Edited by R.J. Emrich, Vol. 18, Part A, 1981.

33) Weyer, H.B., "Fundamentals of Flow Field Measurement Techniques", NATO Advanced Study Institute on Thermo-dynamics and Fluid Mechanics of Turbomachinery, 17-28 September 1984, Izmir, Turkey, pg. 4.2.1.

34) Weyer, H.B., "The Determination of Time-Weighted Average Pressures in Strongly Fluctuating Flows, Especially in Turbomachines", ESRO-TT-161, 1975.

35) Gertz, J.B., Private Communication, Computer Software.

(a) Rotor Wakes in Stator

(b) Velocities into Stator
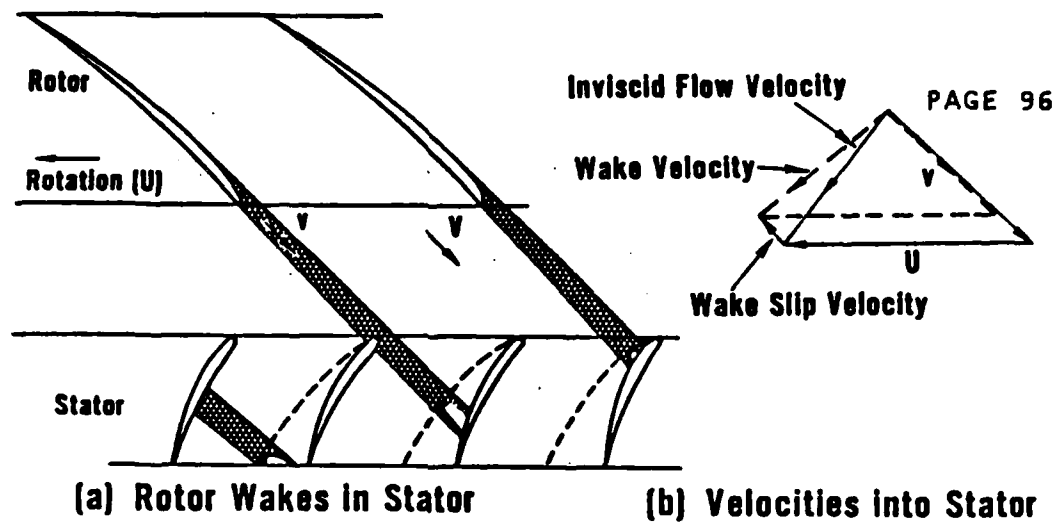
Figure 1-1A: Schematic of Compressor Stage Showing Rotor Wake in Stator [2]
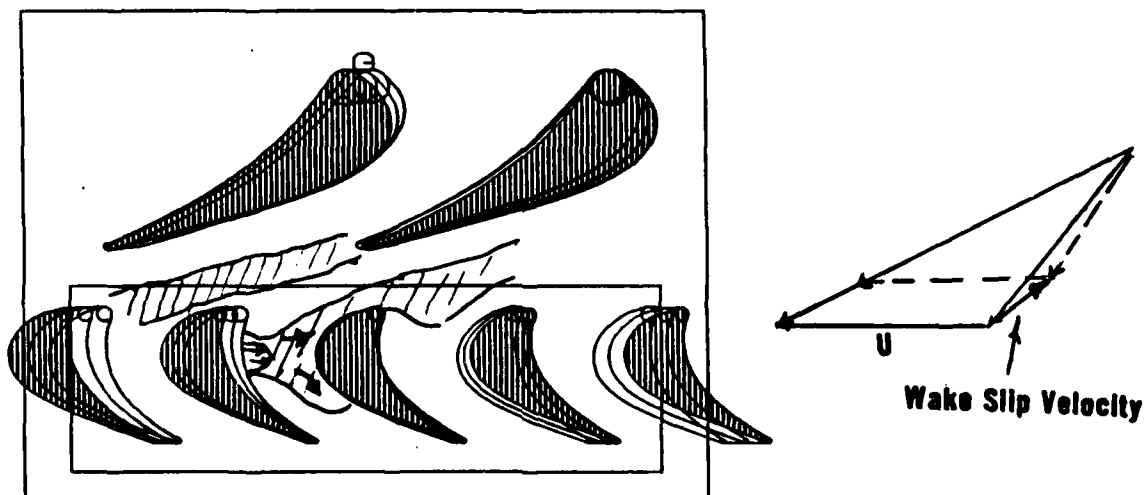
Figure 1-1B: Schematic of Turbine Stage Showing Vane Wake in Rotor

MIT BLOWDOWN TURBINE FACILITY

DUMP TANK

1 METER

TEST SECTION

VALVE

SUPPLY TANK
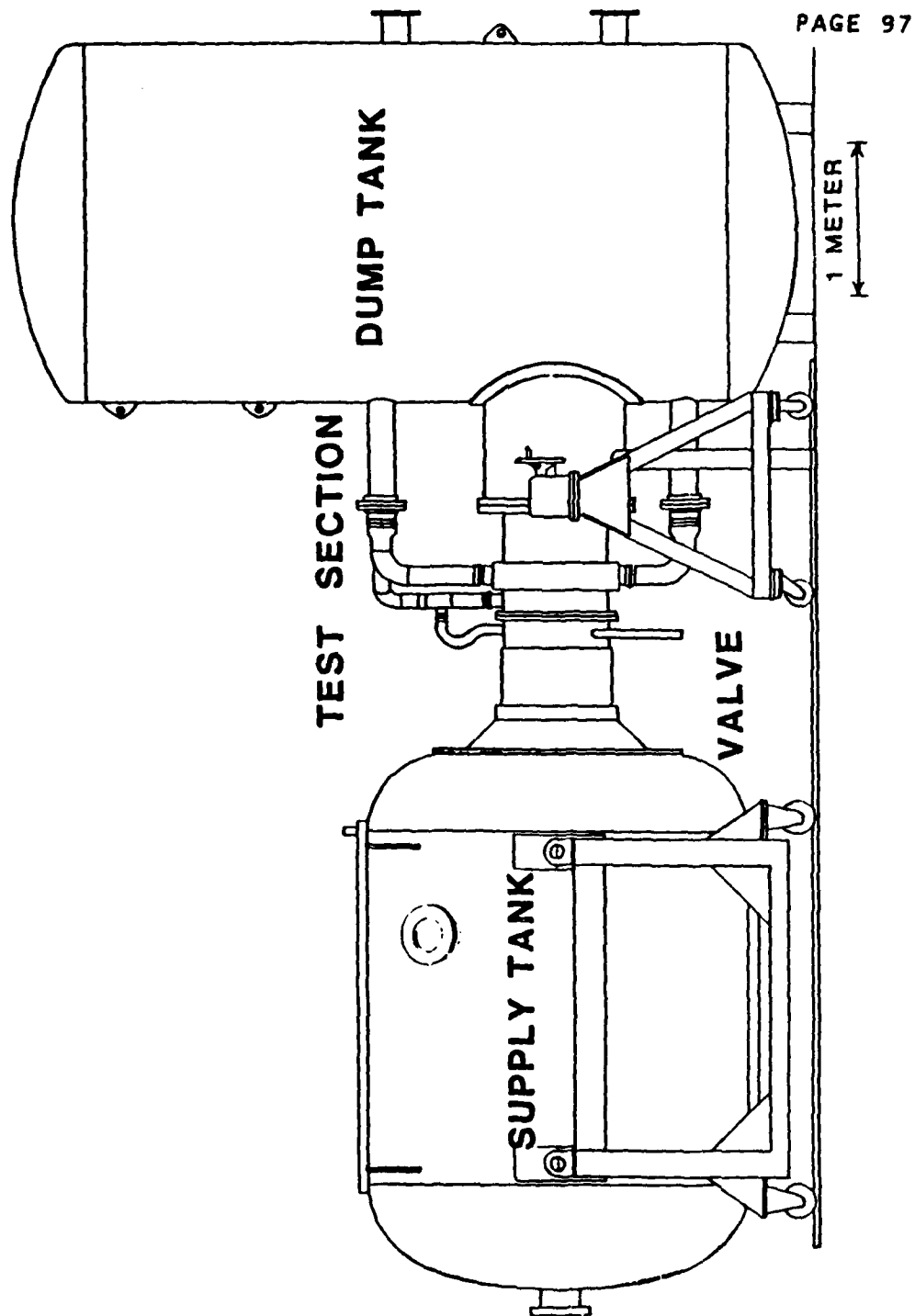
Figure 2-1:   Turbine Blowdown Facility Schematic
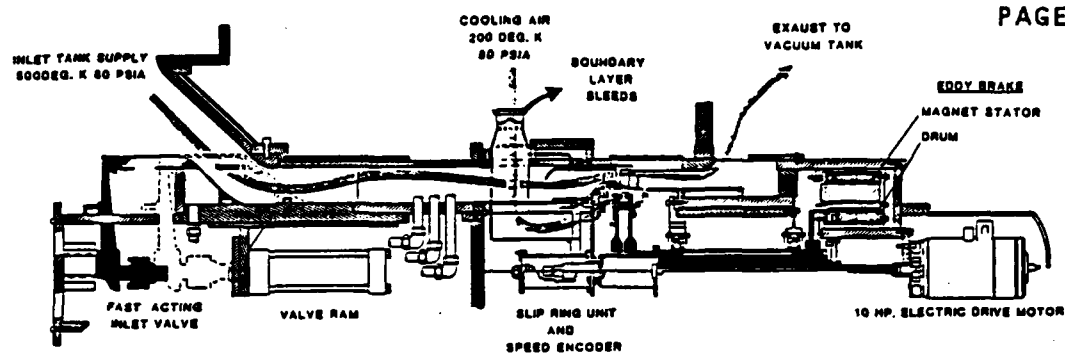
TURBINE FACILITY FLOW PATH
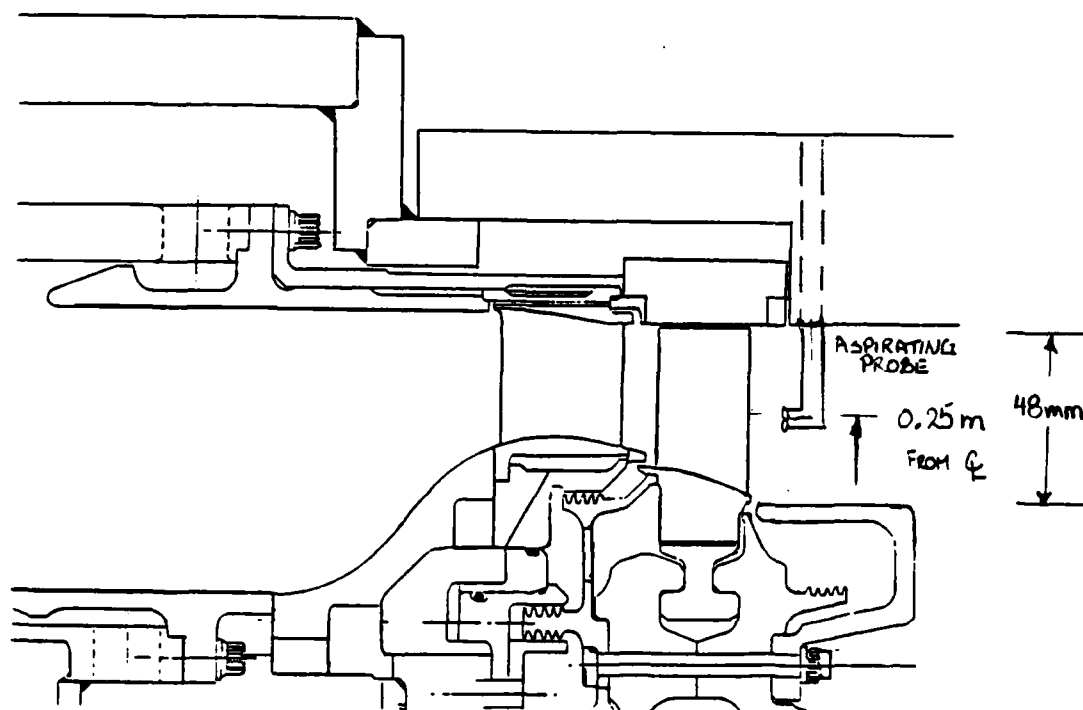
Figure 2-2: Test Section Schematic with Instrumentation
Locations
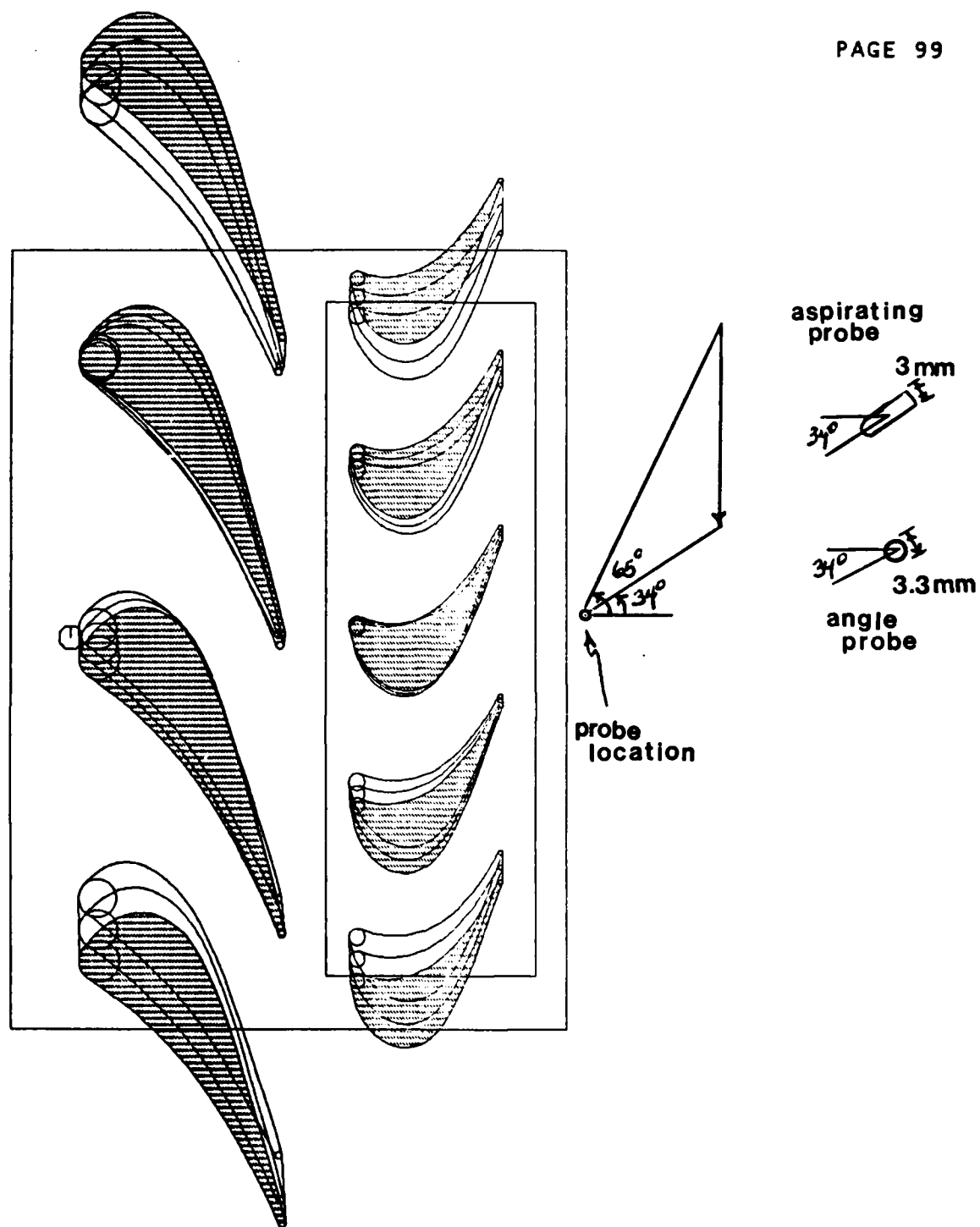
Figure 2-3:   Endview of Test Turbine with Scale Drawing
of Instrumentation
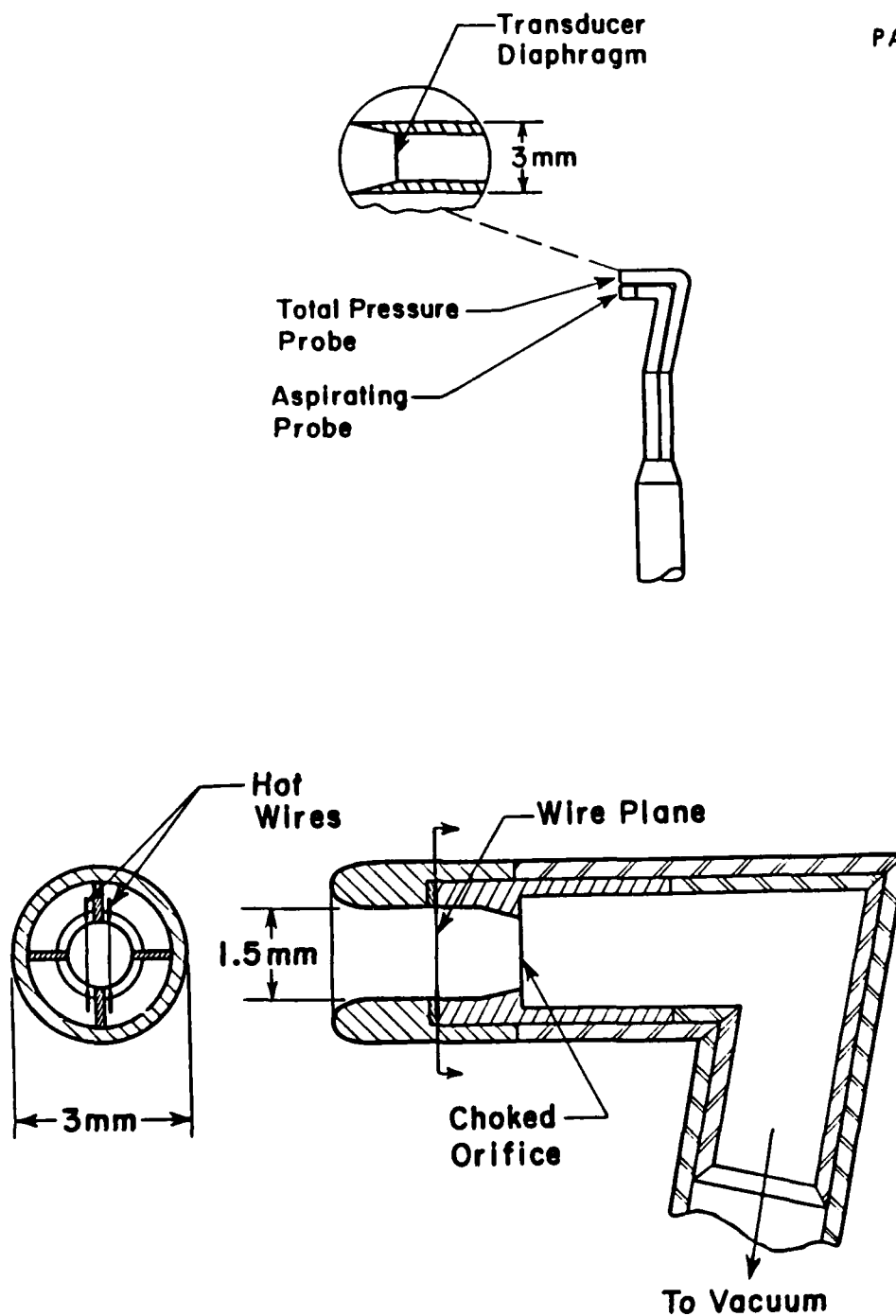
Figure 2-4:   Schematic of Aspirating Probe/Total Pressure
               Probe Assembly; Cross-Section of Aspirating
               Probe

ASPIRATING PROBE CALIBRATION/PREDICTION

$$V**2 = [(PT/SQRT(TT))**N*C+D](TW-R*TT)$$

CALIBRATED ☐

NPTS	= 11		LENGTH	= 1.2700	MM
OHR	= 1.80		DIAMETER	= 0.0051	MM
R25	= 2.98	OHMS	C CAL	= 0.318502	
TTOT	= 321.7	K	D CAL	= -0.026833	
TWIRE	= 491.1	K	N	= 0.30	
XFREON	= 0.5107		SD	= 0.23	C

PREDICTED △ (FLUID PROPERTIES UNCORRECTED)

NPTS	= 11		LENGTH	= 1.2700	MM
OHR	= 1.80		DIAMETER	= 0.0051	MM
R25	= 2.98	OHMS	C	= 0.318502	
TTOT	= 349.5	K	D	= -0.026833	
TWIRE	= 491.1	K	N	= 0.30	
XFREON	= 0.5107		SD	= 3.88	C
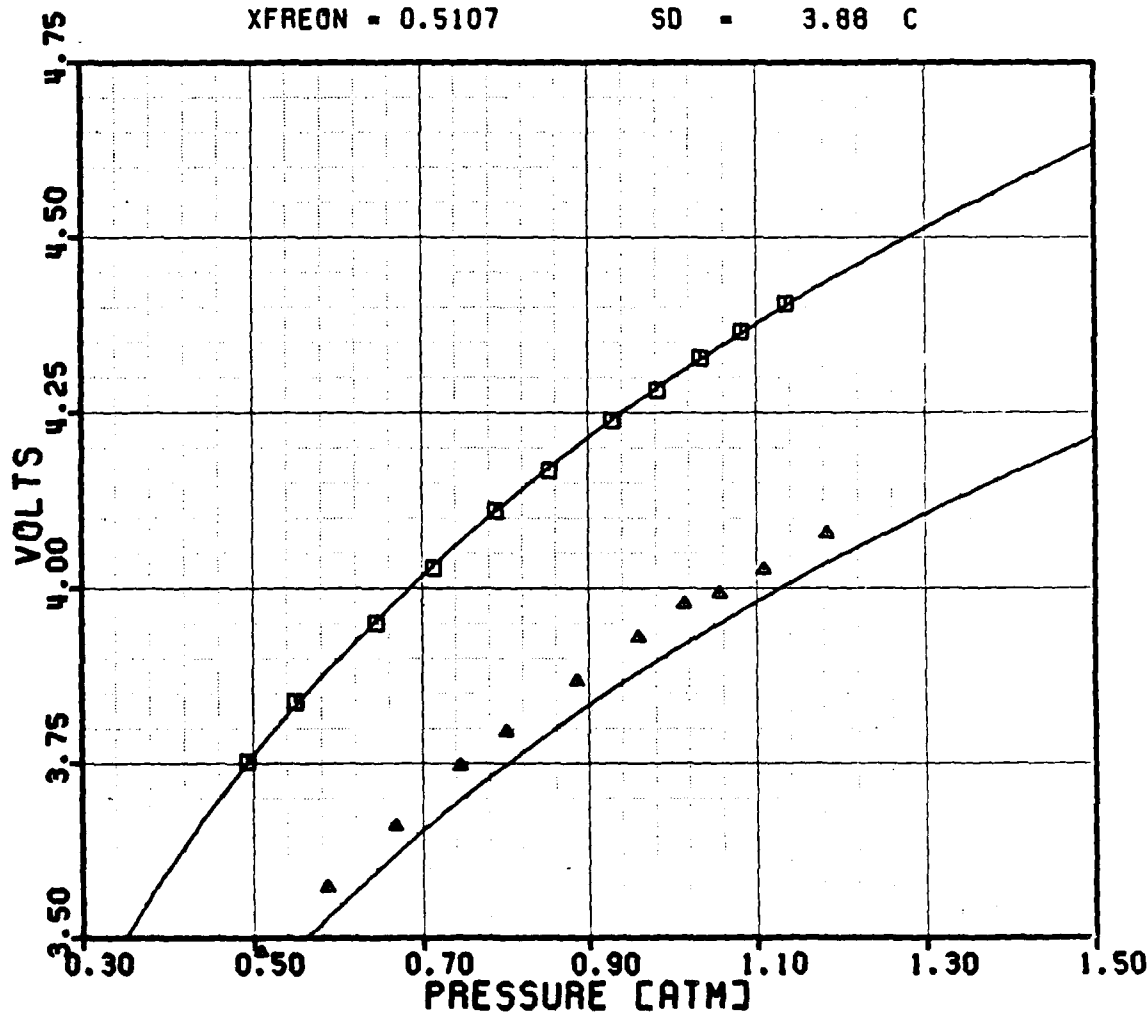
Figure 2-5A: Prediction of Aspirating Probe Calibration
Data With Uncorrected Fluid Properties.
Overheat Ratio = 1.8

ASPIRATING PROBE CALIBRATION/PREDICTION

$$V**2 = [(PT/SQRT(TT))**N*C+D](TW-R*TT)$$

CALIBRATED ☐

NPTS	= 11		LENGTH	= 1.2700	MM	
OHR	= 2.00		DIAMETER	= 0.0051	MM	
R25	= 3.27	OHMS	C CAL	= 0.285529		
TTOT	= 321.7	K	D CAL	= -0.029117		
TWIRE	= 539.4	K	N	= 0.30		
XFREON	= 0.5107		SD	= 0.44	C	

PREDICTED △ (FLUID PROPERTIES UNCORRECTED)

NPTS	= 11		LENGTH	= 1.2700	MM	
OHR	= 2.00		DIAMETER	= 0.0051	MM	
R25	= 3.27	OHMS	C	= 0.285529		
TTOT	= 349.5	K	D	= -0.029117		
TWIRE	= 539.4	K	N	= 0.30		
XFREON	= 0.5107		SD	= 4.63	C	
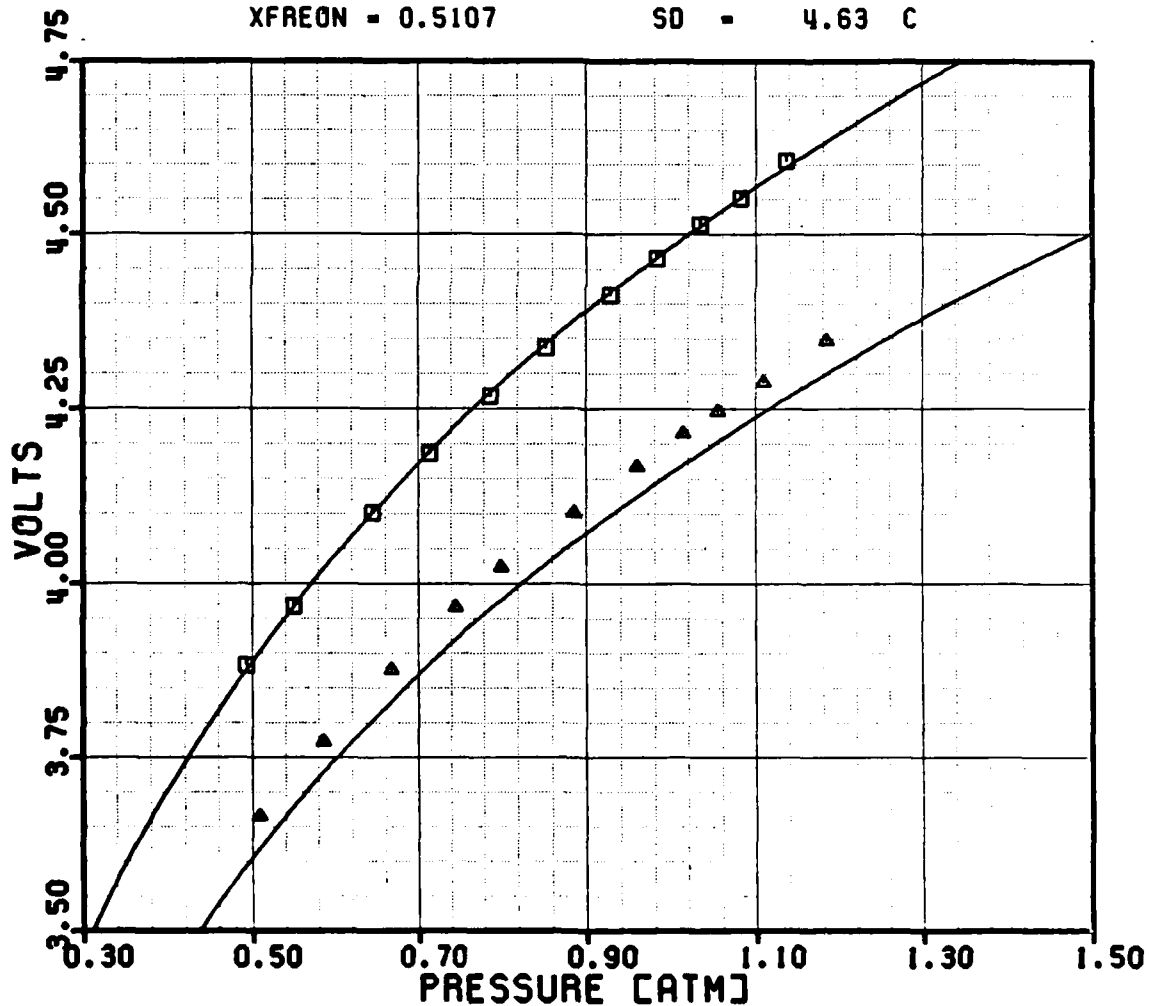
Figure 2-58: Prediction of Aspirating Probe Calibration
Data With Uncorrected Fluid Properties,
Overheat Ratio = 2.0

ASPIRATING PROBE CALIBRATION/PREDICTION

$$V**2 = [(PT/SQRT(TT))**N*C+D](TW-R*TT)$$

CALIBRATED ☐
     NPTS   = 11   LENGTH   = 1.2700   MM
     OHR   = 1.80   DIAMETER = 0.0051   MM
     R25   = 2.98   OHMS   C CAL = 0.318502
     TTOT   = 321.7 K   D CAL = -0.026833
     TWIRE = 491.1 K   N   =   0.30
     XFREON = 0.5107   SD   =   0.23 C

PREDICTED   △   (FLUID PROPERTIES CORRECTED - K AND MU)
     NPTS   = 11   LENGTH   = 1.2700   MM
     OHR   = 1.80   DIAMETER = 0.0051   MM
     R25   = 2.98   OHMS   C   =   0.326891
     TTOT   = 349.5 K   D   =   -0.027772
     TWIRE = 491.1 K   N   =   0.30
     XFREON = 0.5107   SD   =   0.52 C
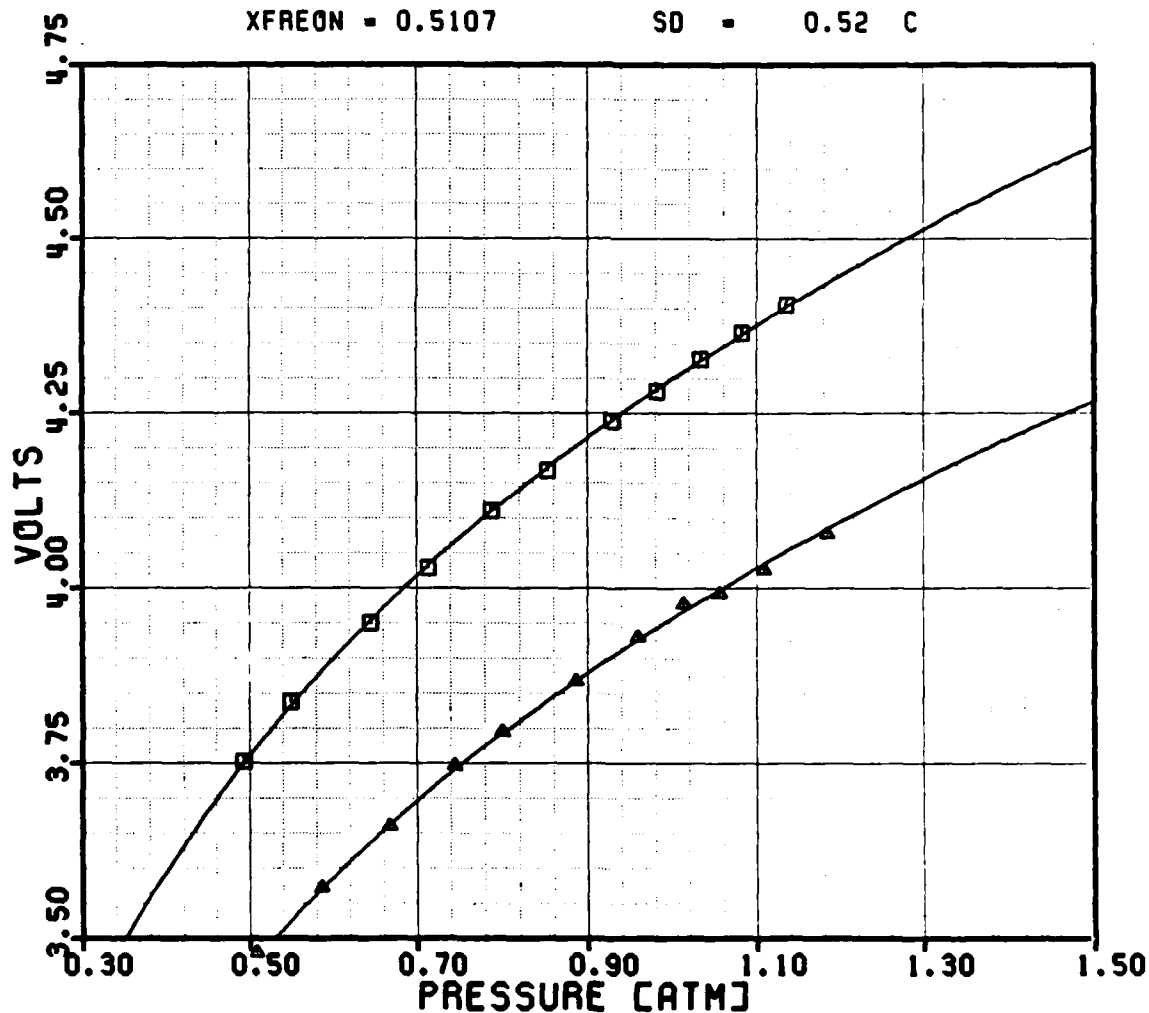
Figure 2-5C: Prediction of Aspirating Probe Calibration
               Data With Corrected Fluid Properties,
               Overheat Ratio = 1.8

ASPIRATING PROBE CALIBRATION/PREDICTION

$$V**2 = [(PT/SQRT(TT))**N*C+D](TW-R*TT)$$

CALIBRATED ▯

NPTS	= 11		LENGTH	= 1.2700	MM
OHR	= 2.00		DIAMETER	= 0.0051	MM
R25	= 3.27	OHMS	C CAL	= 0.285529	
TTOT	= 321.7	K	D CAL	= -0.029117	
TWIRE	= 539.4	K	N	= 0.30	
XFREON	= 0.5107		SD	= 0.44	C

PREDICTED △ (FLUID PROPERTIES CORRECTED - K AND MU)

NPTS	= 11		LENGTH	= 1.2700	MM
OHR	= 2.00		DIAMETER	= 0.0051	MM
R25	= 3.27	OHMS	C	= 0.292189	
TTOT	= 349.5	K	D	= -0.030033	
TWIRE	= 539.4	K	N	= 0.30	
XFREON	= 0.5107		SD	= 0.61	C
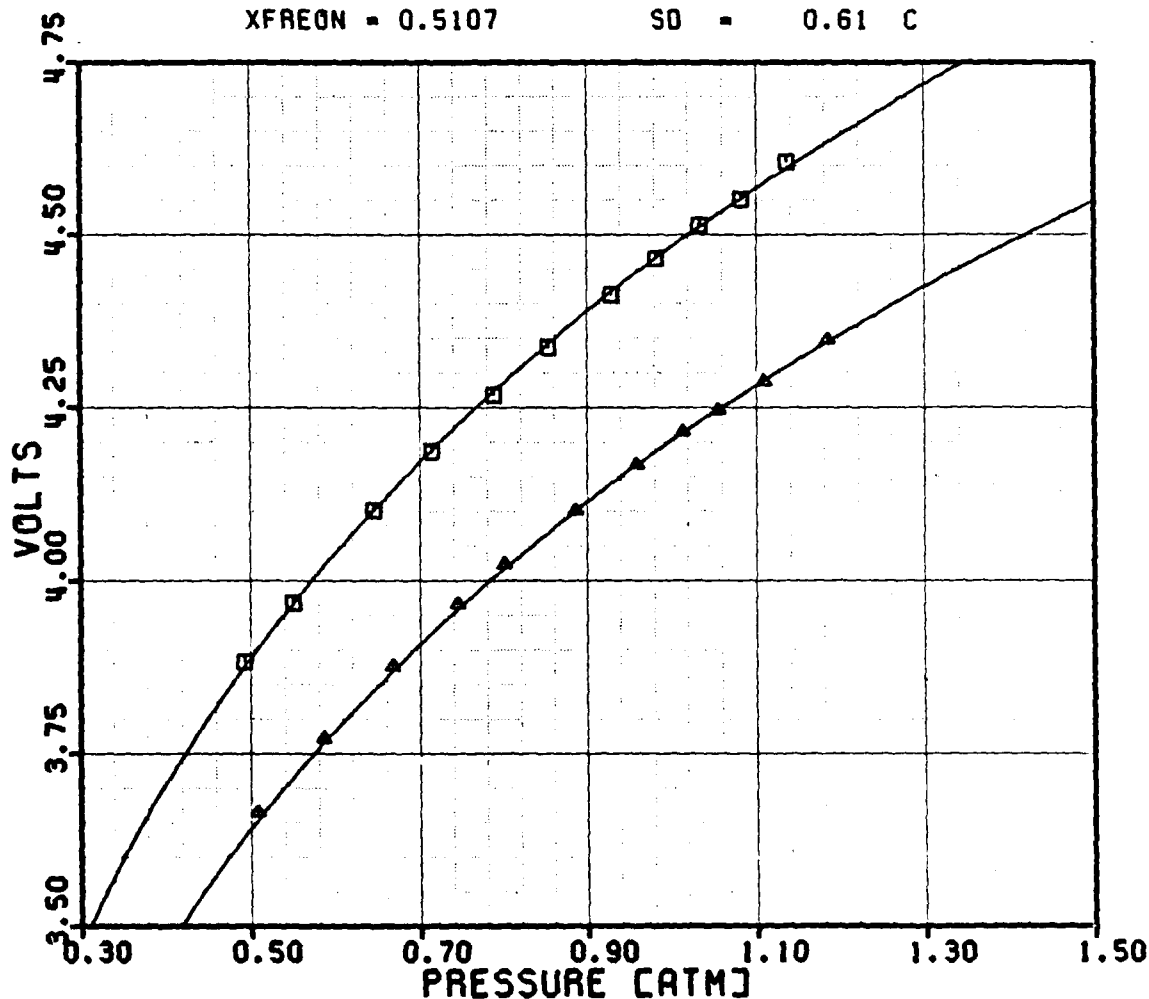
Figure 2-5D: Prediction of Aspirating Probe Calibration
Data With Corrected Fluid Properties.
Overheat Ratio = 2.0
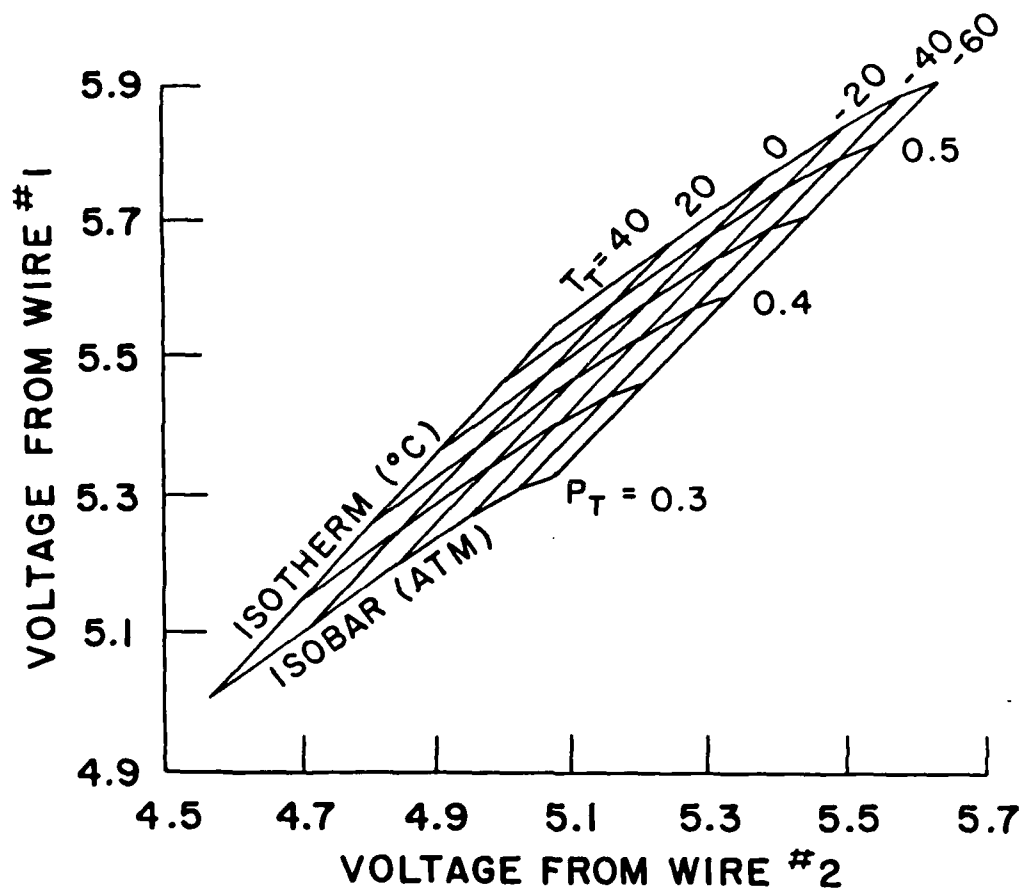
Figure 2-6: Aspirating Probe Combined Calibration
Map (from [10])

4-WAY PROBE CALIBRATION -- M=0.60

○ MACH NO. = 0.60   PHI = -10.000
▲ MACH NO. = 0.60   PHI = -5.000
+ MACH NO. = 0.60   PHI = 0.000
✕ MACH NO. = 0.60   PHI = 5.000
◆ MACH NO. = 0.60   PHI = 10.000
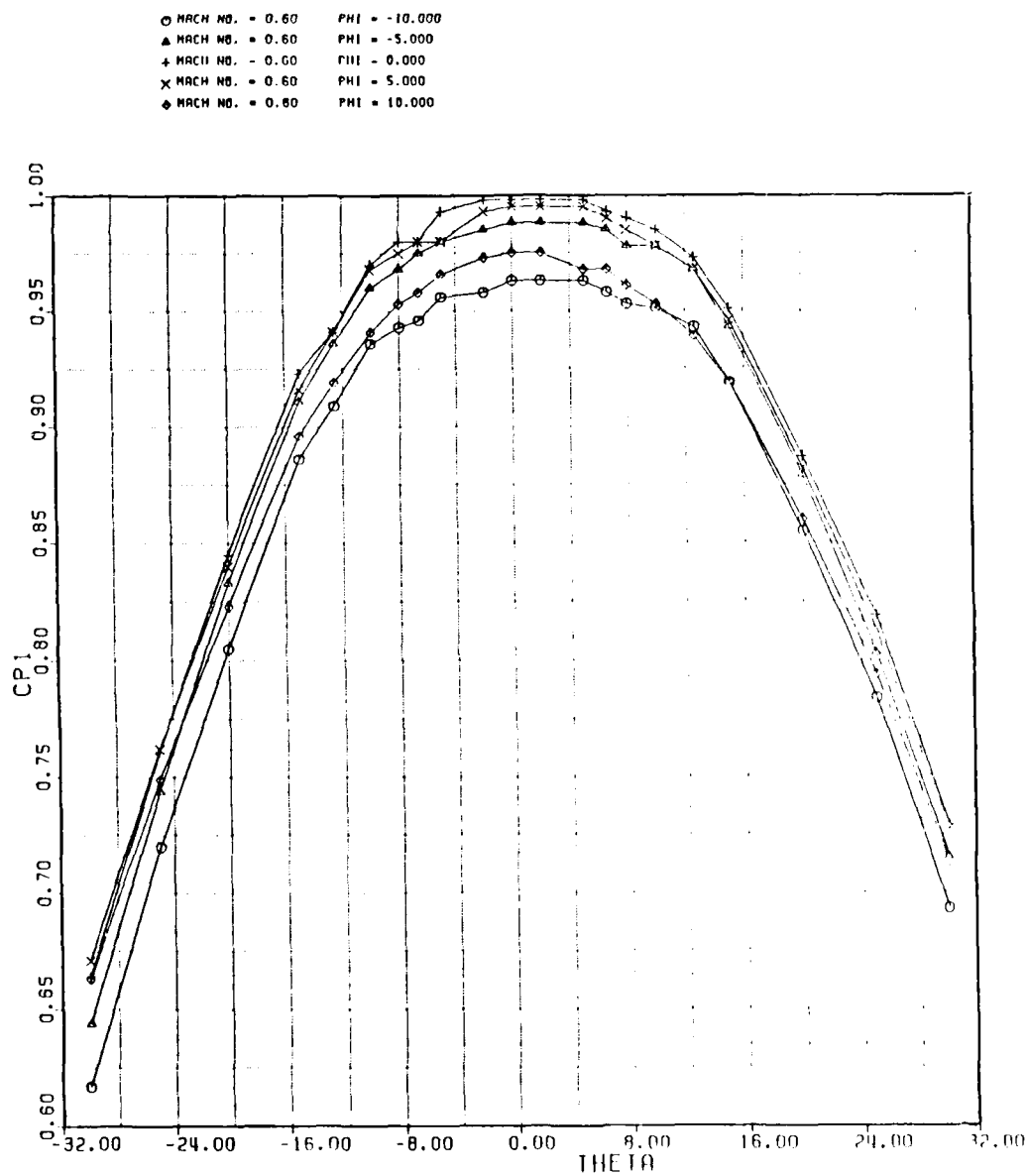
Figure 2-1:D: Angle Probe Coefficent Prediction,
                CP1 Versus Phi with Mach Number = 0.6

4-WAY PROBE CALIBRATION -- M=0.60

⊙ MACH NO. = 0.60	PHI = -10.000	
▲ MACH NO. = 0.60	PHI = -5.000	
+ MACH NO. = 0.60	PHI = 0.000	
✕ MACH NO. = 0.60	PHI = 5.000	
◇ MACH NO. = 0.60	PHI = 10.000	
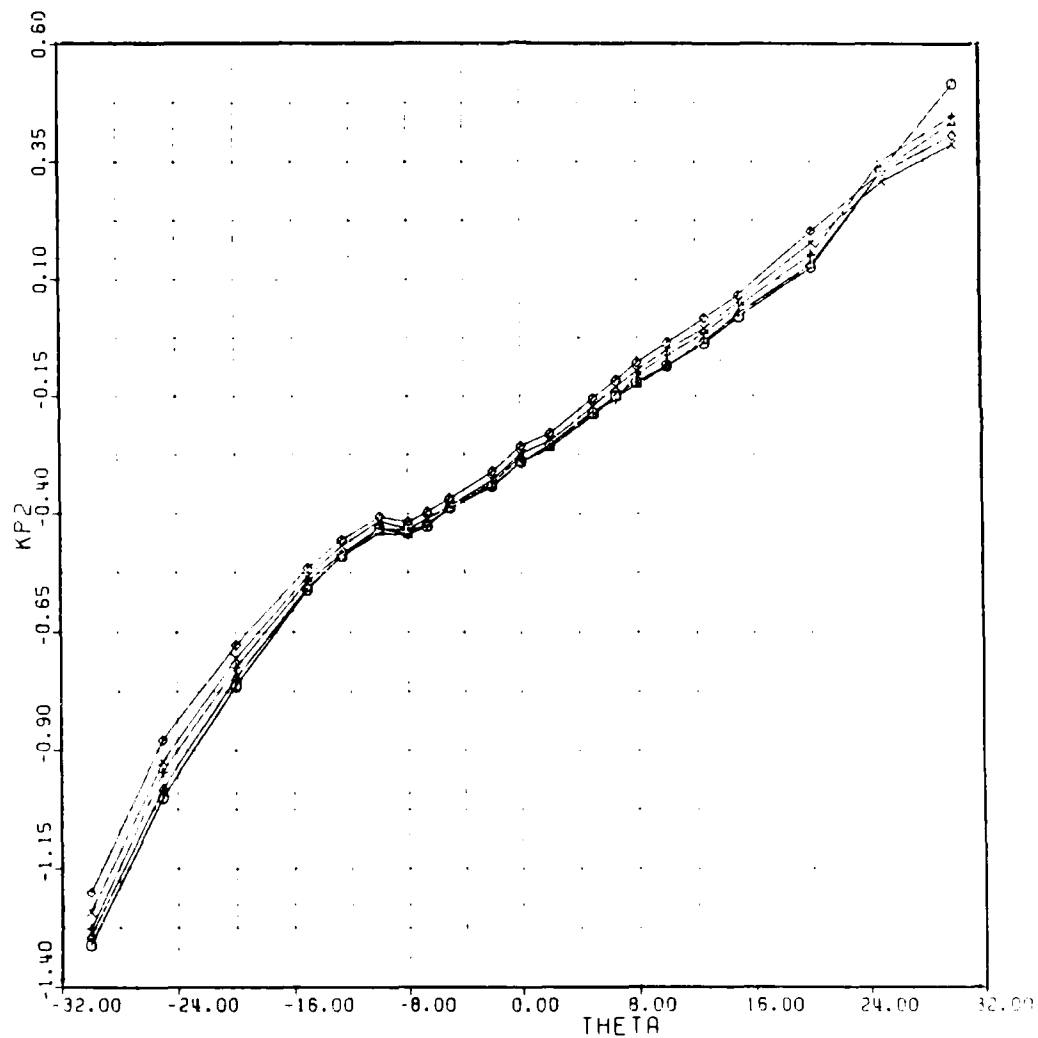
Figure 2-11C: Angle Probe Coefficent Prediction,
KP2 Versus Phi with Mach Number = 0.6

4-WAY PROBE CALIBRATION -- M=0.60

⊙ MACH NO. = 0.60	PHI = -10.000	
▲ MACH NO. = 0.60	PHI = -5.000	
+ MACH NO. = 0.60	PHI = 0.000	
✕ MACH NO. = 0.60	PHI = 5.000	
◇ MACH NO. = 0.60	PHI = 10.000	
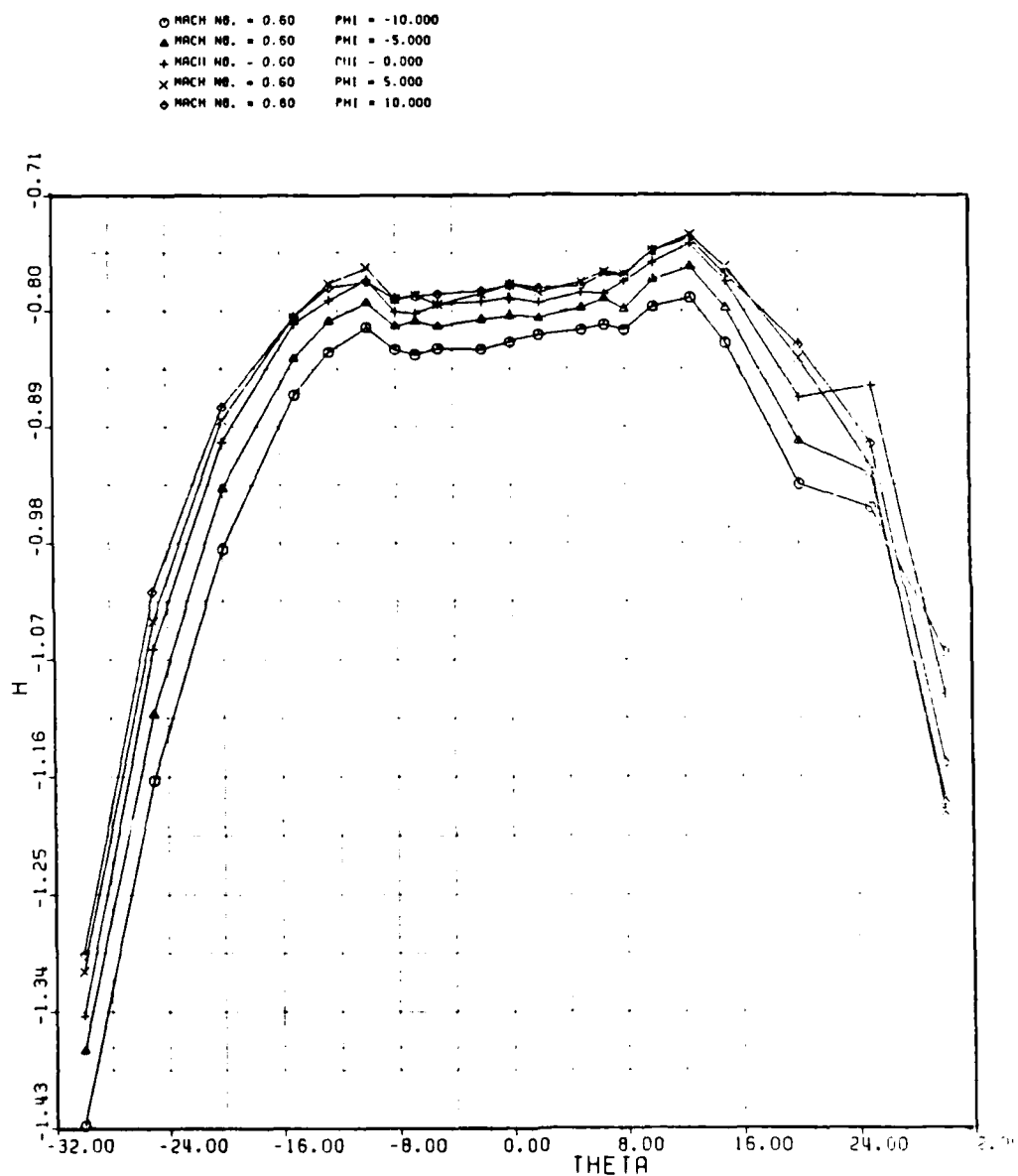
Figure 2-11B: Angle Probe Coefficent Prediction,
H23 Versus Phi with Mach Number = 0.6

4-W Y PROBE CALIBRATION -- M=0.60

○ MACH NO. = 0 60   PHI = -10.000
▲ MACH NO. = 0 60   PHI = -5.000
+ MACH NO. = 0.60   PHI = 0.000
× MACH NO. = 0 60   PHI = 5.000
◆ MACH NO. = 0.60   PHI = 10.000
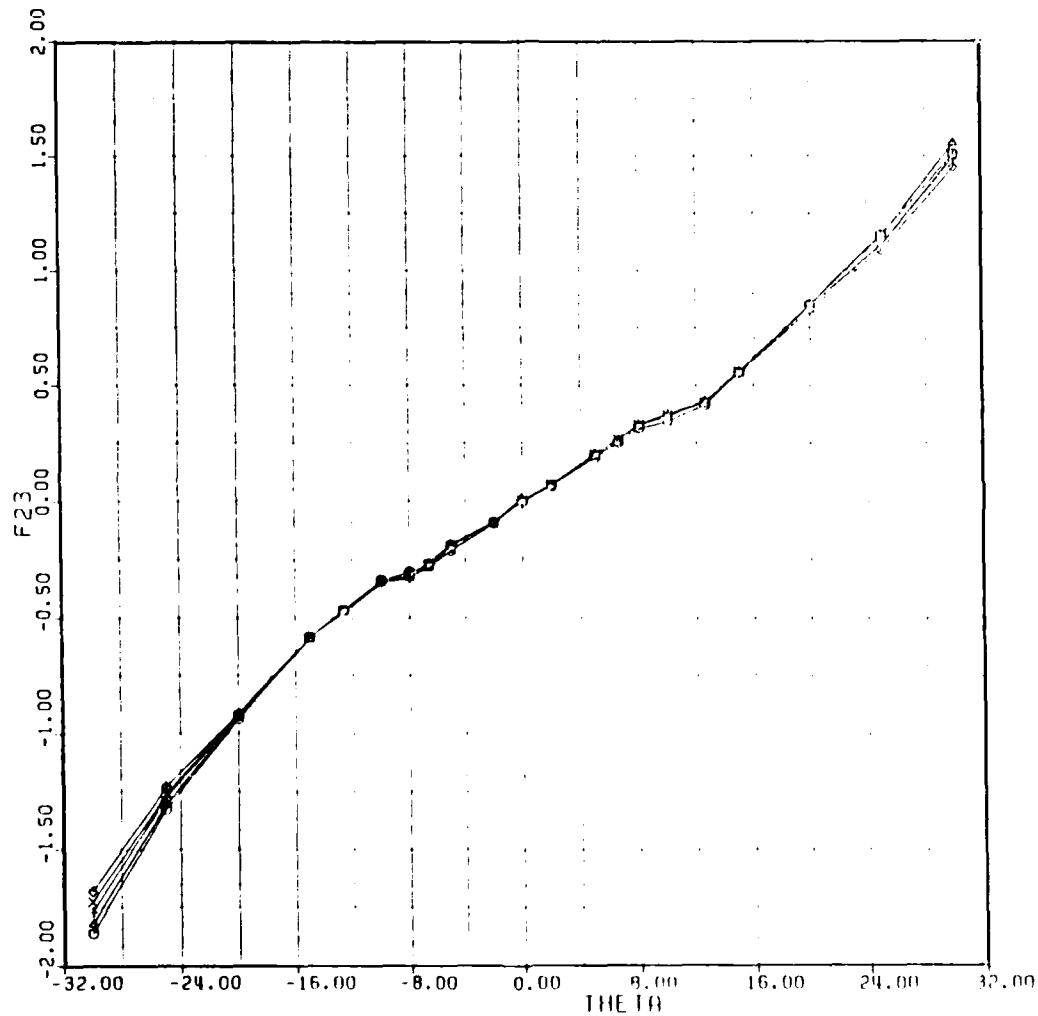
Figure 2-11A: Angle Probe Coefficent Prediction.
              F23 Versus Phi with Mach Number = 0.6

4-WAY PROBE CALIBRATION -- VS. MACH NO.

⊙ MACH NO. = 0.35   PHI = 0.000
▲ MACH NO. = 0.50   PHI = 0.000
+ MACH NO. = 0.60   PHI = 0.000
× MACH NO. = 0.85   PHI = 0.000
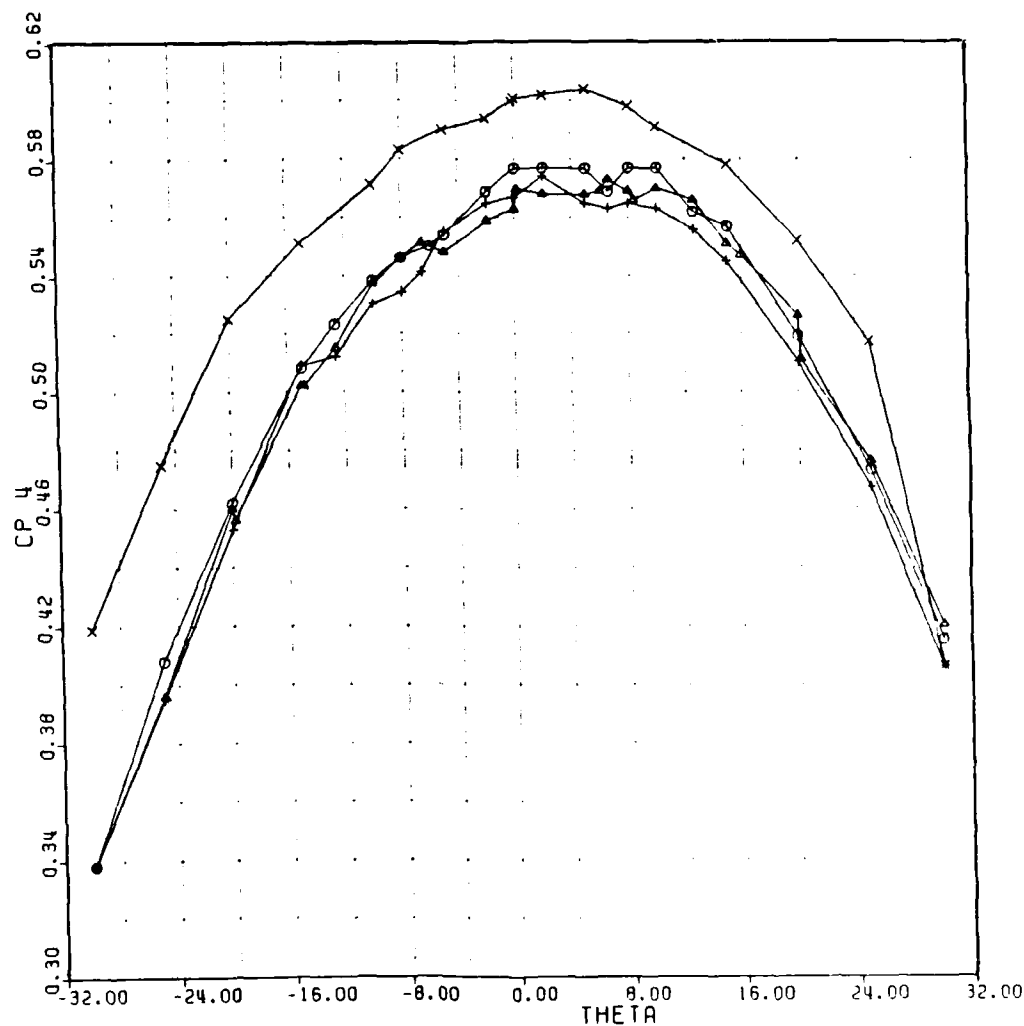
Figure 2-10E: Angle Probe Coefficent Prediction.
                CP4 Versus Mach Number with Phi = 0.0
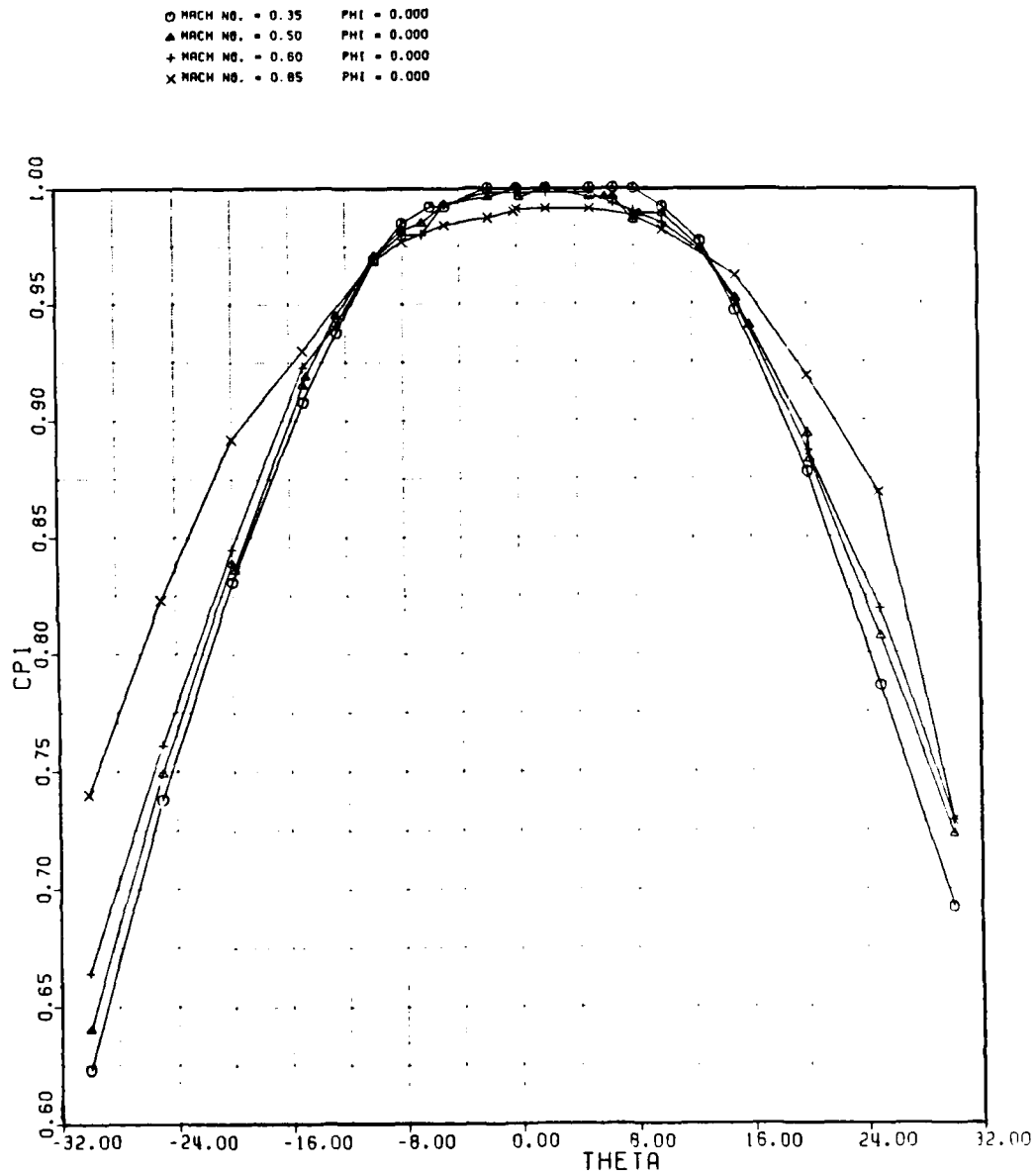
4-WAY PROBE CALIBRATION -- VS. MACH NO.

○ MACH NO. = 0.35   PHI = 0.000
▲ MACH NO. = 0.50   PHI = 0.000
+ MACH NO. = 0.60   PHI = 0.000
✕ MACH NO. = 0.85   PHI = 0.000

Figure 2-18D: Angle Probe Coefficent Prediction,
CP1 Versus Mach Number with Phi = 0.0

4-WAY PROBE CALIBRATION -- VS. MACH NO.

⊙ MACH NO. = 0.35   PHI = 0.000
▲ MACH NO. = 0.50   PHI = 0.000
+ MACH NO. = 0.60   PHI = 0.000
✕ MACH NO. = 0.85   PHI = 0.000
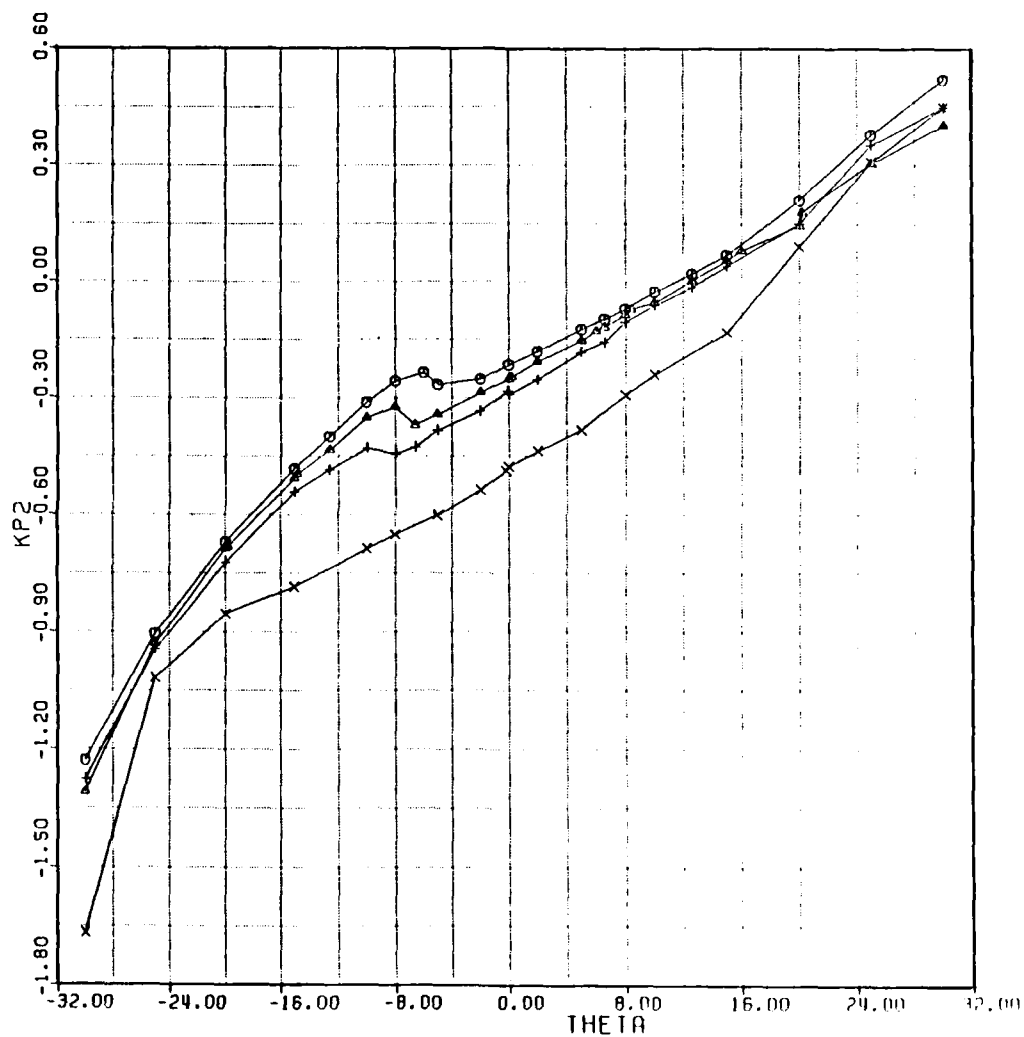
Figure 2-18C: Angle Probe Coefficent Prediction.
                KP2 Versus Mach Number with Phi = 0.0

4-WAY PROBE CALIBRATION -- VS. MACH NO.

⊙ MACH NO. = 0.35   PHI = 0.000
▲ MACH NO. = 0.50   PHI = 0.000
+ MACH NO. = 0.60   PHI = 0.000
✕ MACH NO. = 0.85   PHI = 0.000
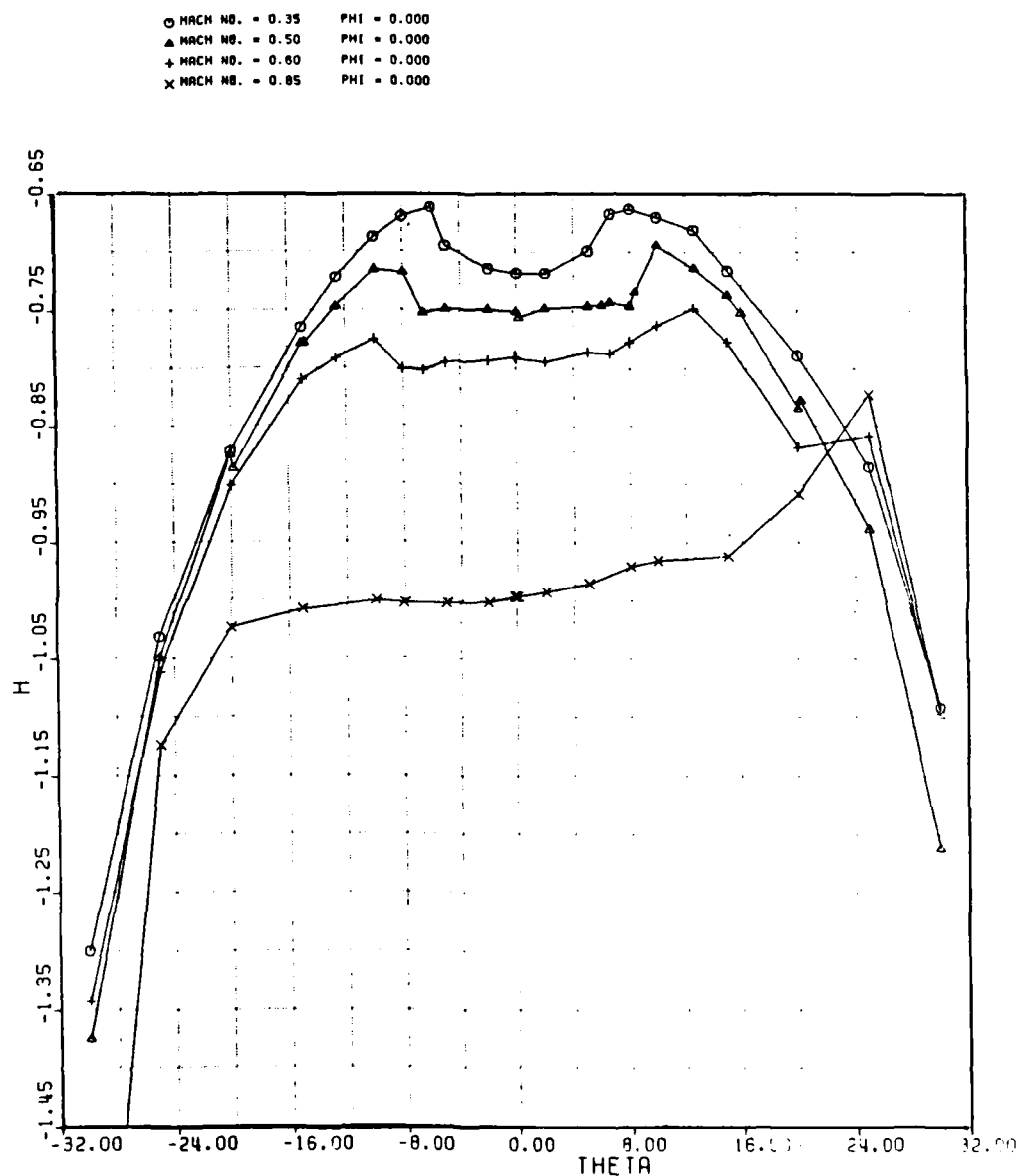
Figure 2-10B: Angle Probe Coefficent Prediction.
H23 Versus Mach Number with Phi = 0.0

4-WAY PROBE CALIBRATION -- VS. MACH NO.

⊙ MACH NO. = 0.35   PHI = 0.000
▲ MACH NO. = 0.50   PHI = 0.000
+ MACH NO. = 0.60   PHI = 0.000
✕ MACH NO. = 0.85   PHI = 0.000
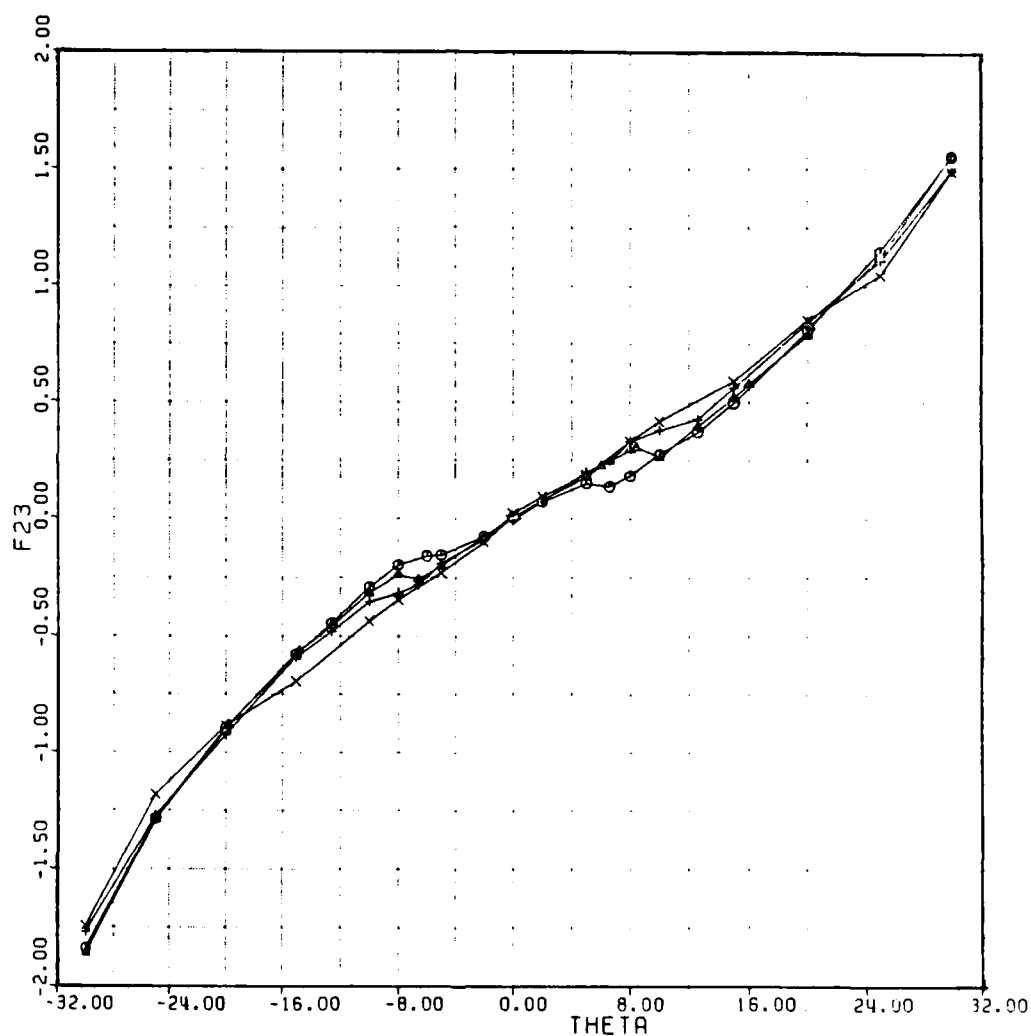
Figure 2-10A: Angle Probe Coefficent Prediction,
                F23 Versus Mach Number with Phi = 0.0

ANGLE PROBE COEFFICIENT PREDICTION

ELLIPSE RATIO [A/B] = 1.350   PHI = 0.0
MACH NUMBER   = 0.600
CALIBRATION DATA   = ▥
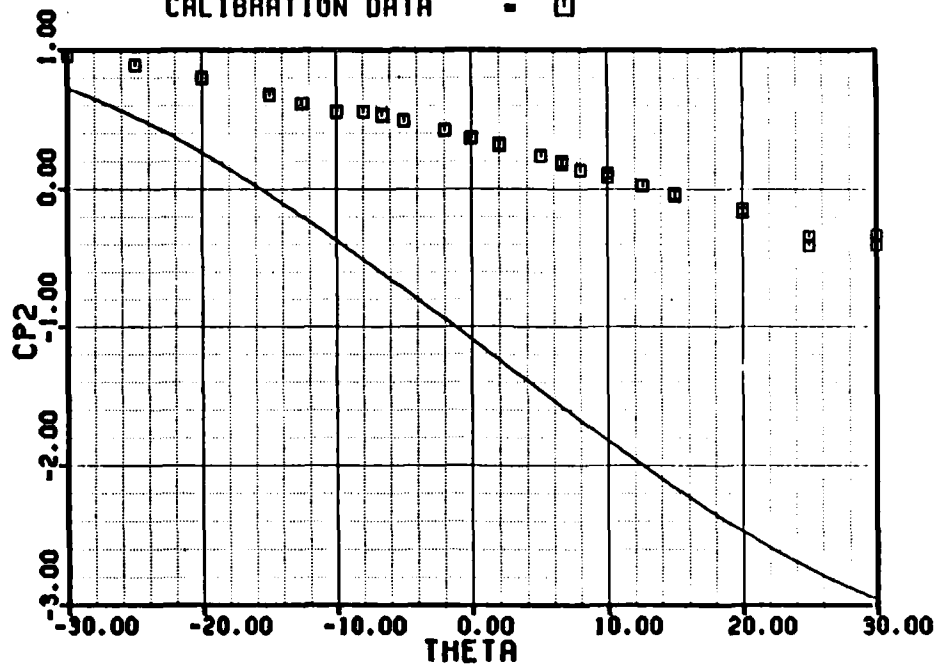
Figure 2-9E: Angle Probe Coefficent Prediction,
               CP2 Versus Theta
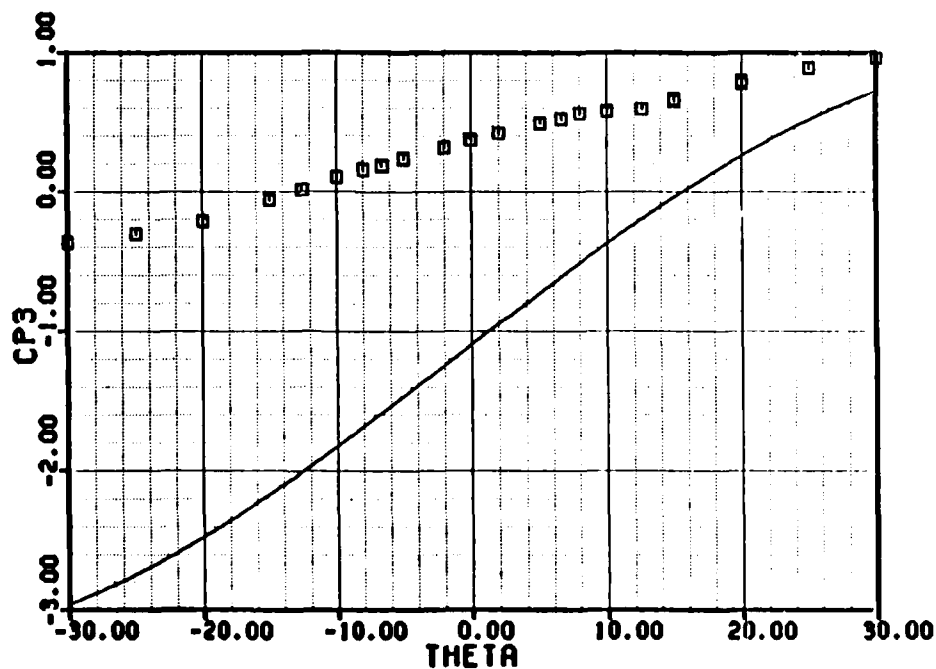
Figure 2-9F: Angle Probe Coefficent Prediction,
               CP3 Versus Theta

ANGLE PROBE COEFFICIENT PREDICTION

ELLIPSE RATIO [A/B] = 1.350   PHI = 0.0

MACH NUMBER   = 0.600
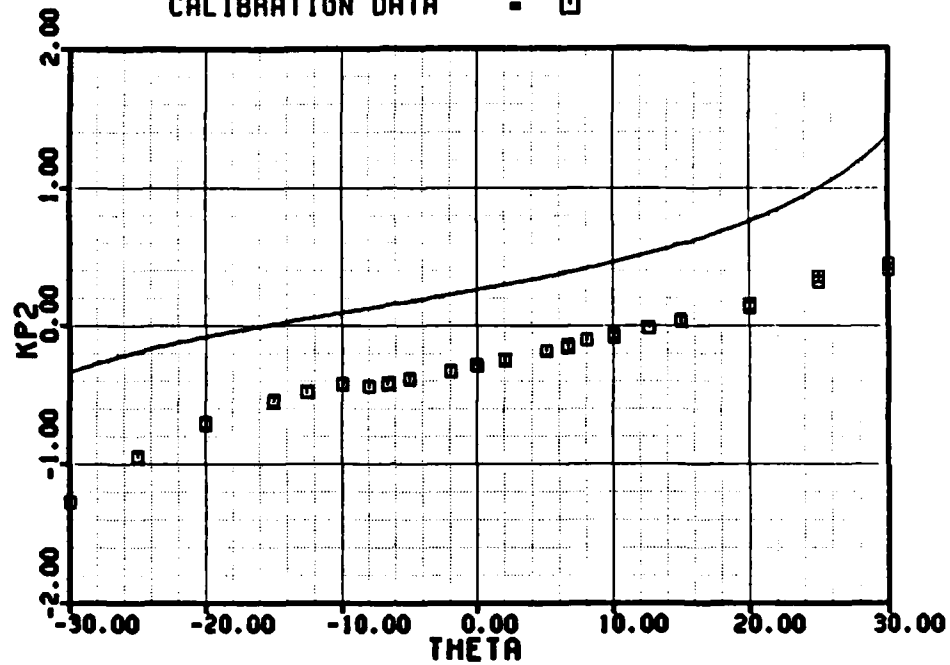
CALIBRATION DATA   = ▯

Figure 2-9C: Angle Probe Coefficent Prediction,
KP2 Versus Theta
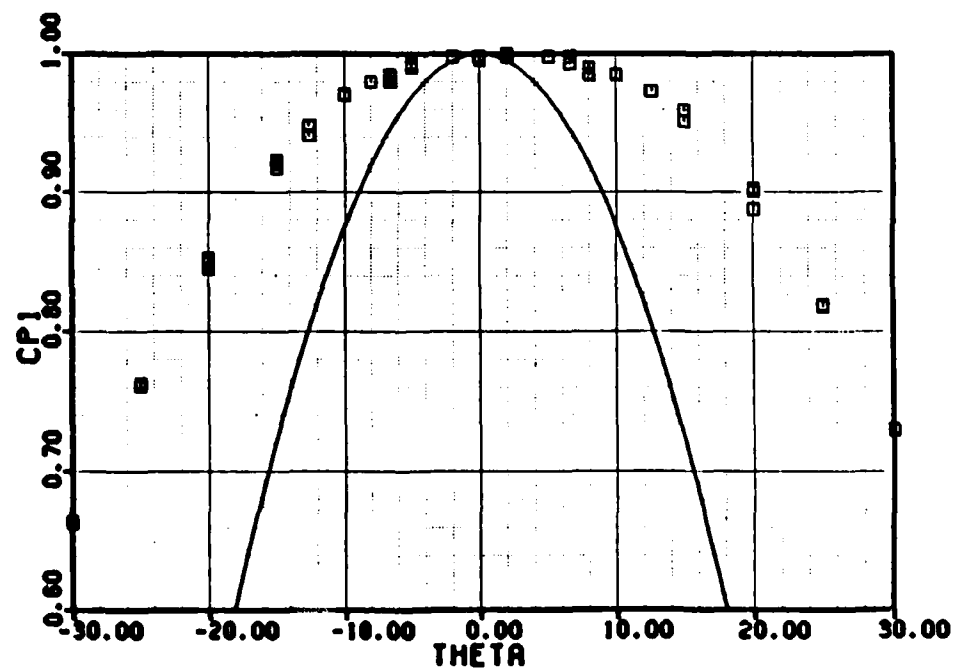
Figure 2-9D: Angle Probe Coefficent Prediction,
CP1 Versus Theta

ANGLE PROBE COEFFICIENT PREDICTION

ELLIPSE RATIO [A/B] = 1.350   PHI = 0.0
MACH NUMBER   = 0.600
CALIBRATION DATA   = □
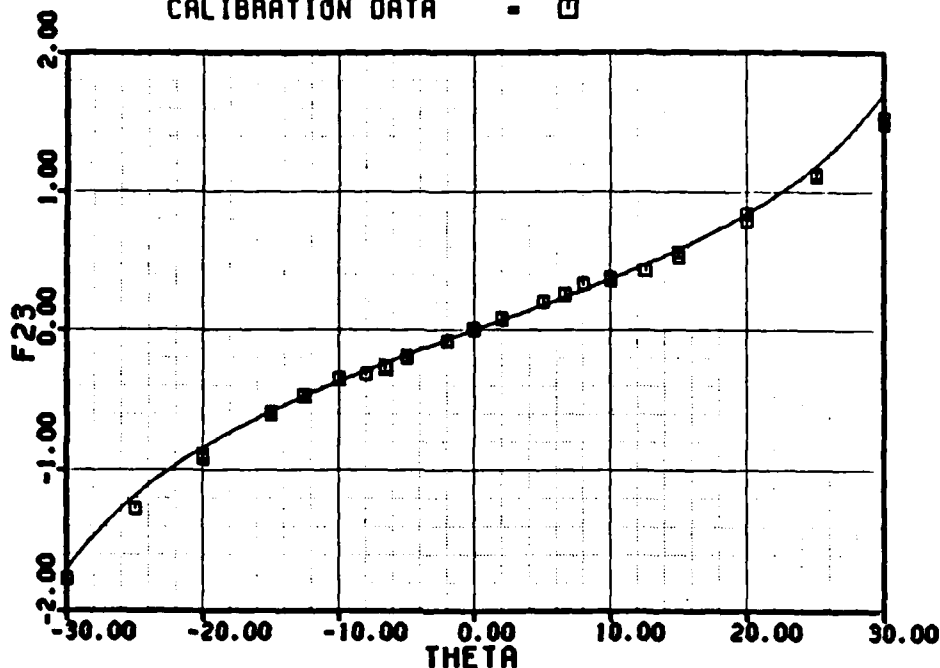
Figure 2-9A: Angle Probe Coefficent Prediction,
              F23 Versus Theta
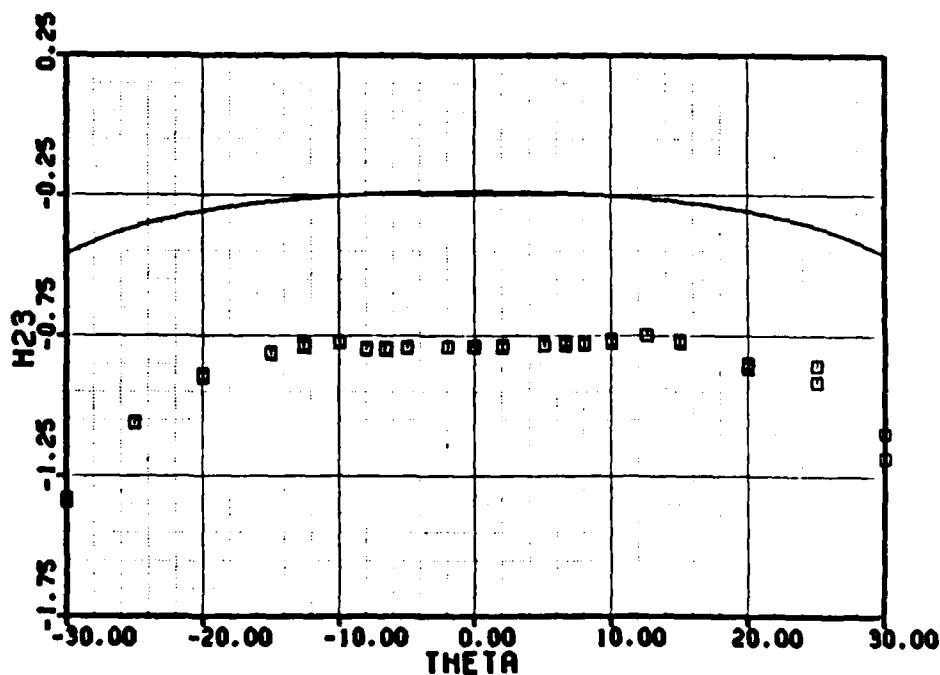
Figure 2-9B: Angle Probe Coefficent Prediction,
              H23 Versus Theta
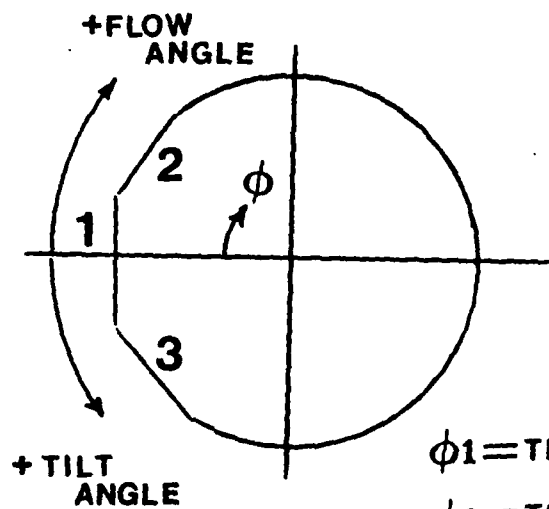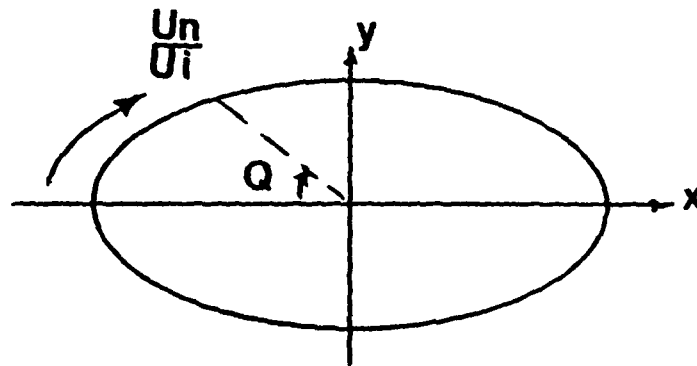
Figure 2-8: Definitions for Ellipse Flowfield Prediction

3.3 mm

45°

4

KULITE
TRANSDUCERS

2   3

Cooling Water
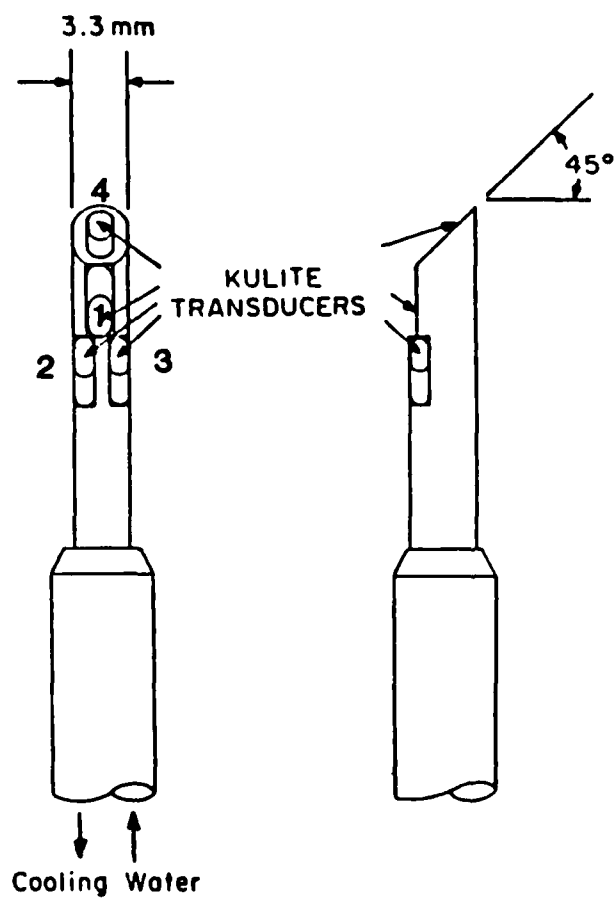
Figure 2-7:   Schematic of "Four-Way" Angle Probe

4-WAY PROBE CALIBRATION -- M=0.60

⊙ MACH NO. = 0.60   PHI = -10.000
▲ MACH NO. = 0.60   PHI = -5.000
+ MACH NO. = 0.60   PHI = 0.000
× MACH NO. = 0.60   PHI = 5.000
◆ MACH NO. = 0.60   PHI = 10.000
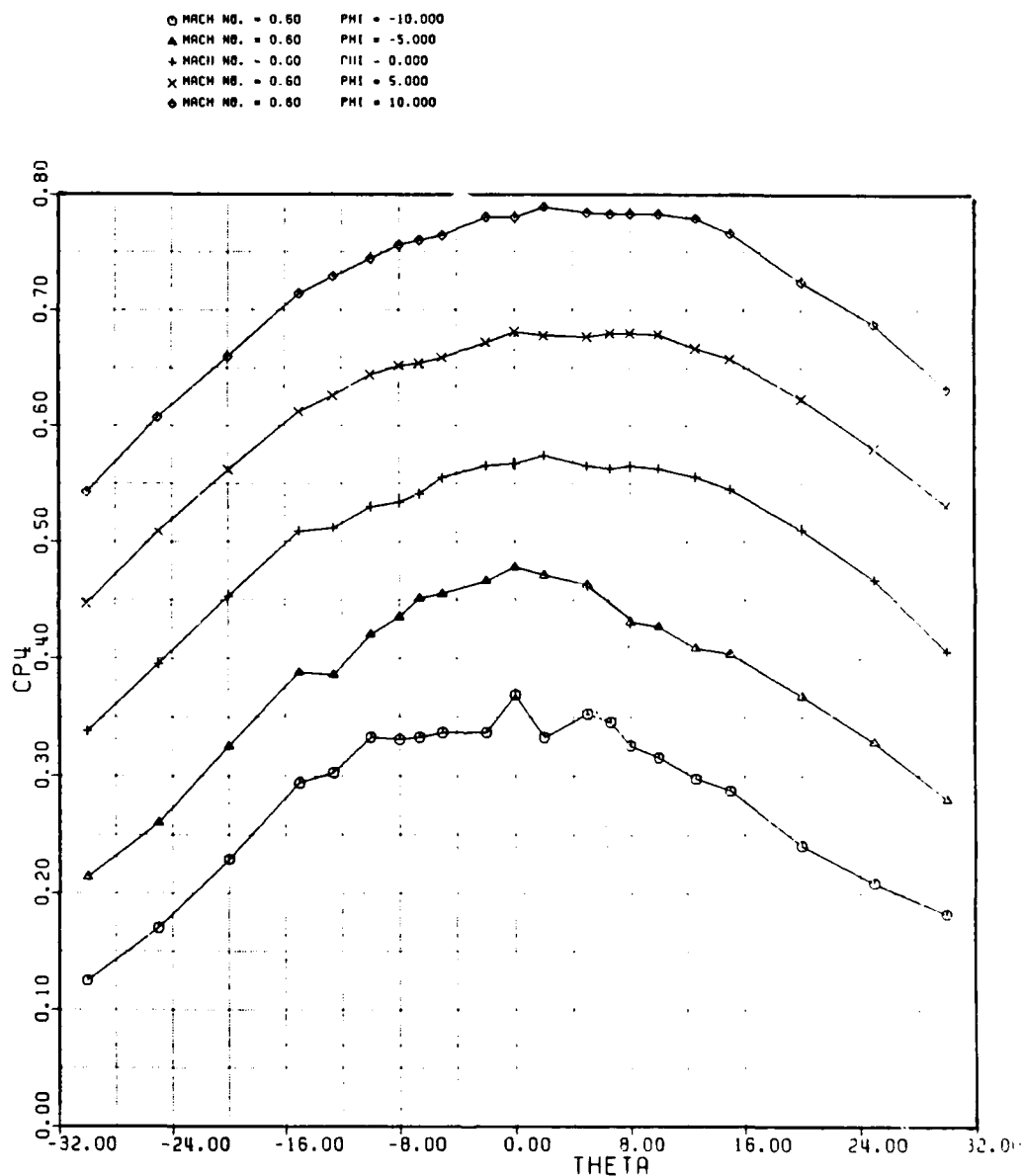
Figure 2-11E: Angle Probe Coefficent Prediction,
                CP4 Versus Phi with Mach Number = 0.6
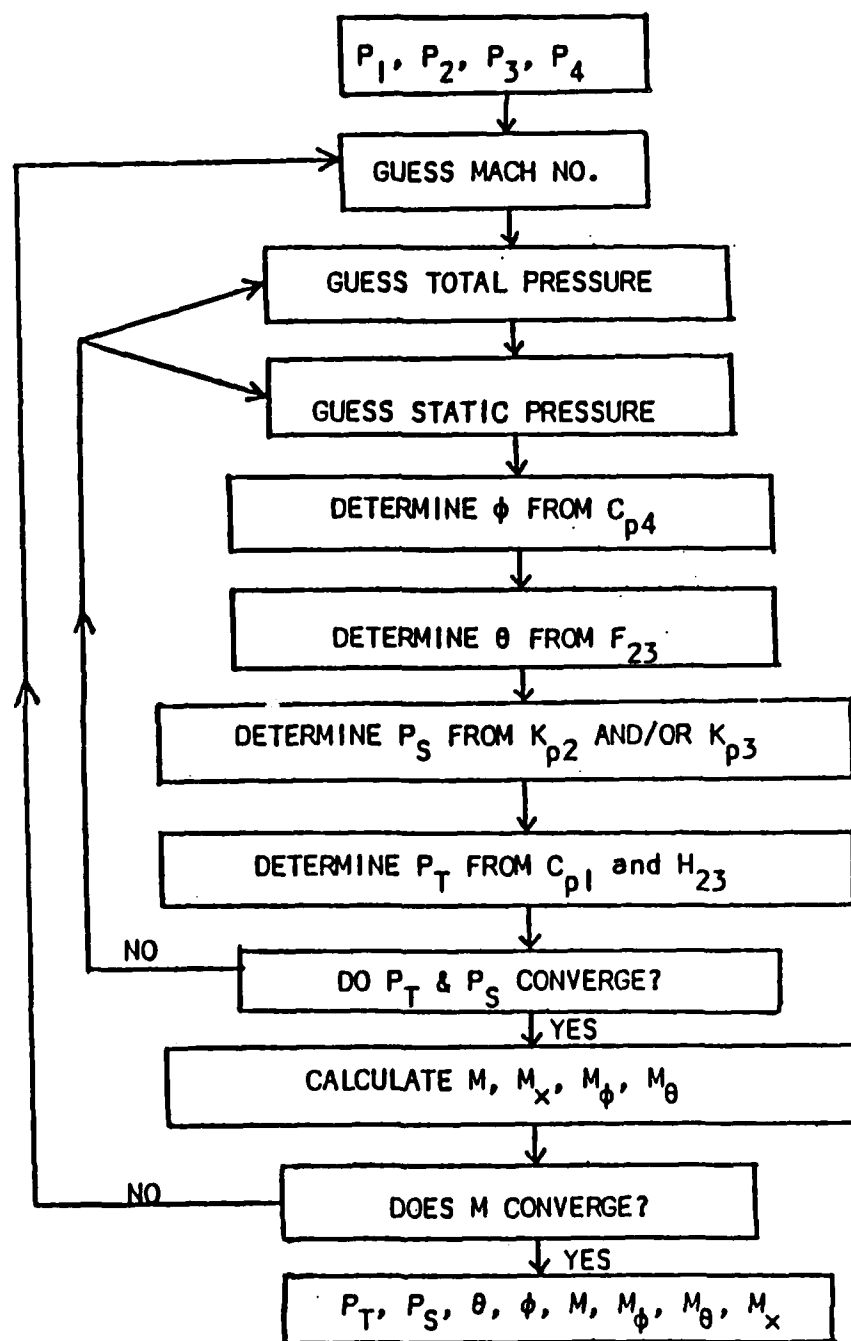
Figure 2-12: Flowchart of Angle Probe Data Reduction
Scheme (from [10])
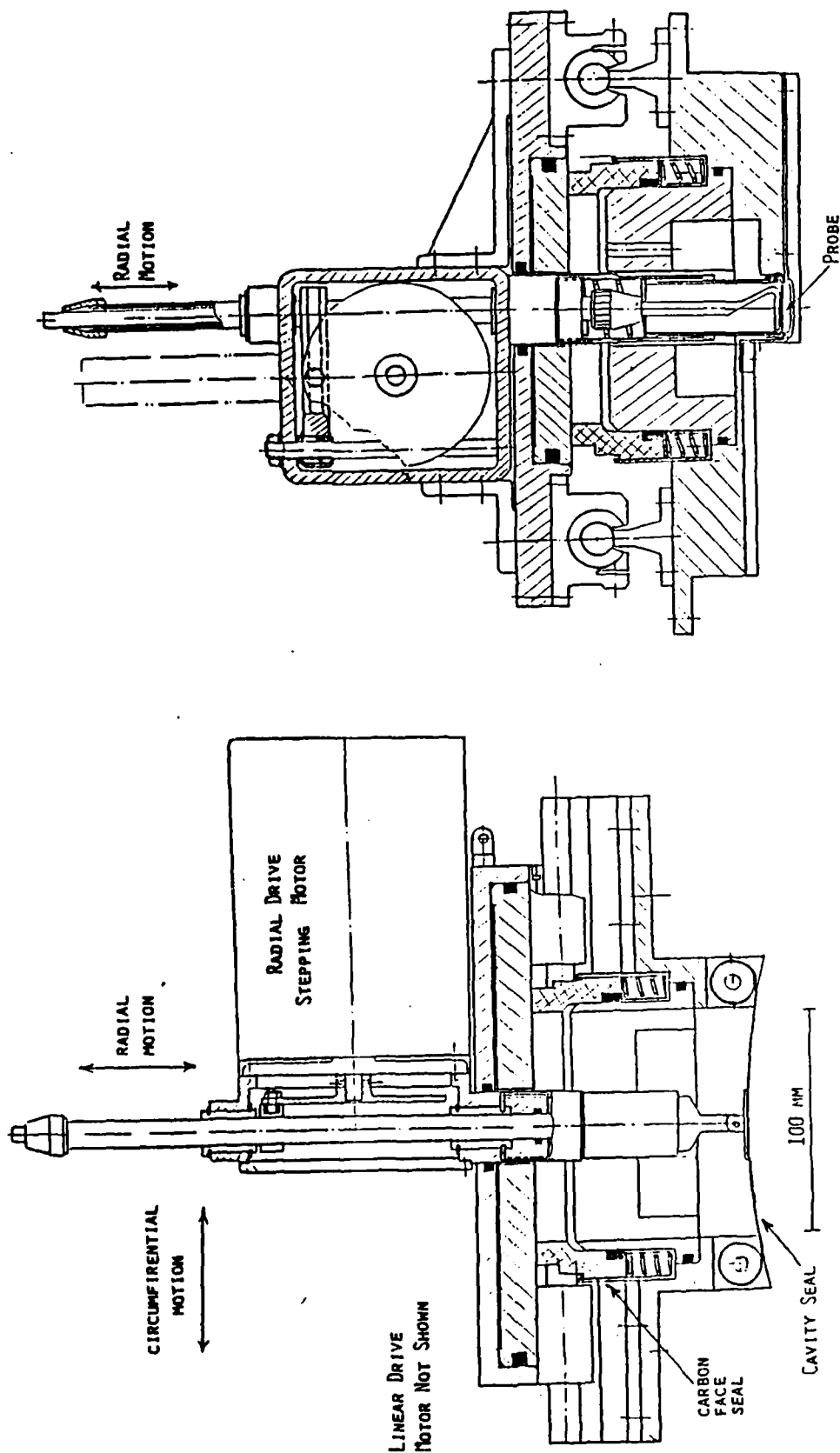
Figure 2-13: Schematic of Stationary Frame, Radial/Circumfer-
ential Translator: A) Downstream View, B) Side view

SHOCK TUBE CONDITIONS -- AIR

GAMMA	=	1.40
GAS CONSTANT [J/KG K]	=	287.18
TEMPERATURE [K]	=	303.00
DRIVEN GAS PRESSURE [KPA]	=	98.31
DIAPHRAGM PRESSURE RATIO	=	1.48
SHOCK PRESSURE RATIO	=	1.2128
SHOCK VELOCITY [M/S]	=	379.53
REFLECTED SHOCK VELOCITY [M/S]	=	340.49
GAS VELOCITY [M/S]	=	48.80
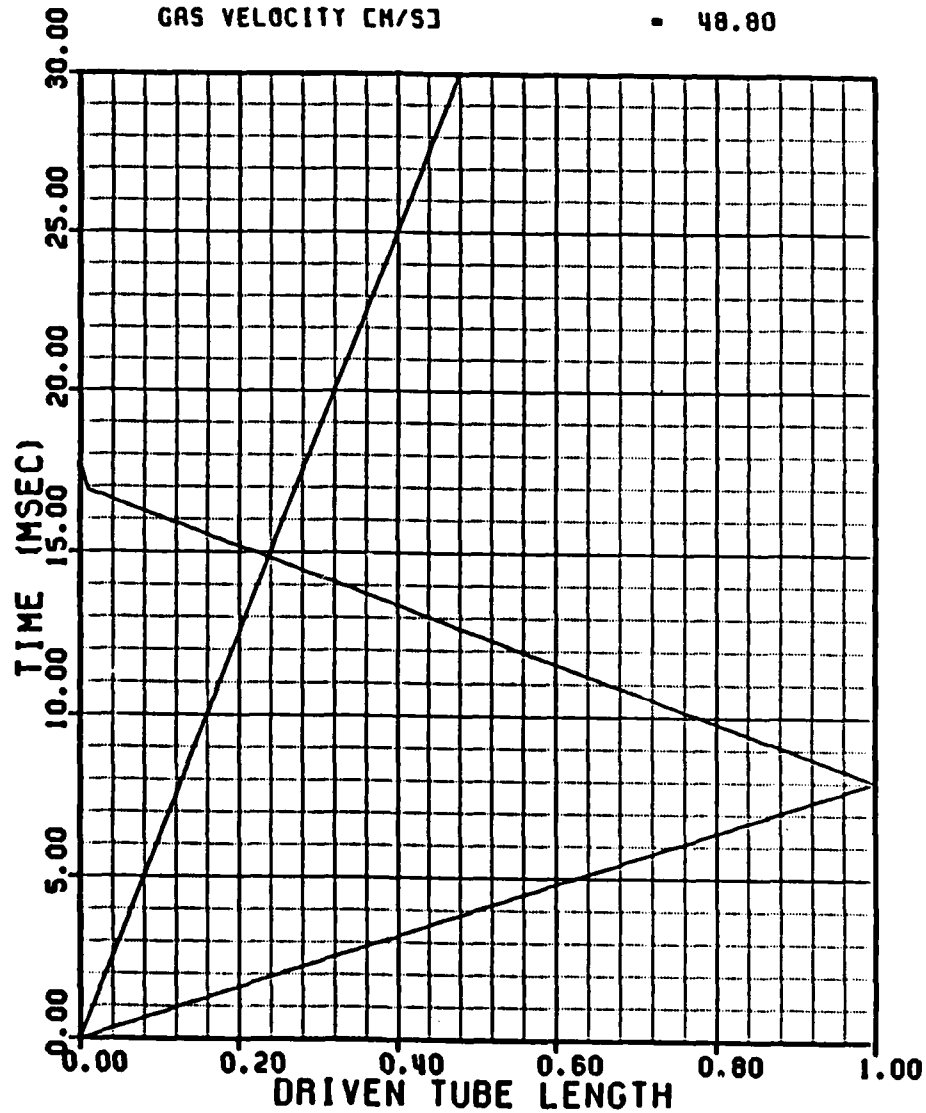
Figure 3-1: Shock Tube Wave Diagram
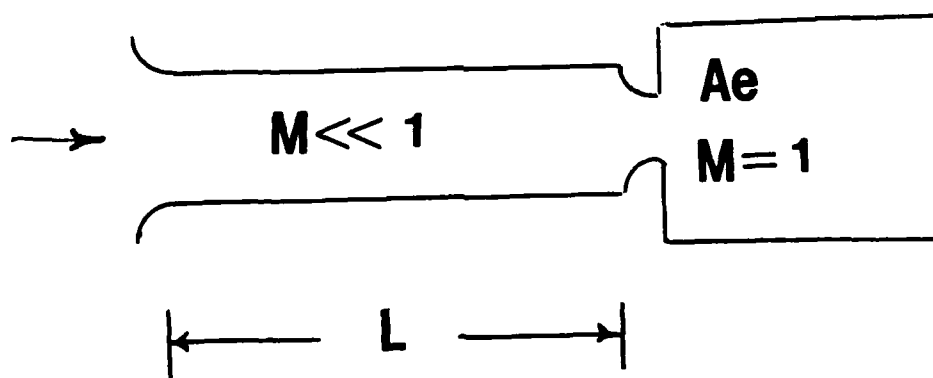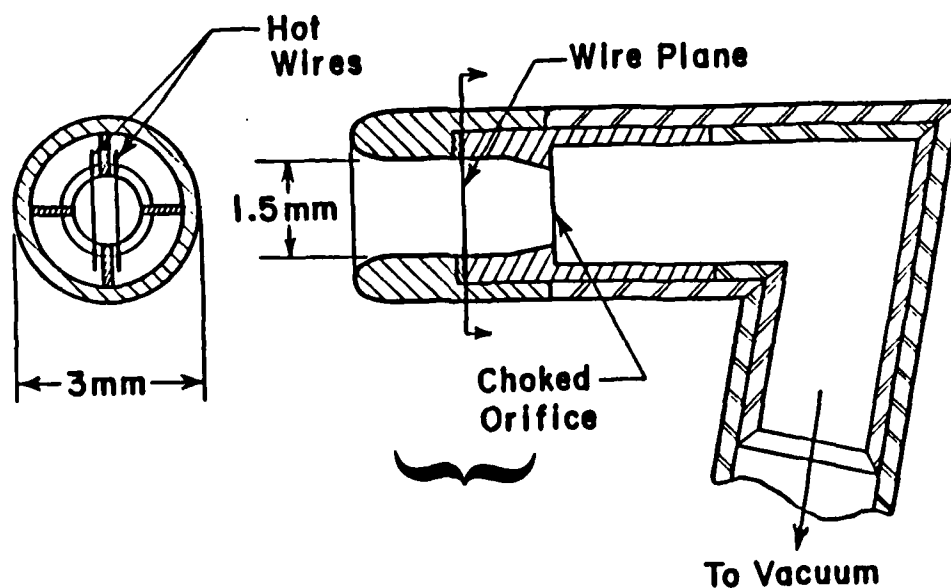
Figure 3-2: Aspirating Probe Model for Frequency Response Prediction
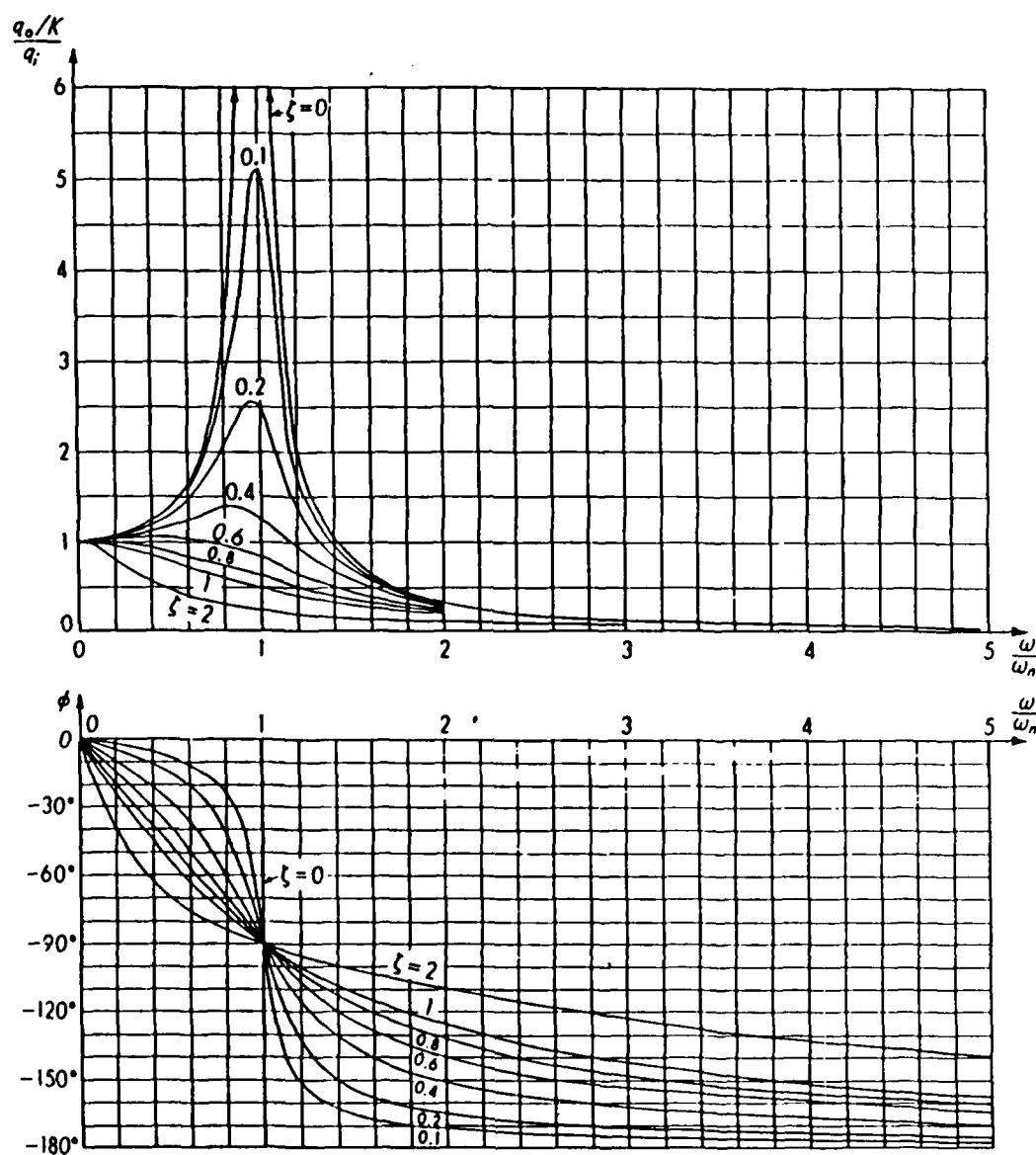
Figure 3-3: Nondimensionalized Frequency Response of
Second Order Instrument[FROM (25)]

ASPIRATING PROBE FREQUENCY RESPONSE
TEST   ST 19   IN AIR

OHM	= 2.00	PSI
P ATM	= 14.768	F
T ATM	= 76.0	PSIG
BURST PRESSURE	= 9.0	DEG
PROBE ANGLE	= 0.0	
DATA POINTS	= 512	
SAMPLE RATE	= 1024	KHZ

Figure 3-4A: Aspirating Probe Damped Natural
                Frequency in Air
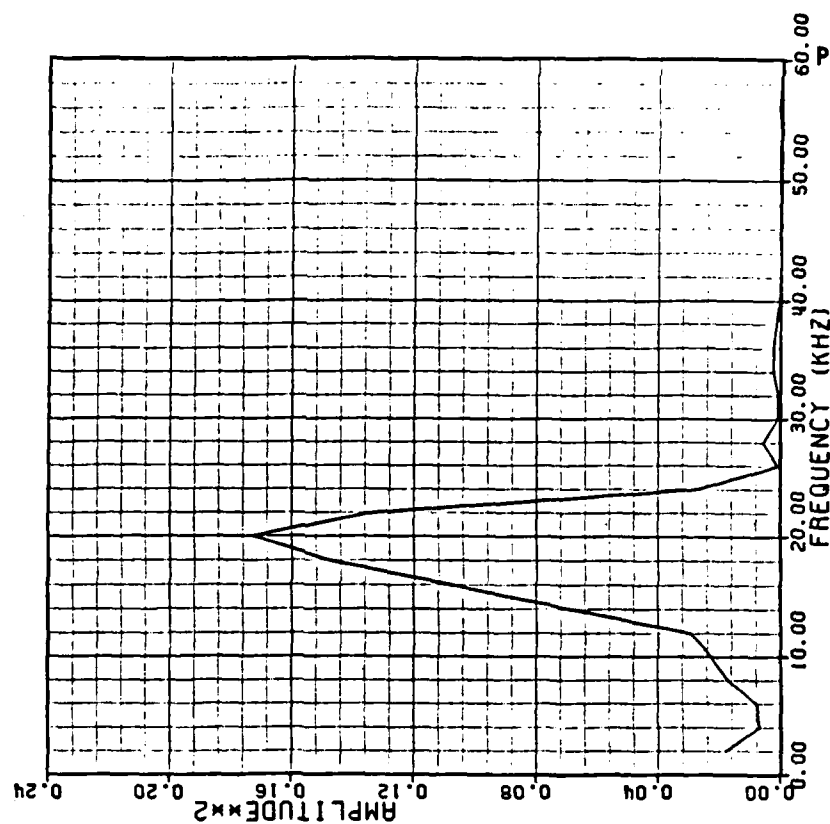
Figure 3-4B: FFT of Aspirating Probe Response
                to Step Input, Air

ASPIRATING PROBE FREQUENCY RESPONSE
TEST ST 24   IN FREON

OHA	=	1.80	
P ATM	=	14.820	PSI
T ATM	=	79.0	F
BURST PRESSURE	=	23.0	PSIG
PROBE ANGLE	=	0.0	DEG
DATA POINTS	=	512	
SAMPLE RATE	=	1024	KHZ
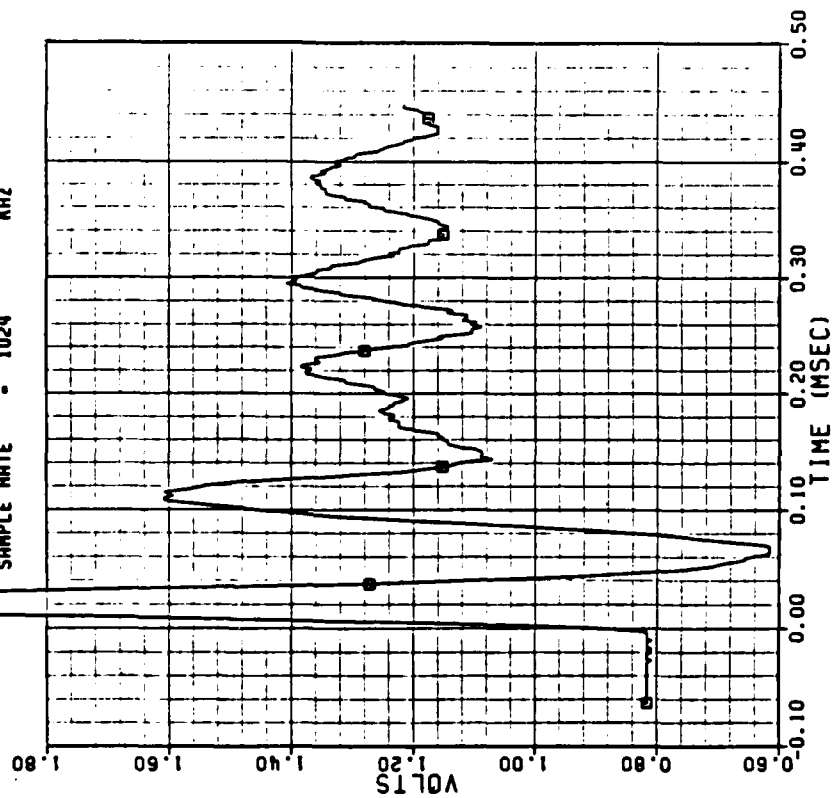
Figure 3-5A: Aspirating Probe Damped Natural
              Frequency in Freon-12
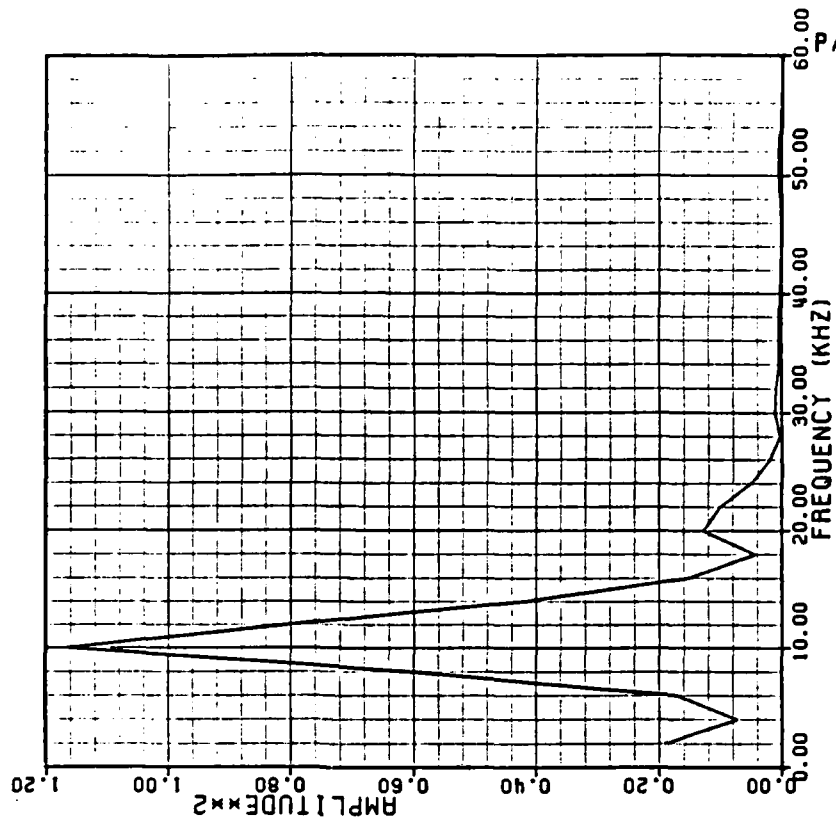
Figure 3-5B: FFT of Aspirating Probe Response
              to Step Input, Freon-12

PAGE 127
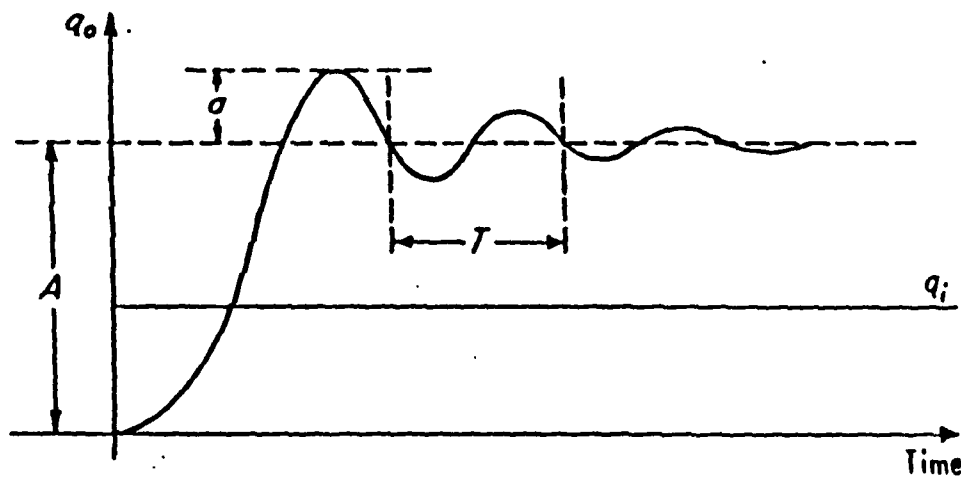
$$\zeta = \sqrt{\frac{1}{\left(\frac{\pi}{\log_e (a/A)}\right)^2 + 1}}$$

$$\omega_n = \frac{2\pi}{T' \sqrt{1 - \zeta^2}}$$

Figure 3-6:   Definitions for Calculation of Undamped
              Natural Frequency and Damping Ratio [3]
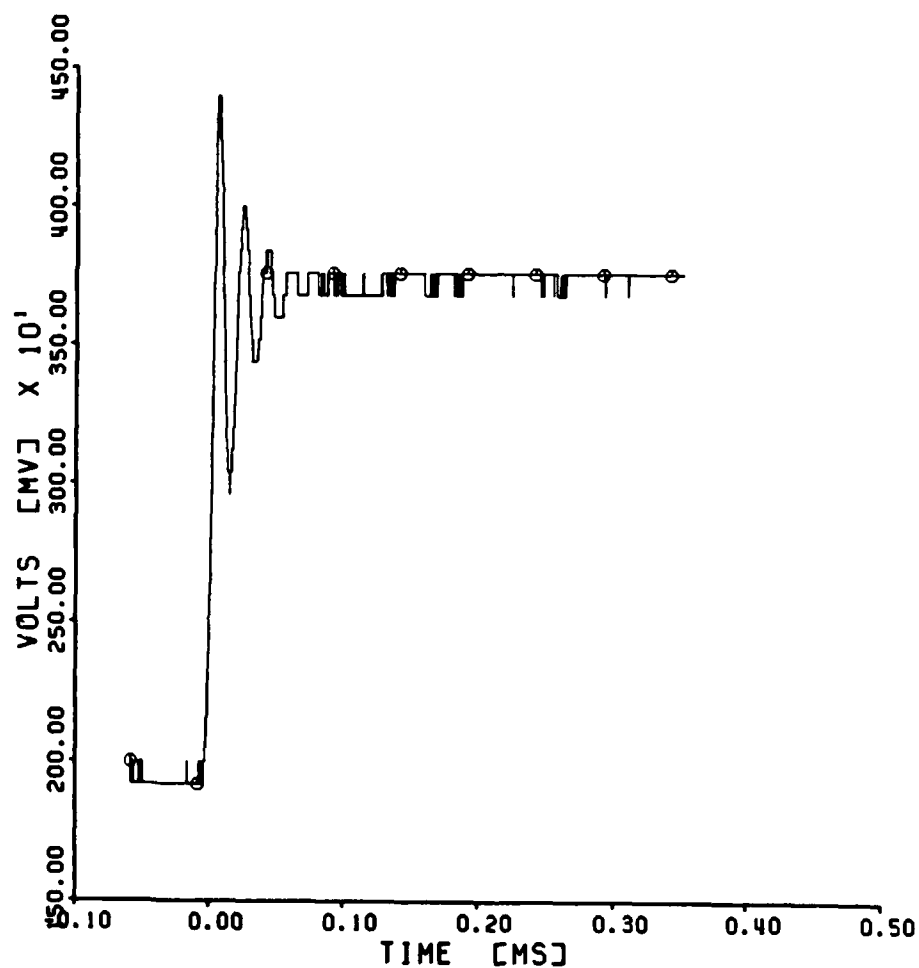
Figure 3-7:   Hot Wire Response to Step Change in
              Flowfield Velocity
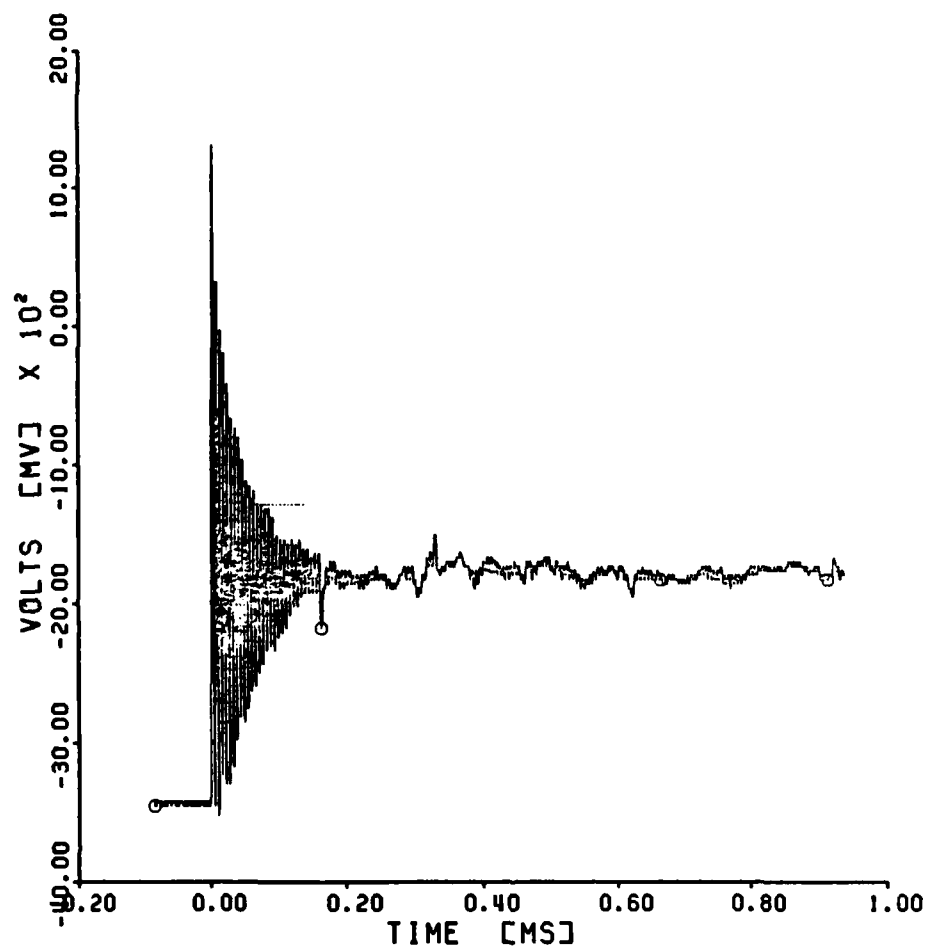
Figure 3-8:   Angle Probe Response to Step Change
              in Pressure

TRAVERSE PATH

0.5
AXIAL
CHORD

● PROBE CIRCUM. POS
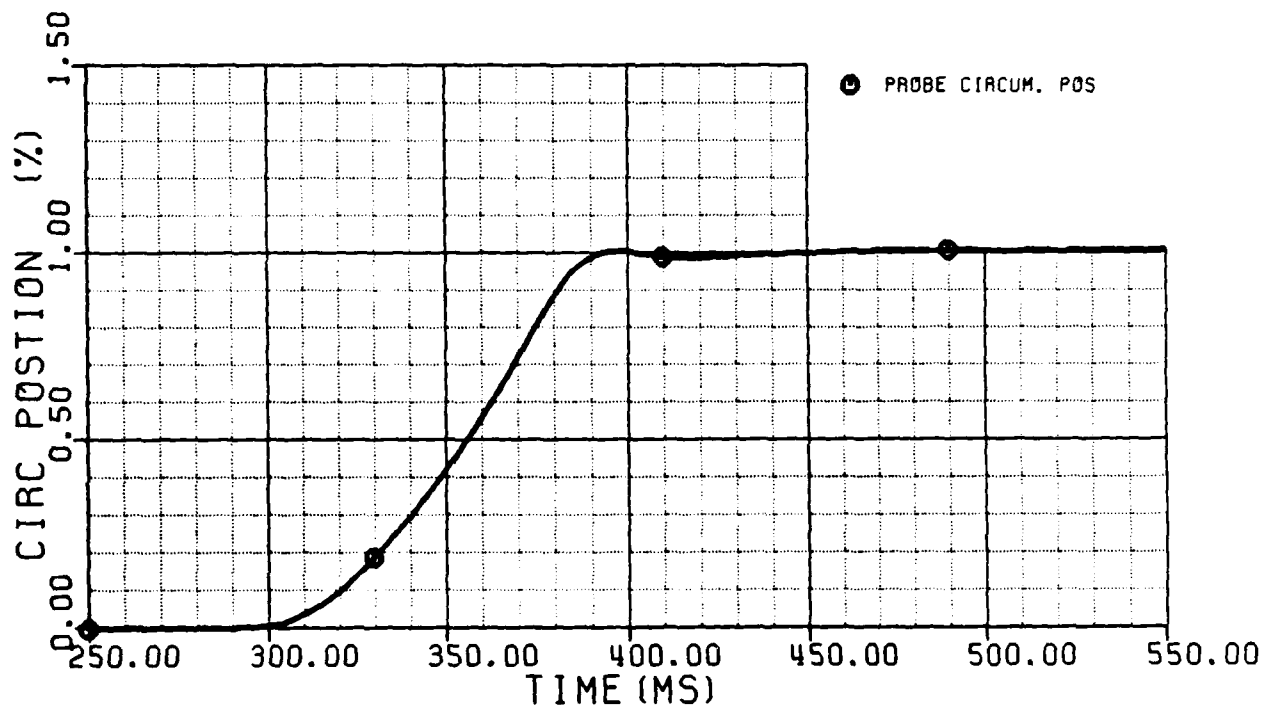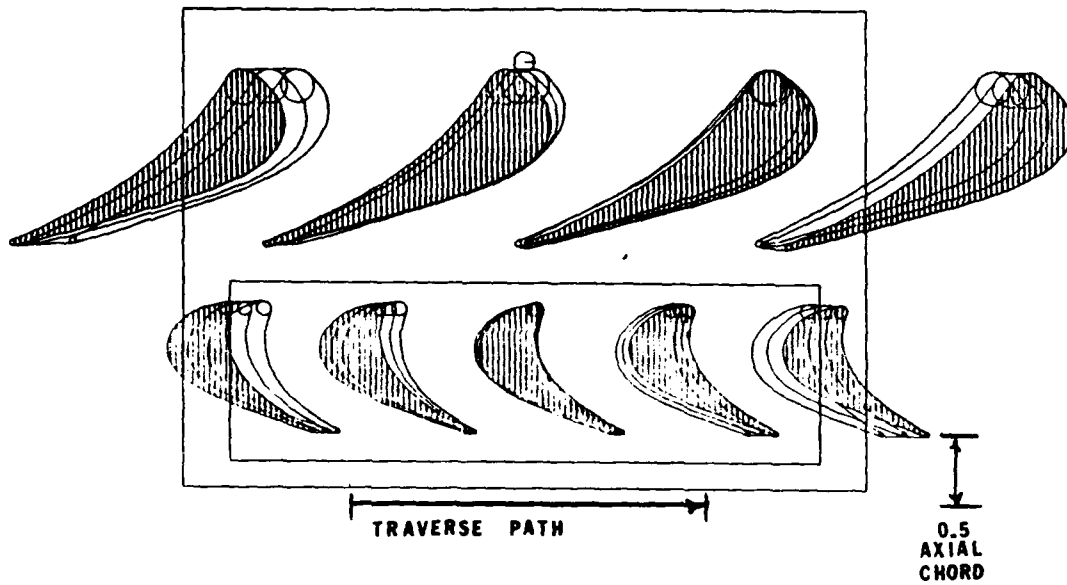
Figure 4-1:   Probe Traverse Location and Position Trace
Versus Test Time
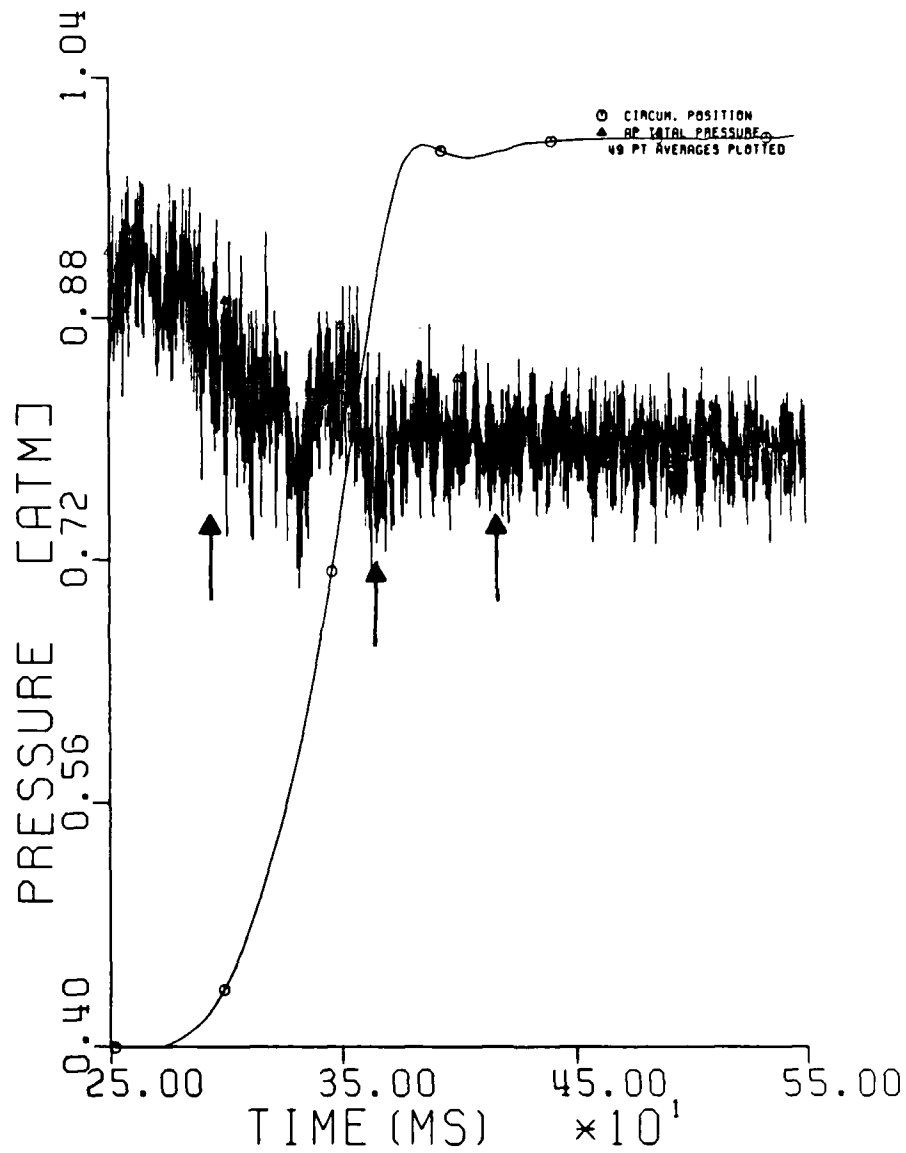
Figure 4-2:   Rotor Exit Total Pressure Trace with Data
               Analysis Times Noted
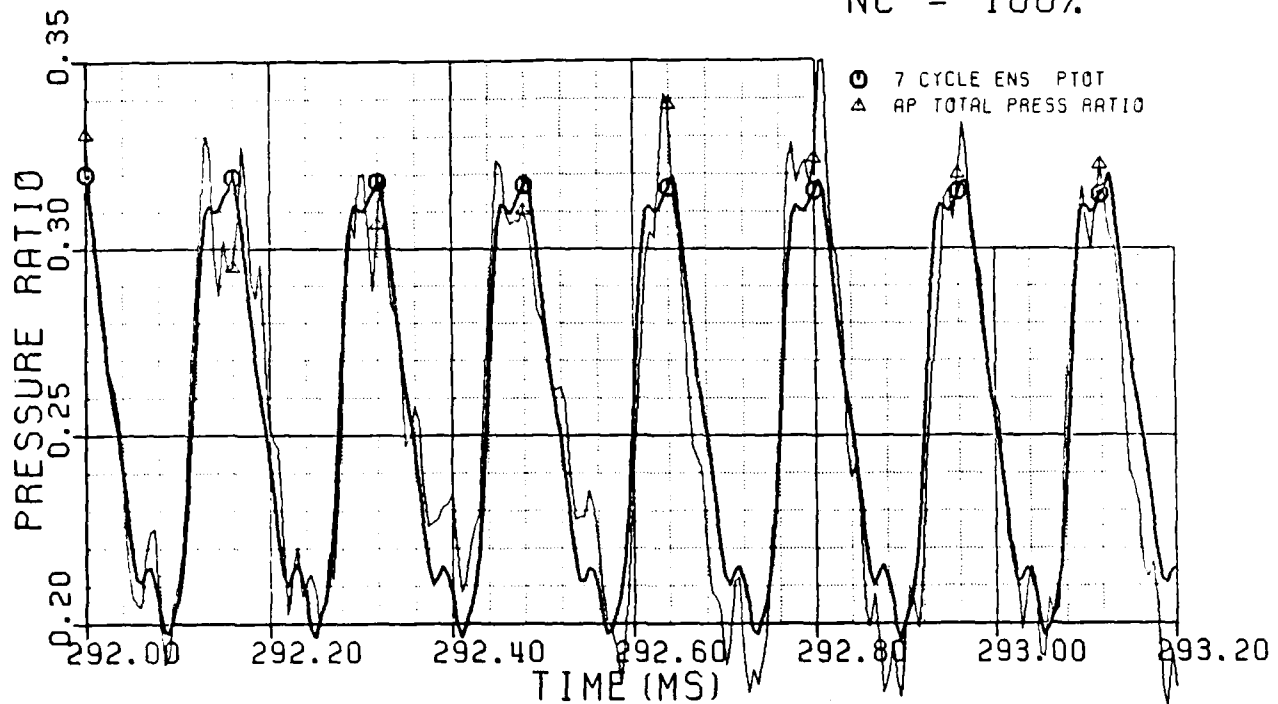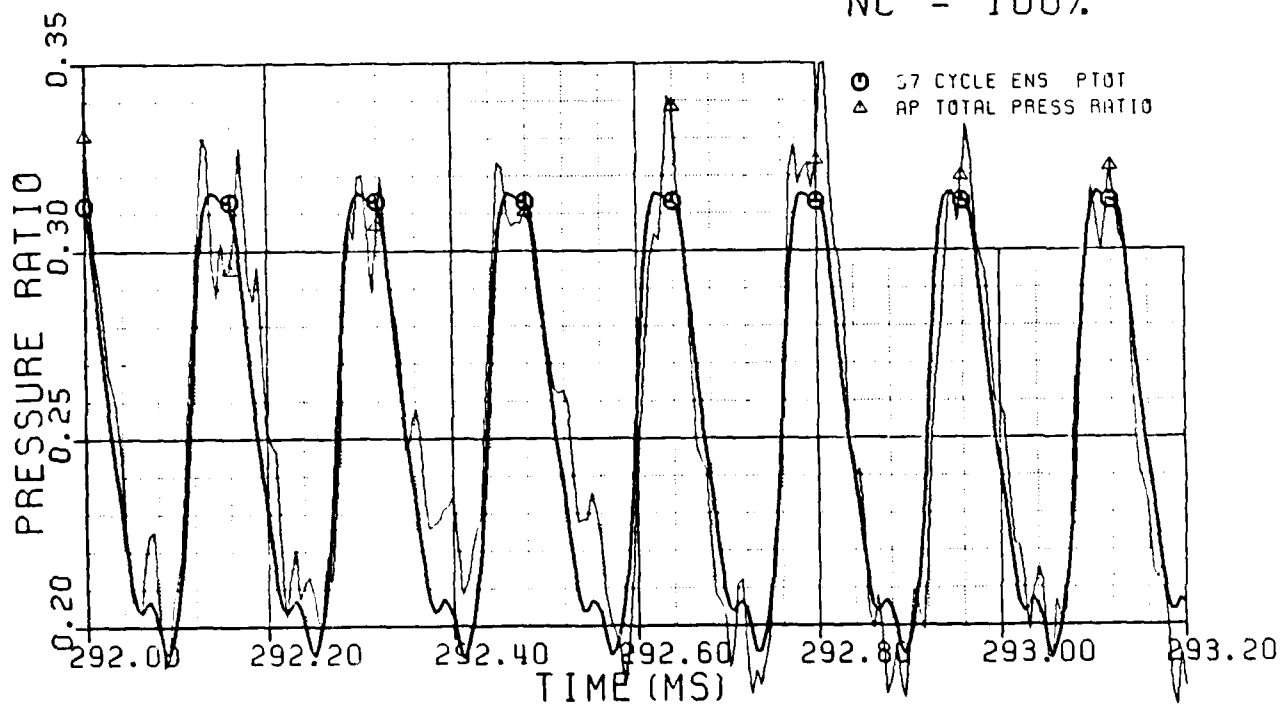
Figure 4-3A: Ensemble Average of Total Pressure Ratio with
7 and 37 Cycles: NC=100%, Time=292 msec

NC = 125%
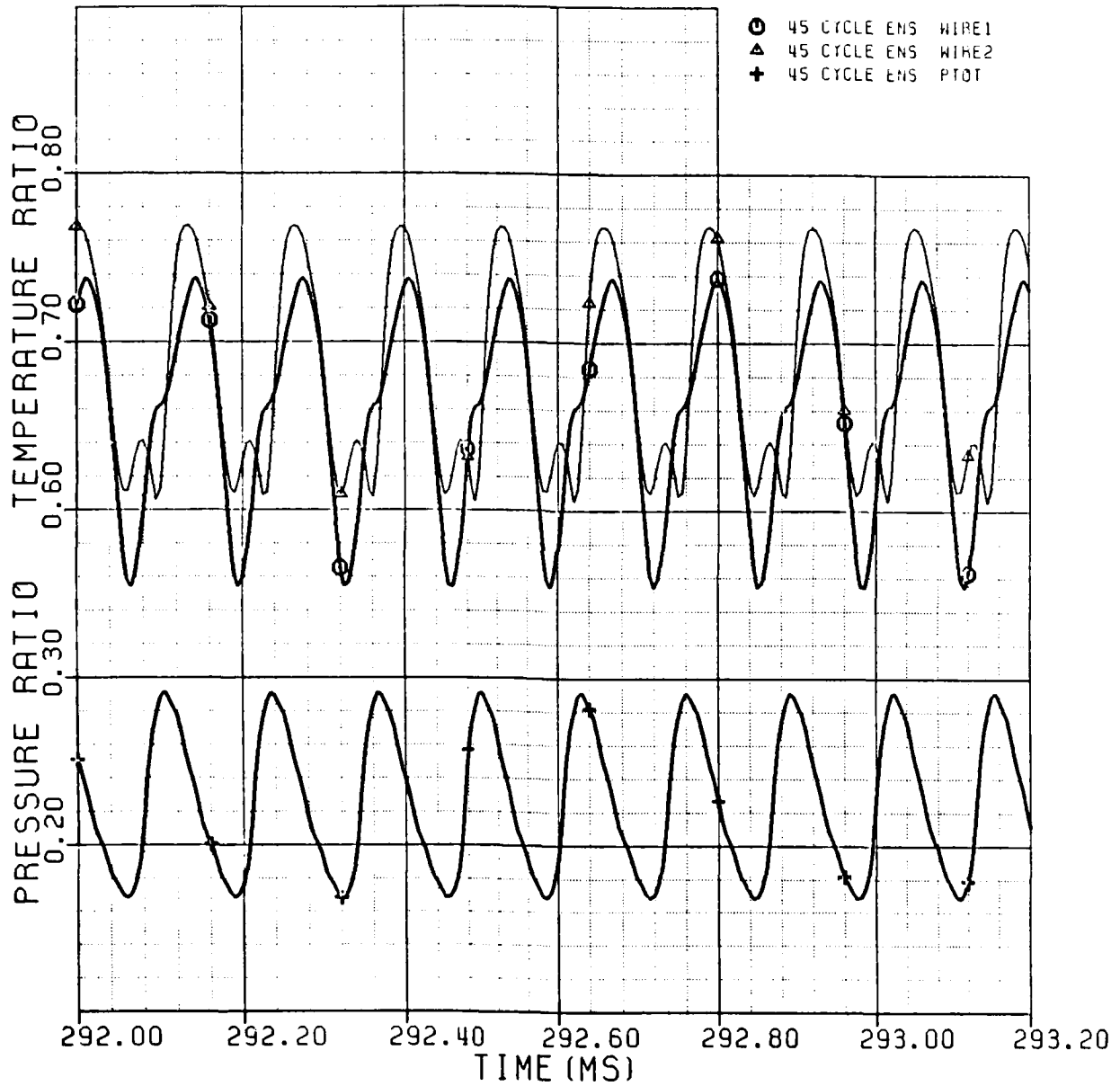
Figure 4-13: Total Temperature and Total Pressure Ratio
at Time=292 msec and NC=125%
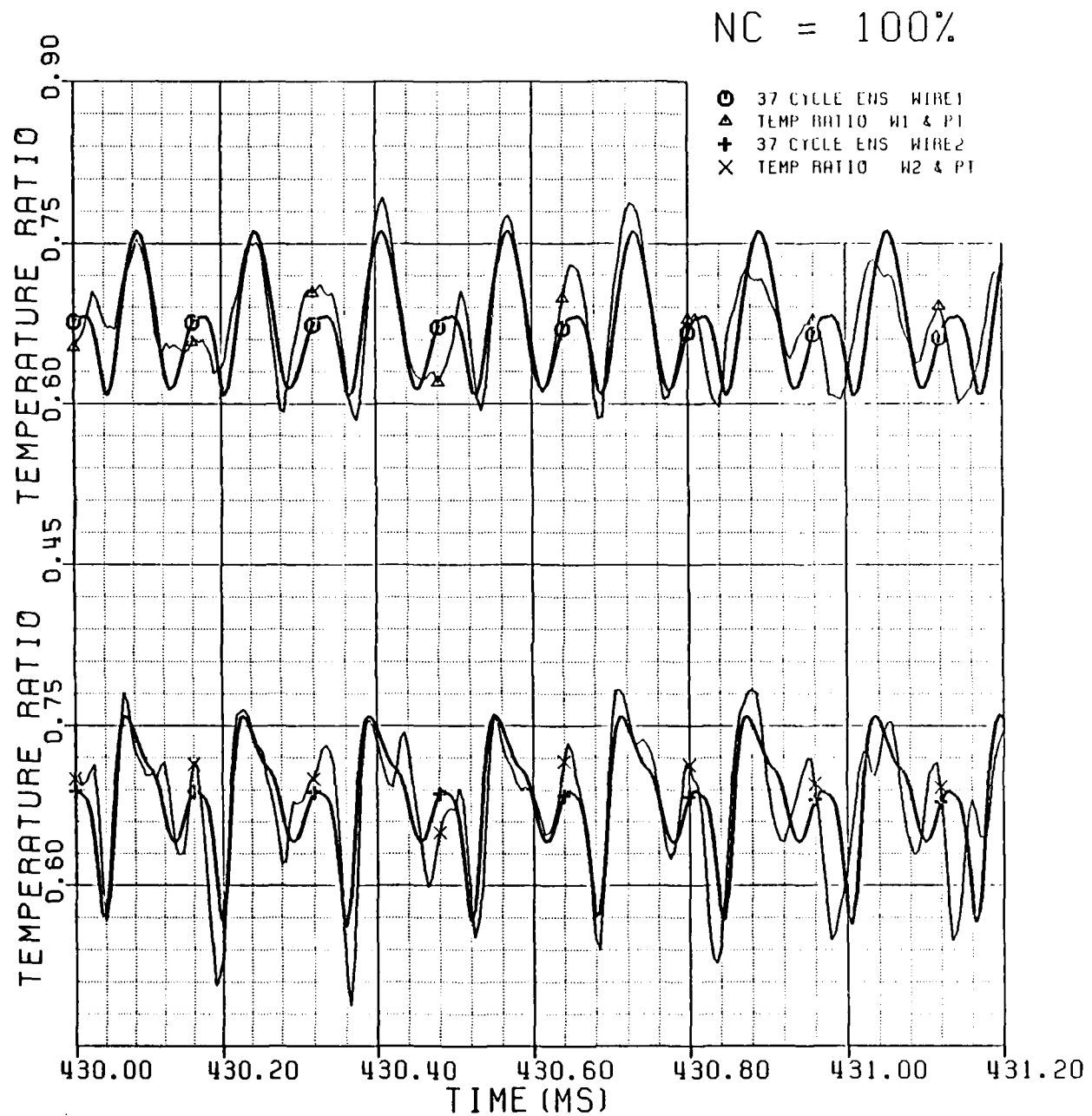
Figure 4-12: Ensembled and Instantaneous Total Temperature
Ratio at Time=430 msec and NC=100%
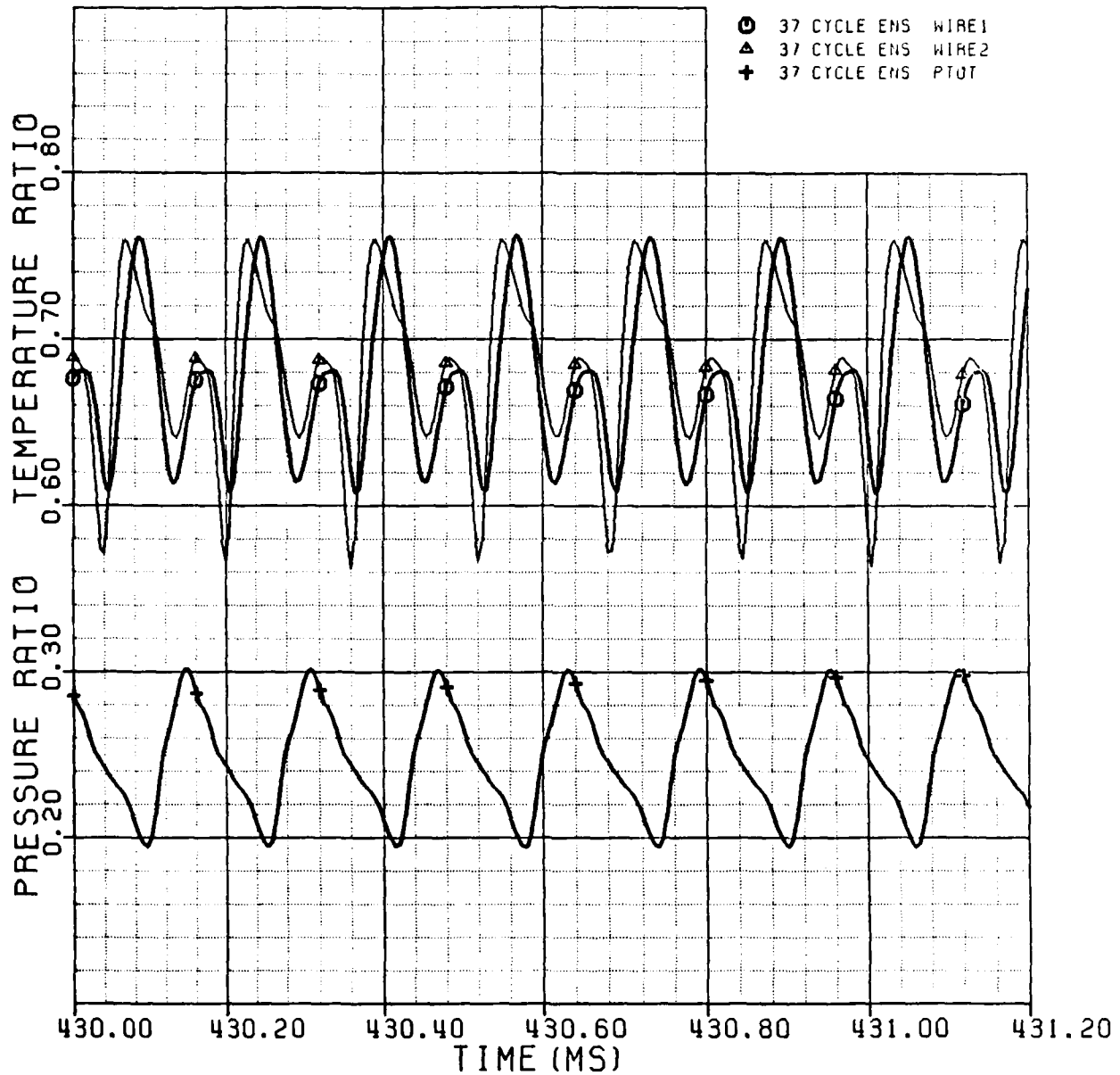
Figure 4-11:   Total Temperature and Total Pressure Ratio
at Time=430 msec and NC=100%

NC = 100%

● 37 CYCLE ENS WIRE1
▲ TEMP RATIO W1 & PT
+ 37 CYCLE ENS WIRE2
✕ TEMP RATIO W2 & PT
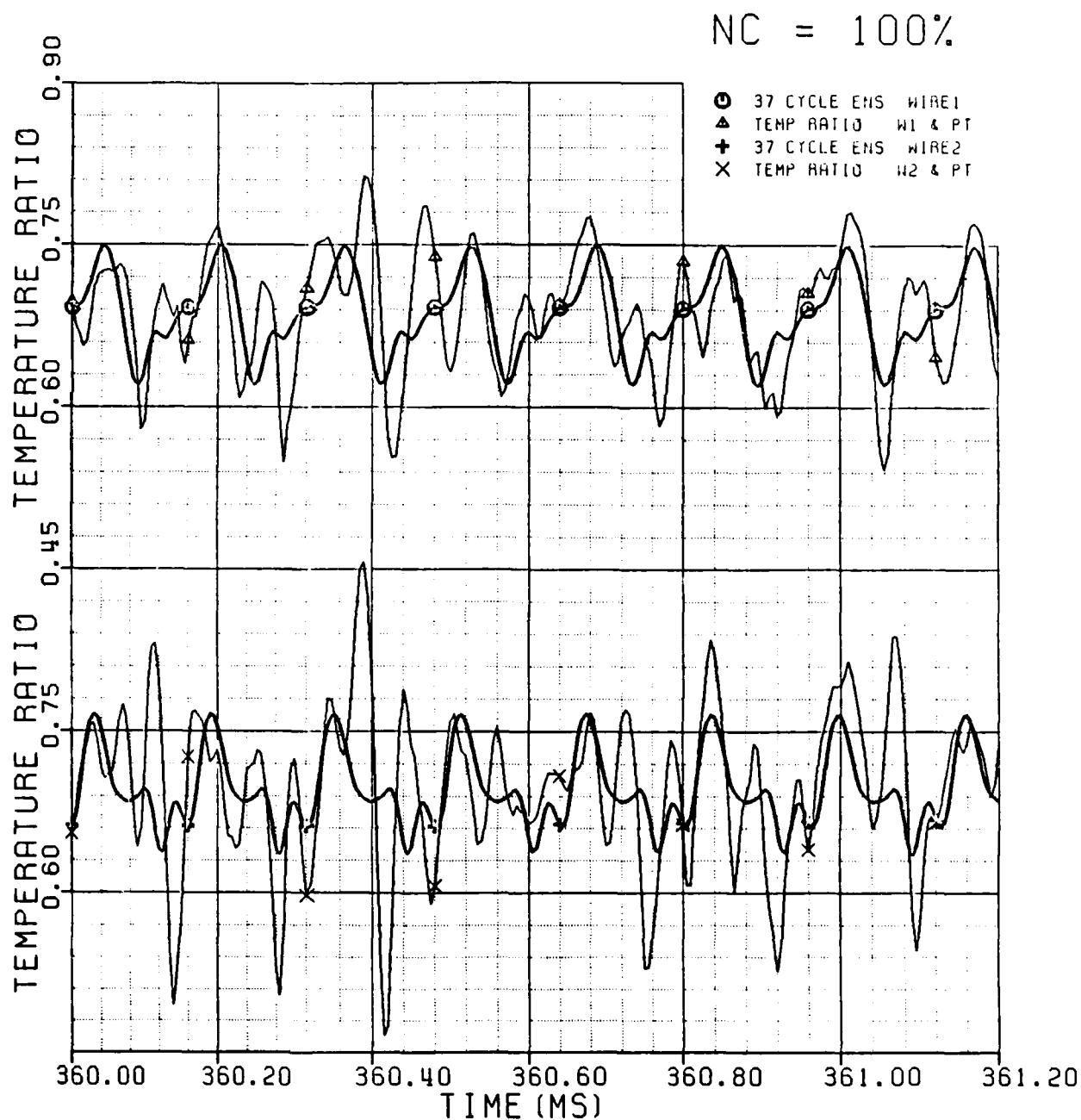
Figure 4-10:   Ensembled and Instantaneous Total Temperature
              Ratio at Time=360 msec and NC=100%
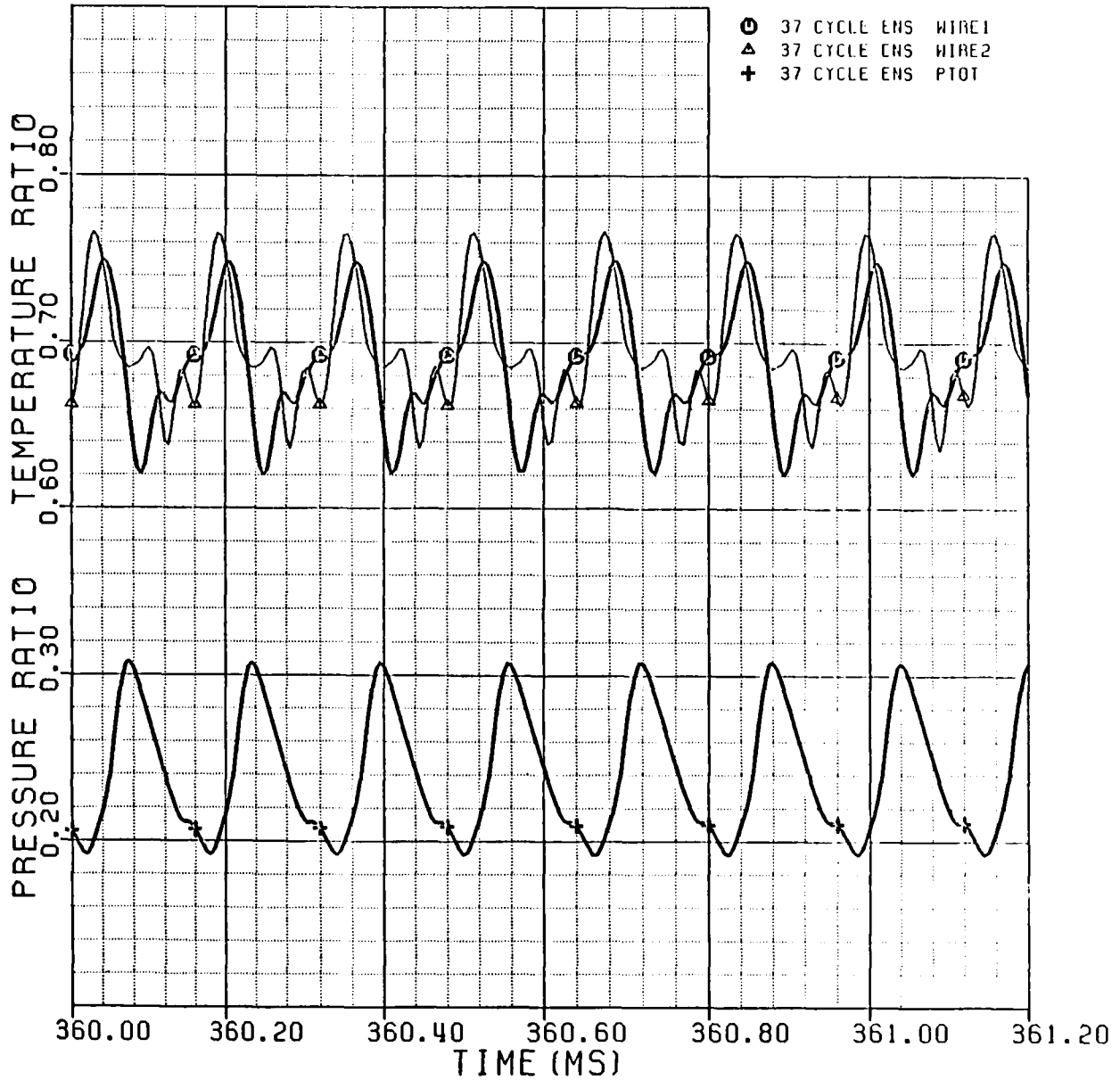
Figure 4-9: Total Temperature and Total Pressure Ratio at Time=360 msec and NC=100%
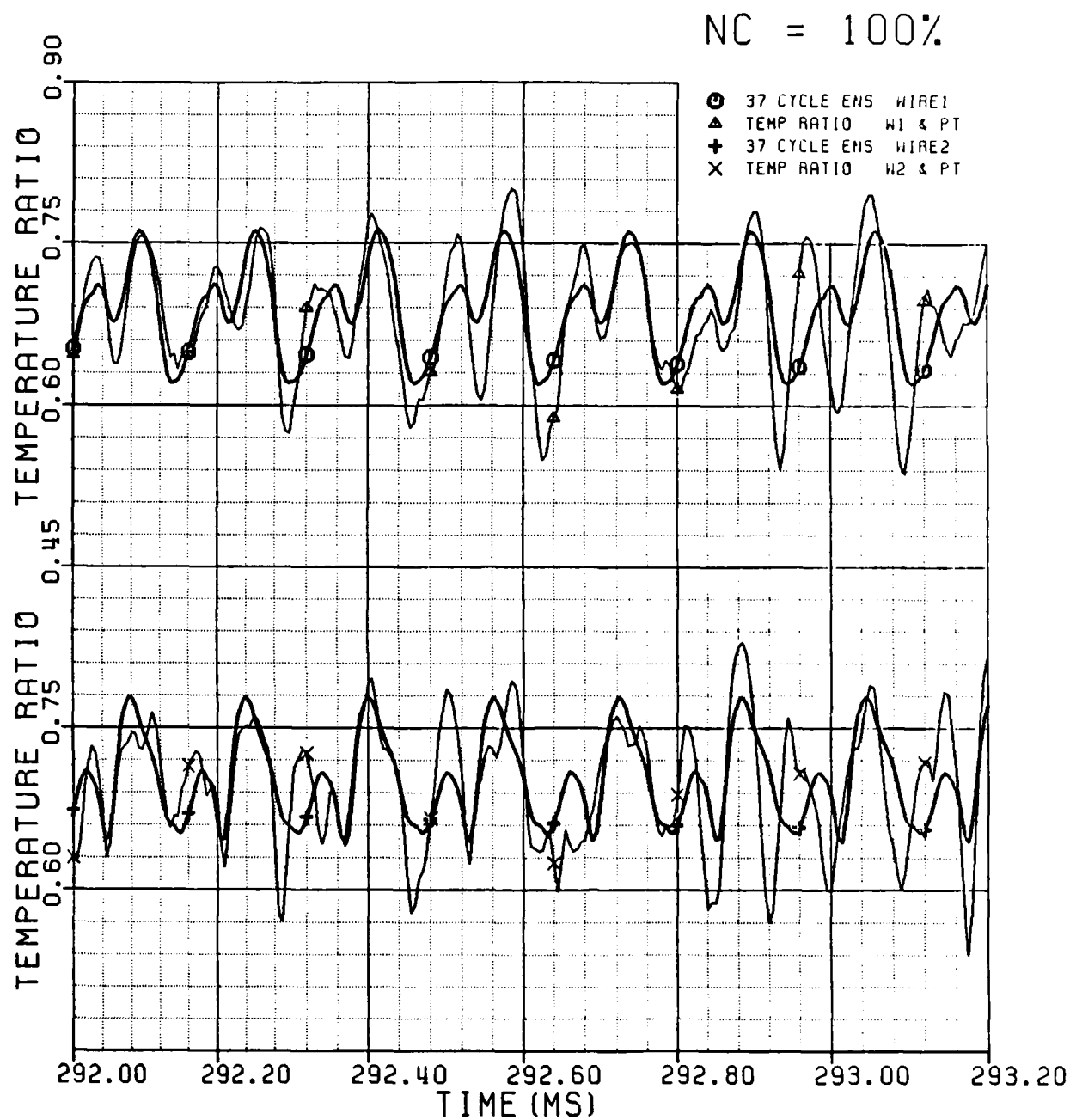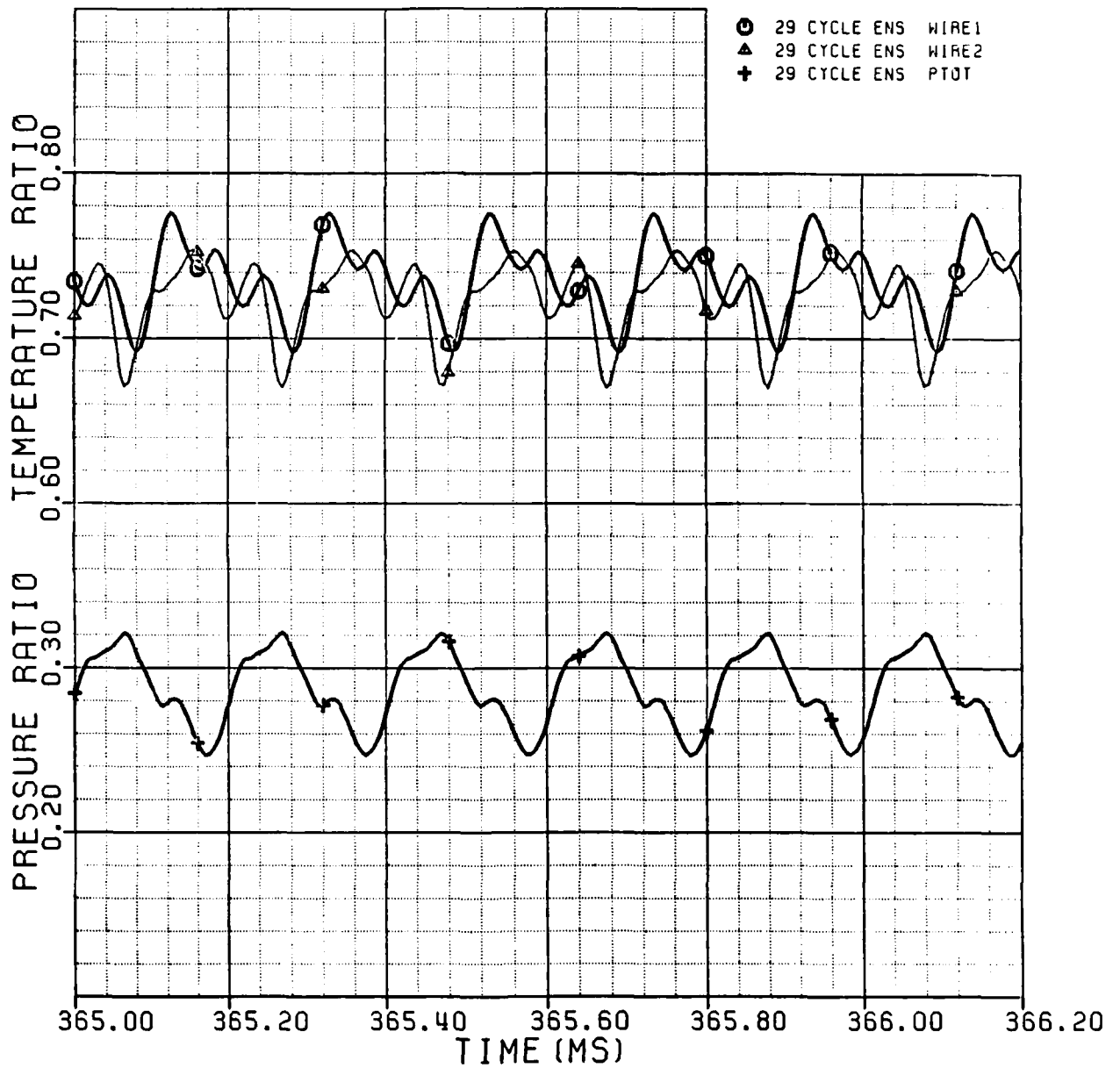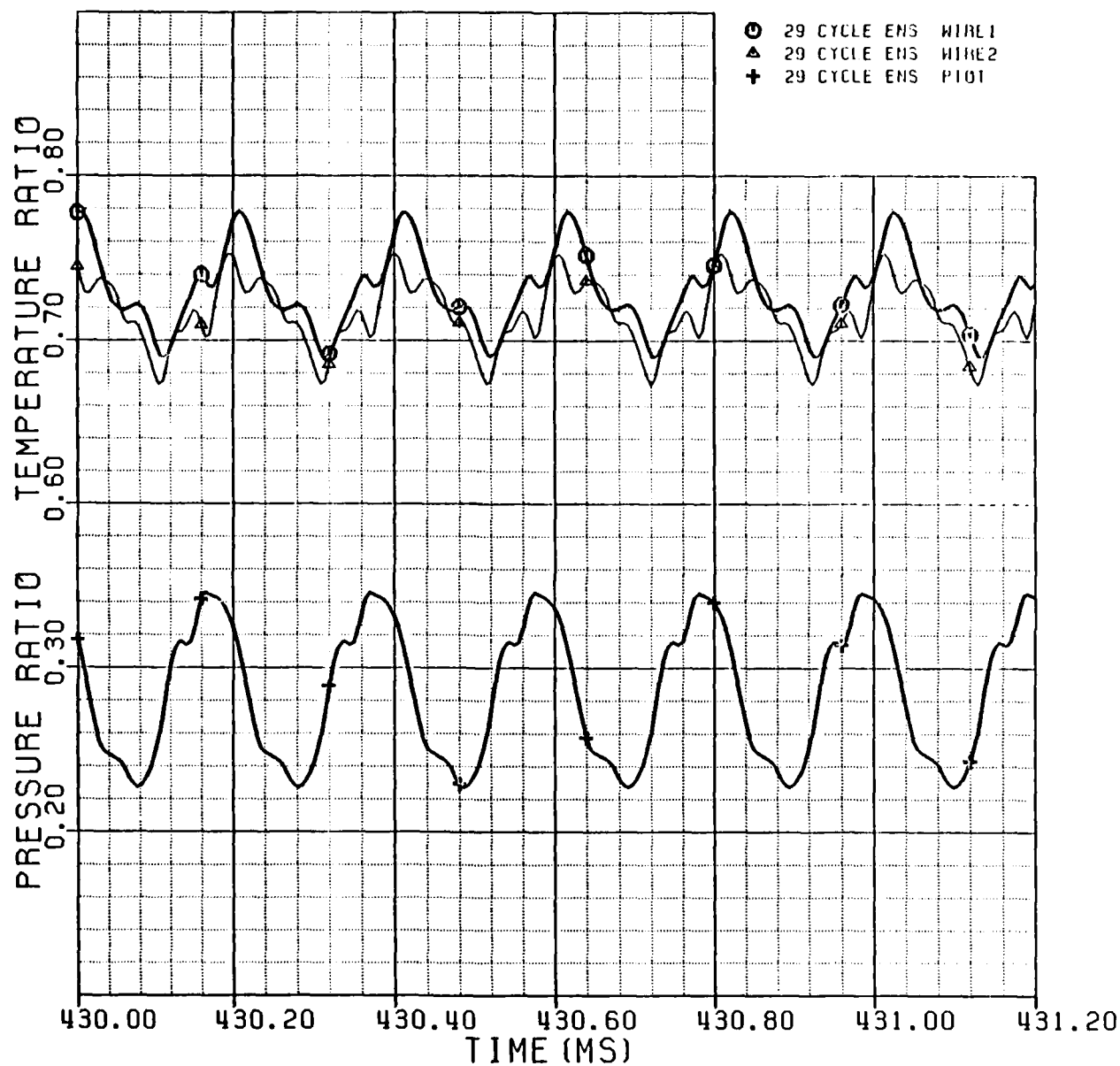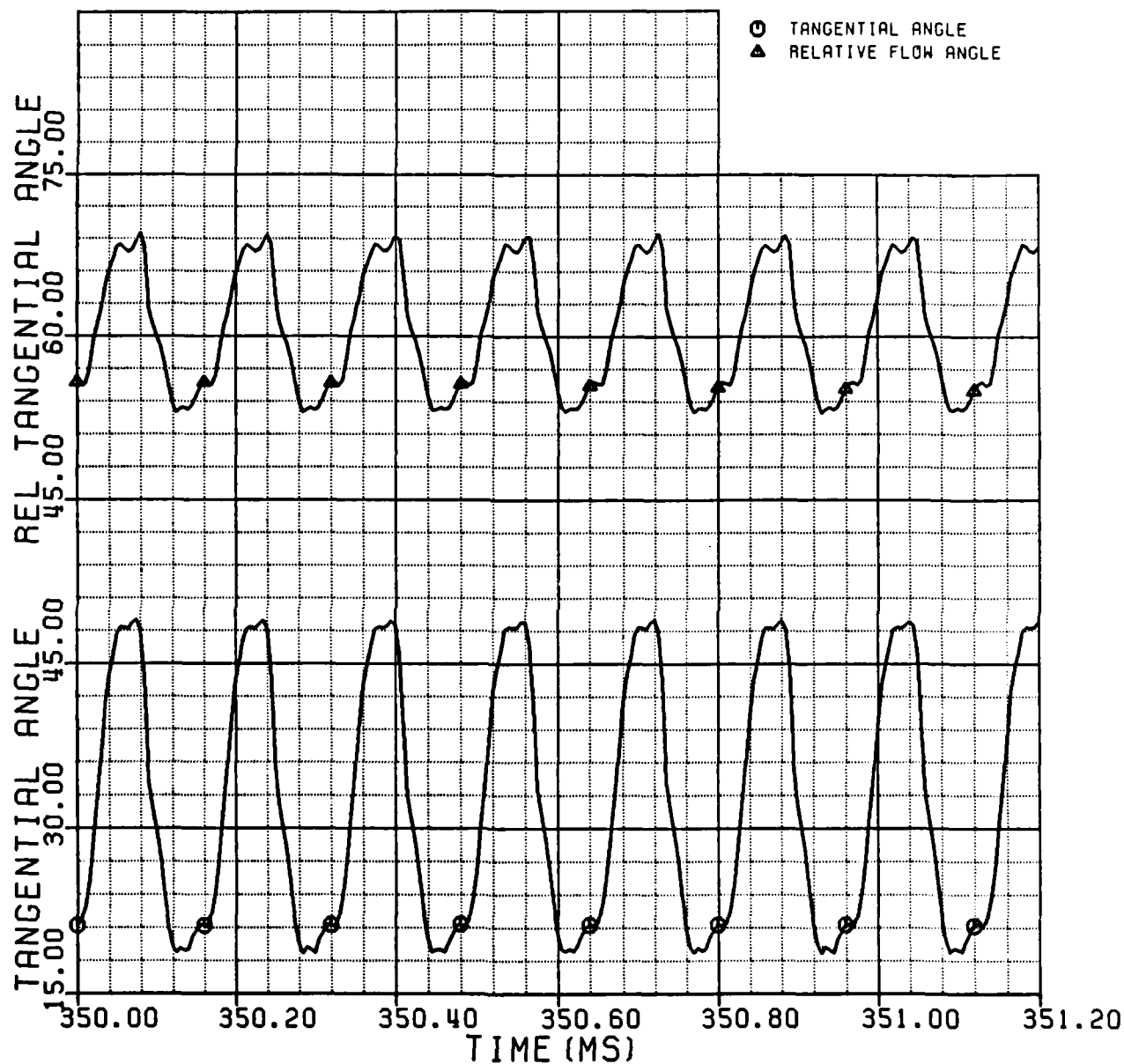
NC = 100%

Figure 4-8:   Ensembled and Instantaneous Total Temperature
              Ratio From Wire1 and Wire2. Time=292 msec

NC = 100%
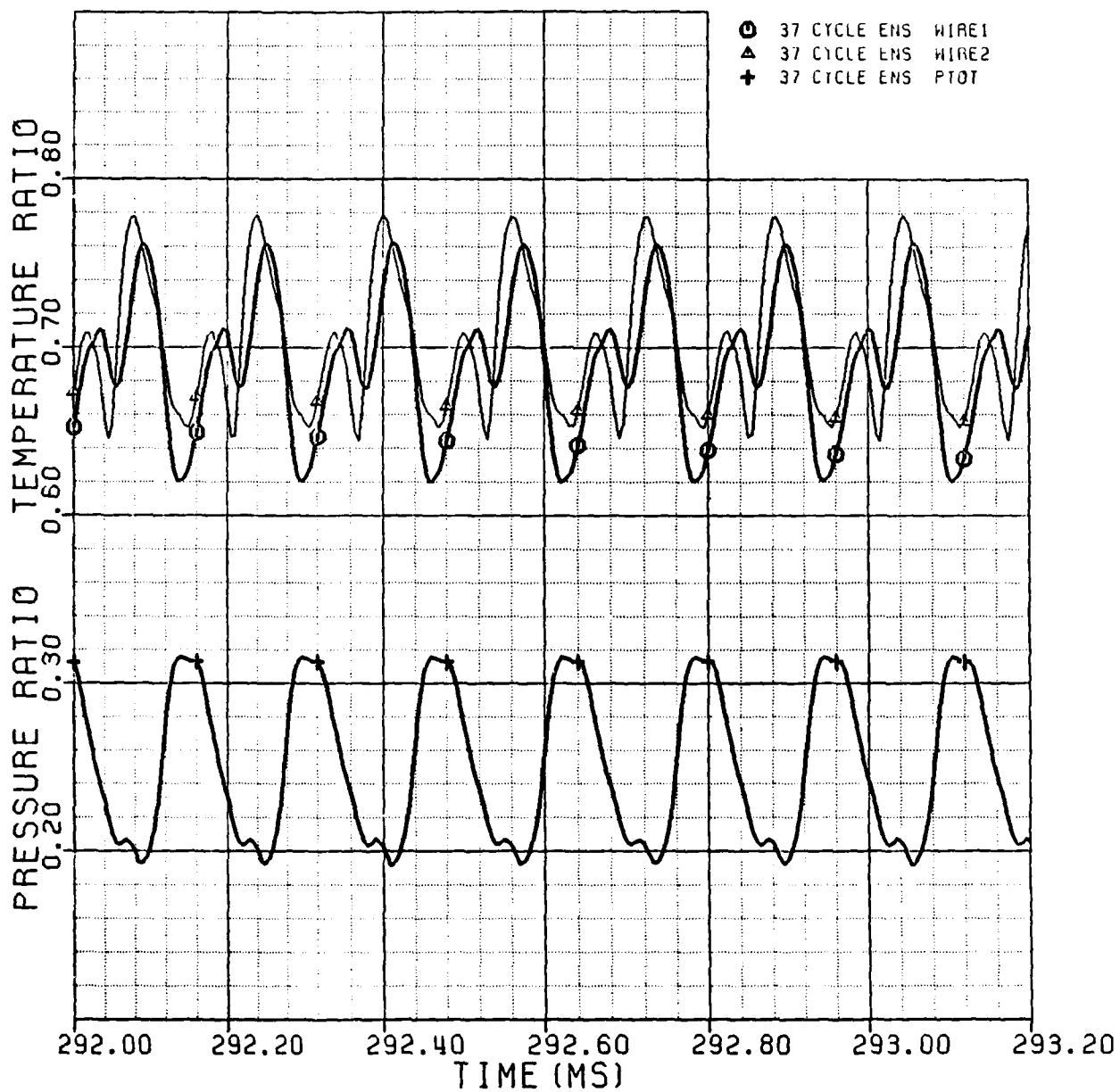
Figure 4-7: Total Temperature and Total Pressure Ratio
at Time=292 msec and NC=100%

NC = 100%

⊕ 111 CYCLE ENS WIRE1
△ TEMP RATIO W1 & PT

NC = 100%

⊕ 37 CYCLE ENS WIRE1
△ 7 CYCLE ENS WIRE1
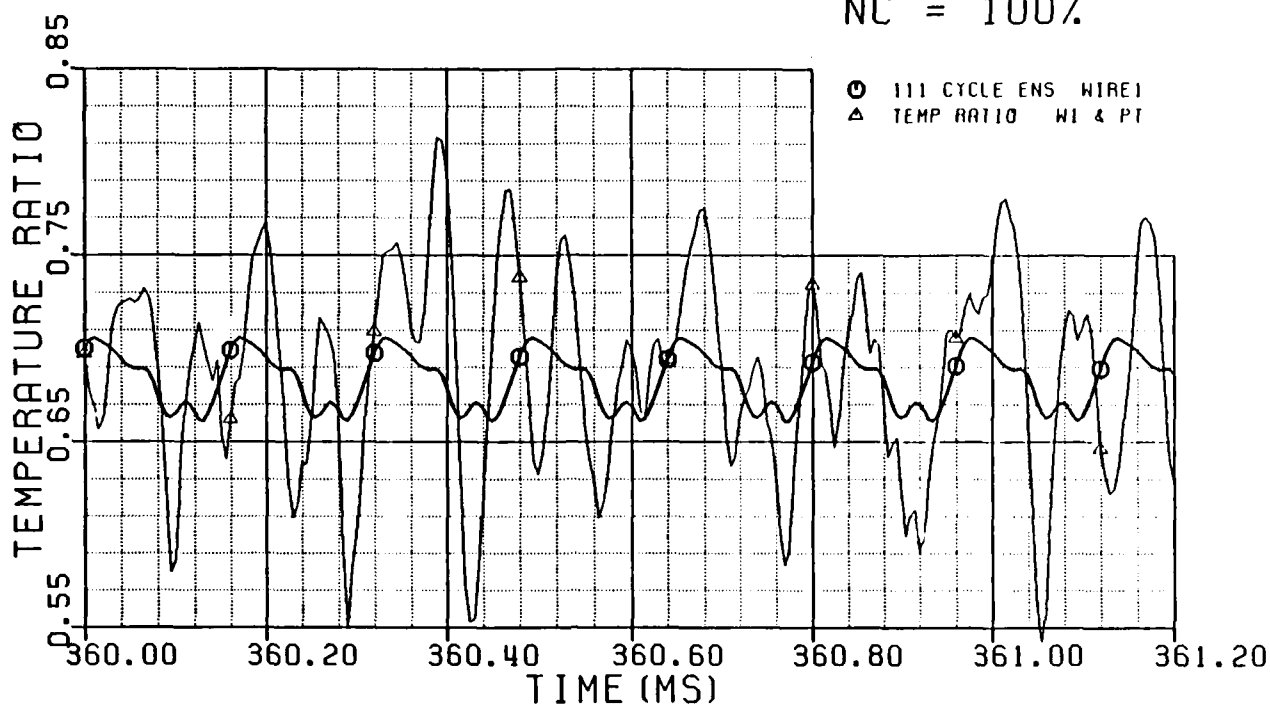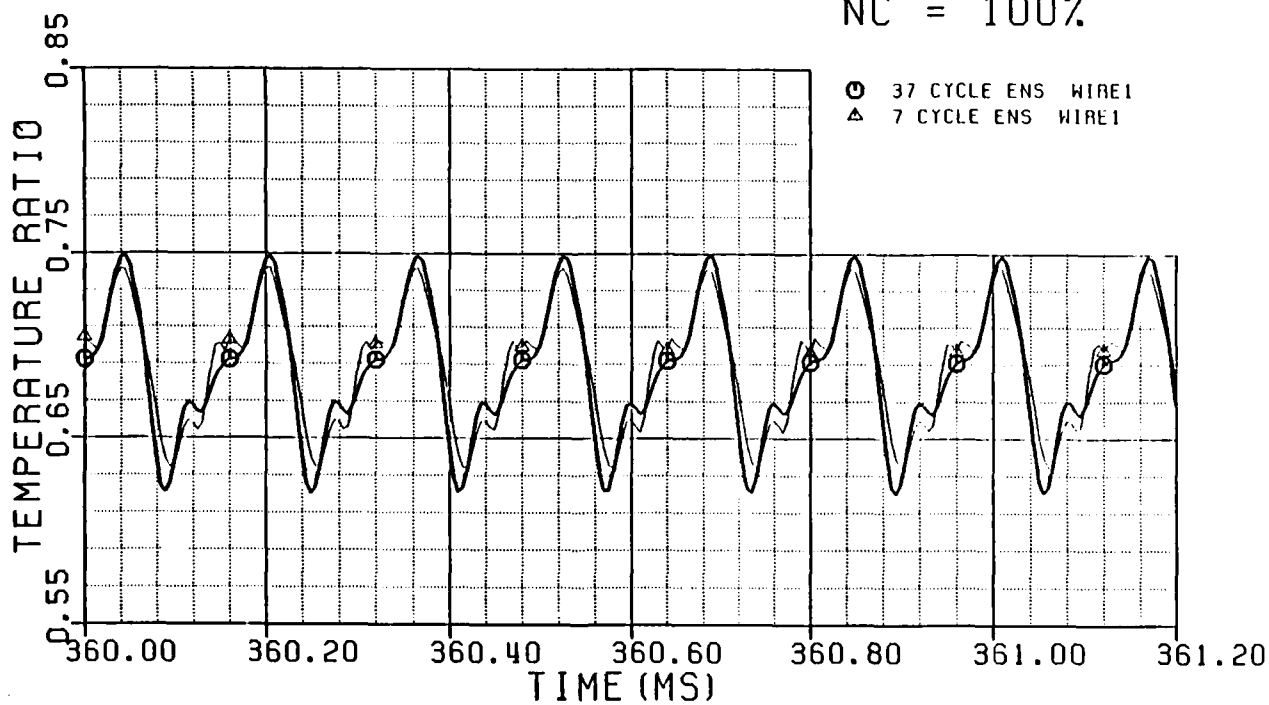
Figure 4-6B: Ensemble Average of Total Temperature Ratio with
                111 Cycle, NC=100%; Comparison of 111 and 7
                Cycle Ensemble Averages, Time=360 msec
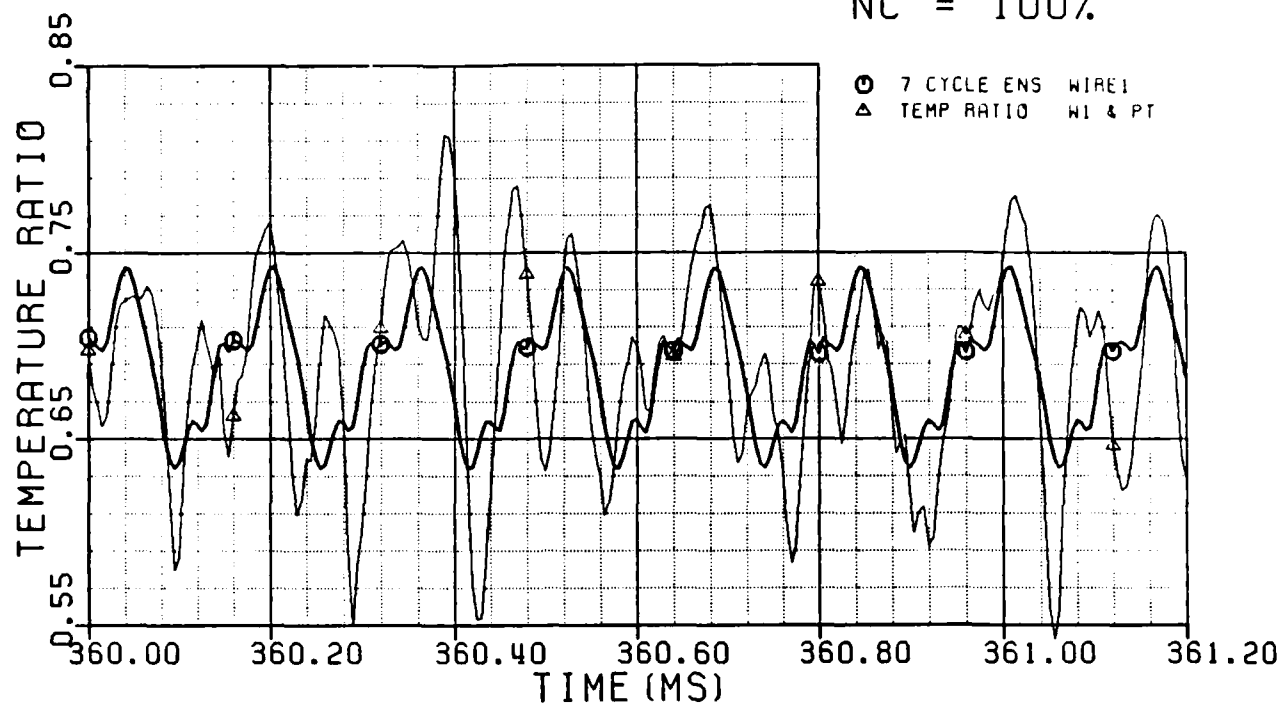
NC = 100%

NC = 100%
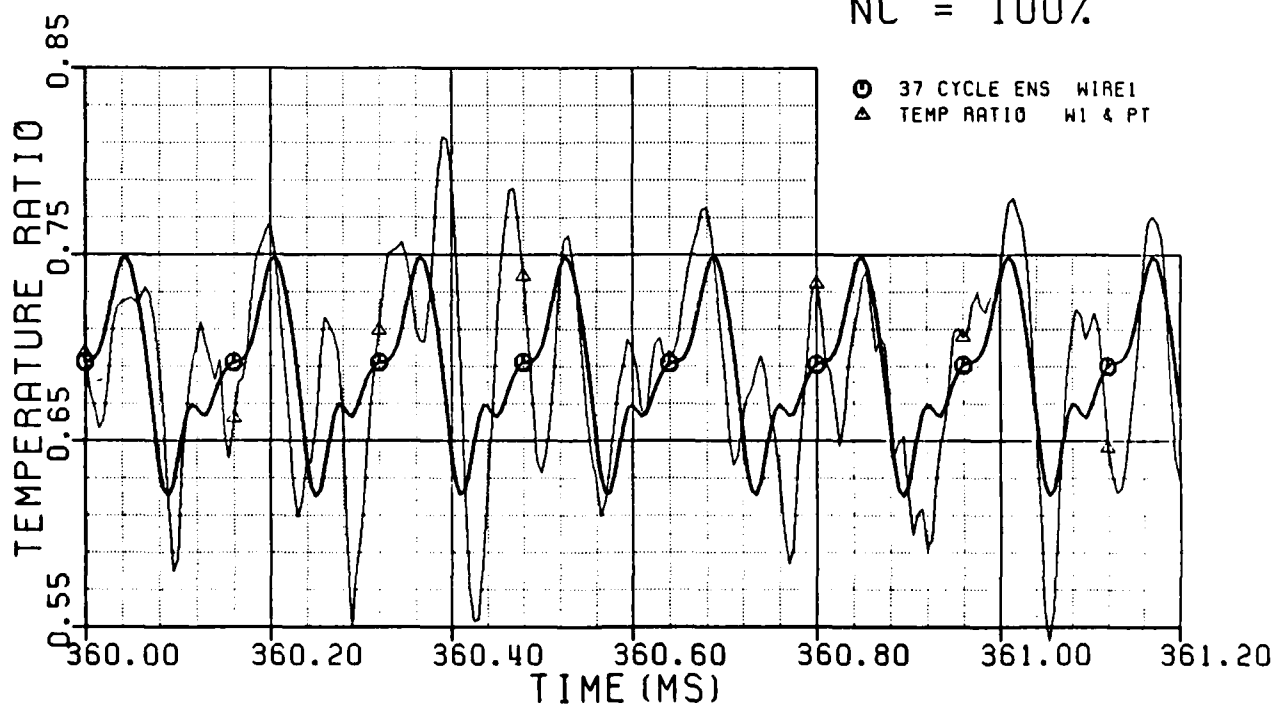
Figure 4-6A: Ensemble Average of Total Temperature Ratio with
7 and 37 Cycles; NC=100%, Time=360 msec
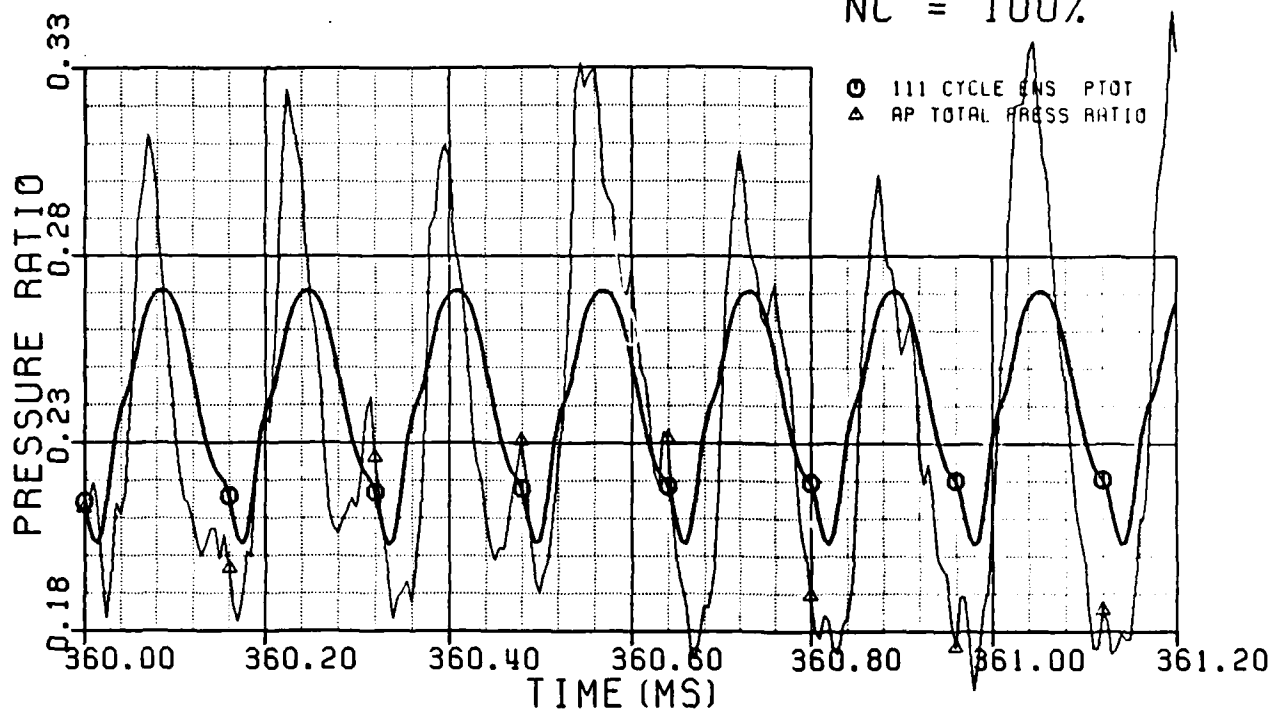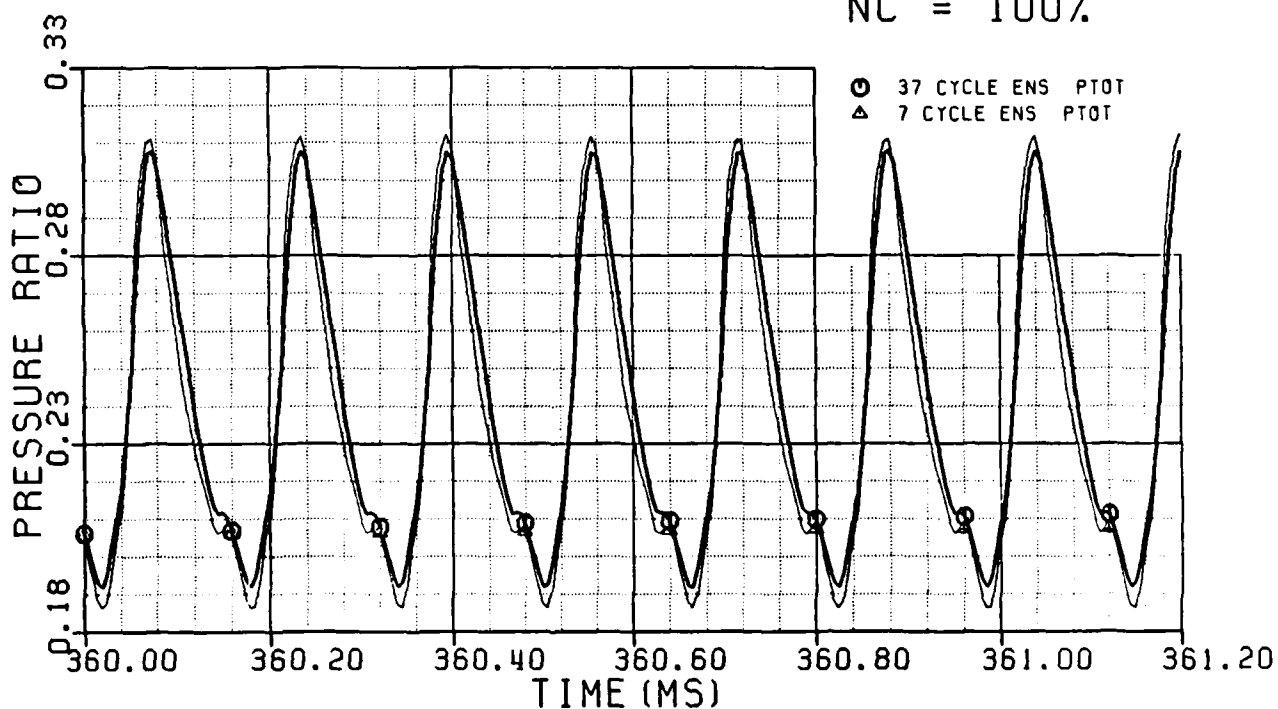
Figure 4-58: Ensemble Average of Total Pressure Ratio with
111 Cycle, NC=100%; Comparison of 37 and 7
Cycle Ensemble Averages, Time=360 msec

NC = 100%

⊙ 7 CYCLE ENS PTOT
△ AP TOTAL PRESS RATIO

TIME (MS)

NC = 100%

⊙ 37 CYCLE ENS PTOT
△ AP TOTAL PRESS RATIO

TIME (MS)
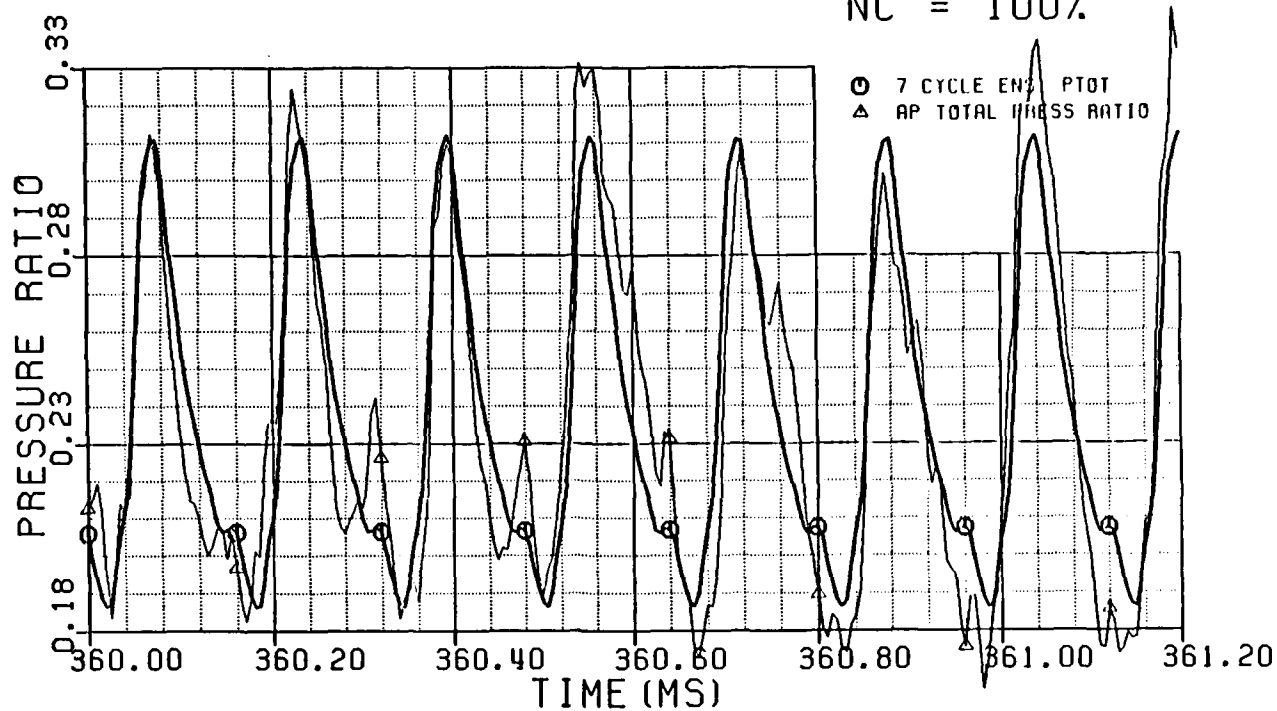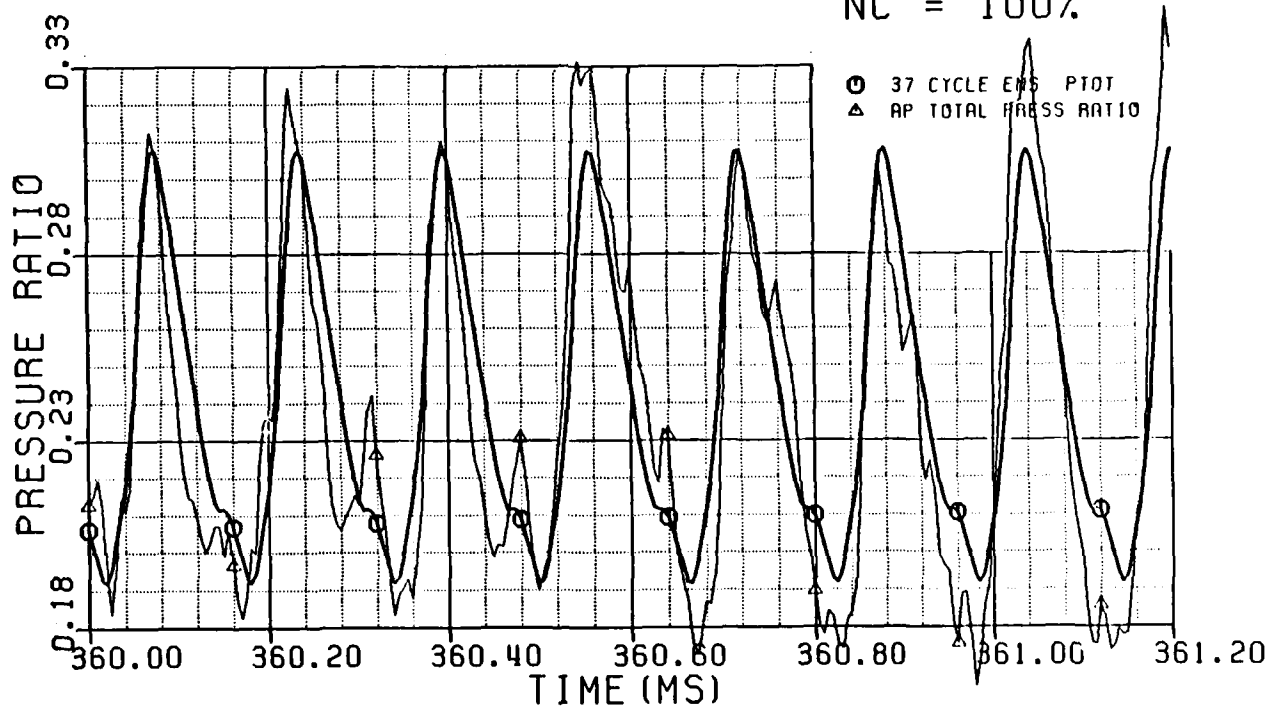
Figure 4-5A: Ensemble Average of Total Pressure Ratio with
7 and 37 Cycles; NC=100%, Time=360 msec

NC = 100%

○ 111 CYCLE ENS WIRE1
△ TEMP RATIO W1 & PT

NC = 100%

○ 111 CYCLE ENS WIRE1
△ 7 CYCLE ENS WIRE1
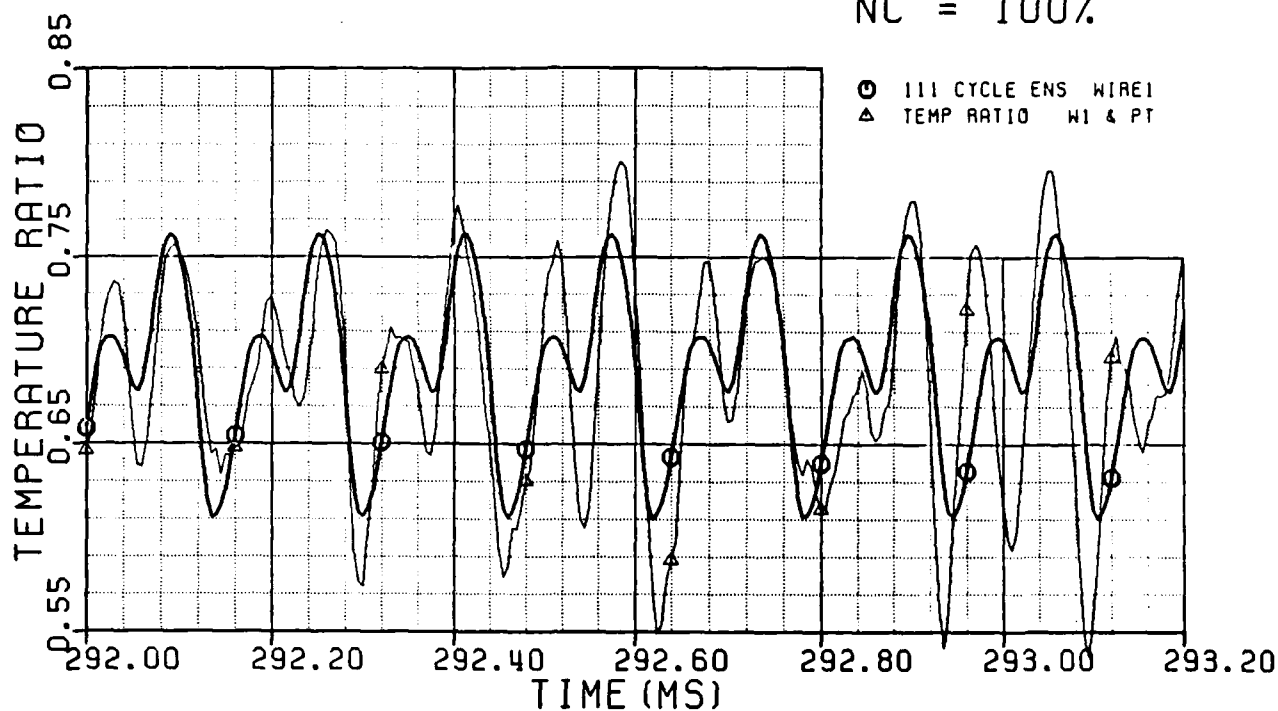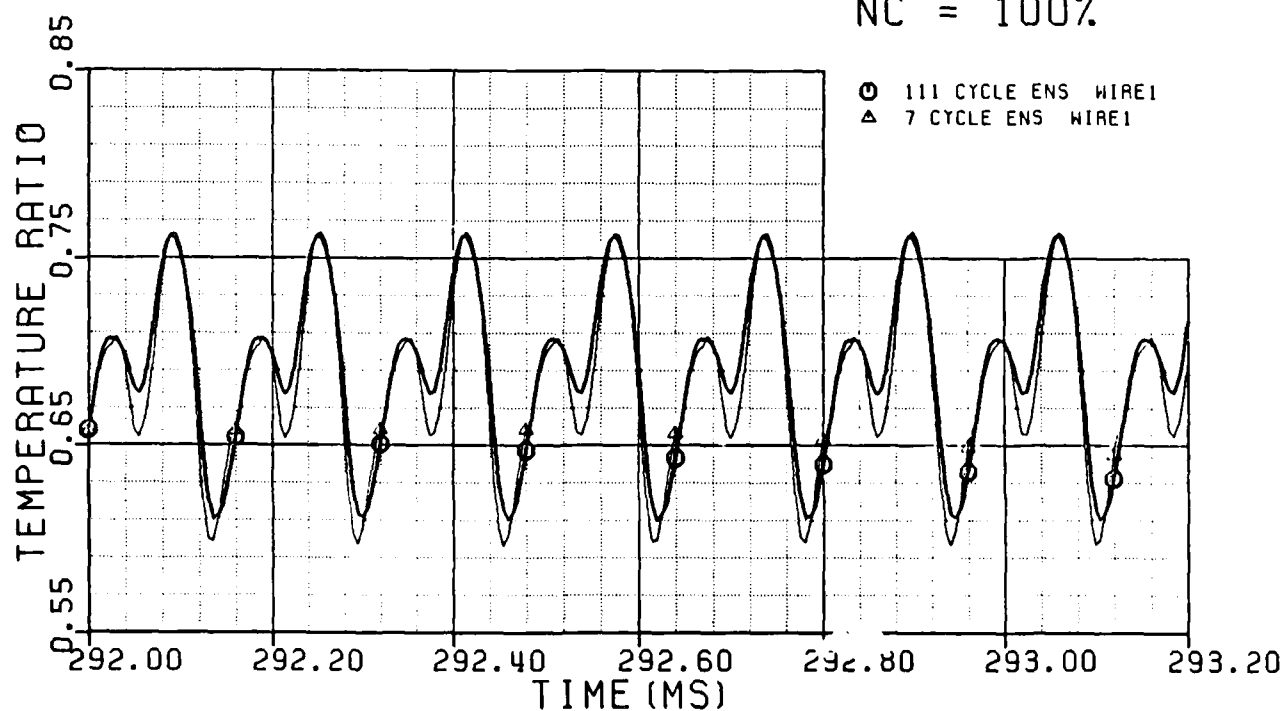
Figure 4-4B: Ensemble Average of Total Temperature Ratio with
111 Cycle, NC=100%; Comparison of 111 and 7
Cycle Ensemble Averages, Time=292 msec
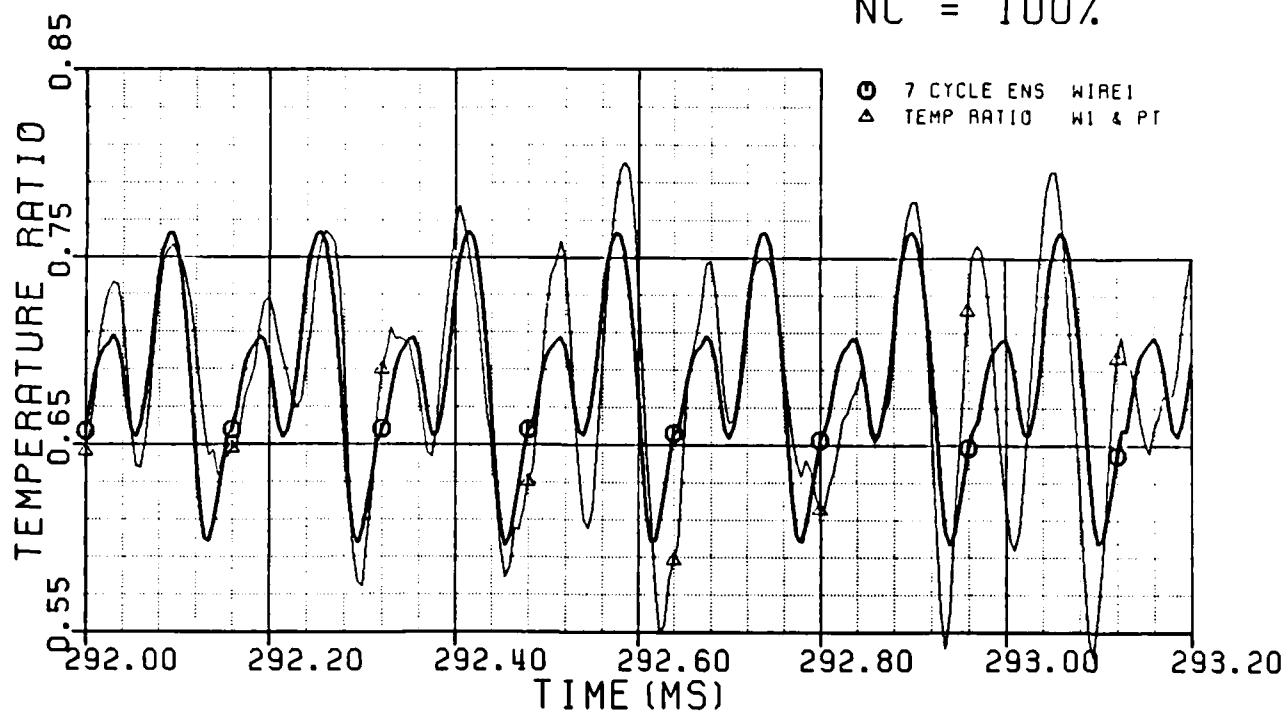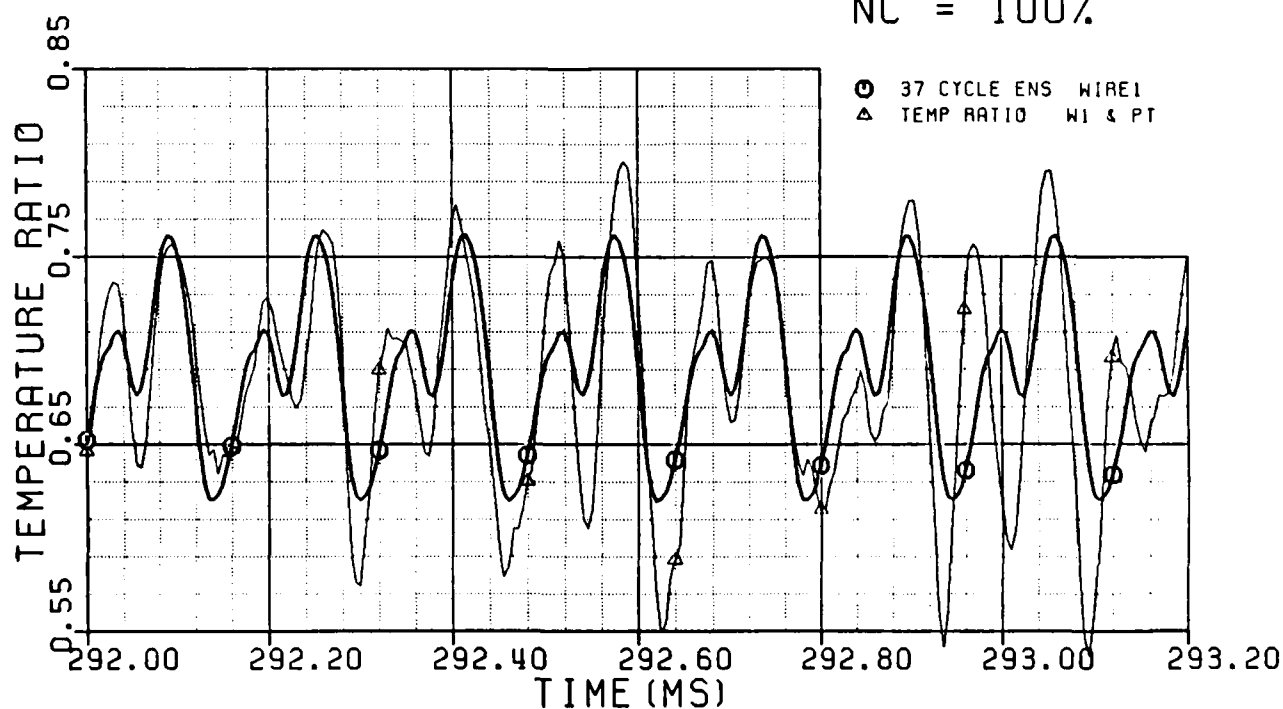
Figure 4-4A: Ensemble Average of Total Temperature Ratio with 7 and 37 Cycles; NC=100%, Time=292 msec

NC = 100%
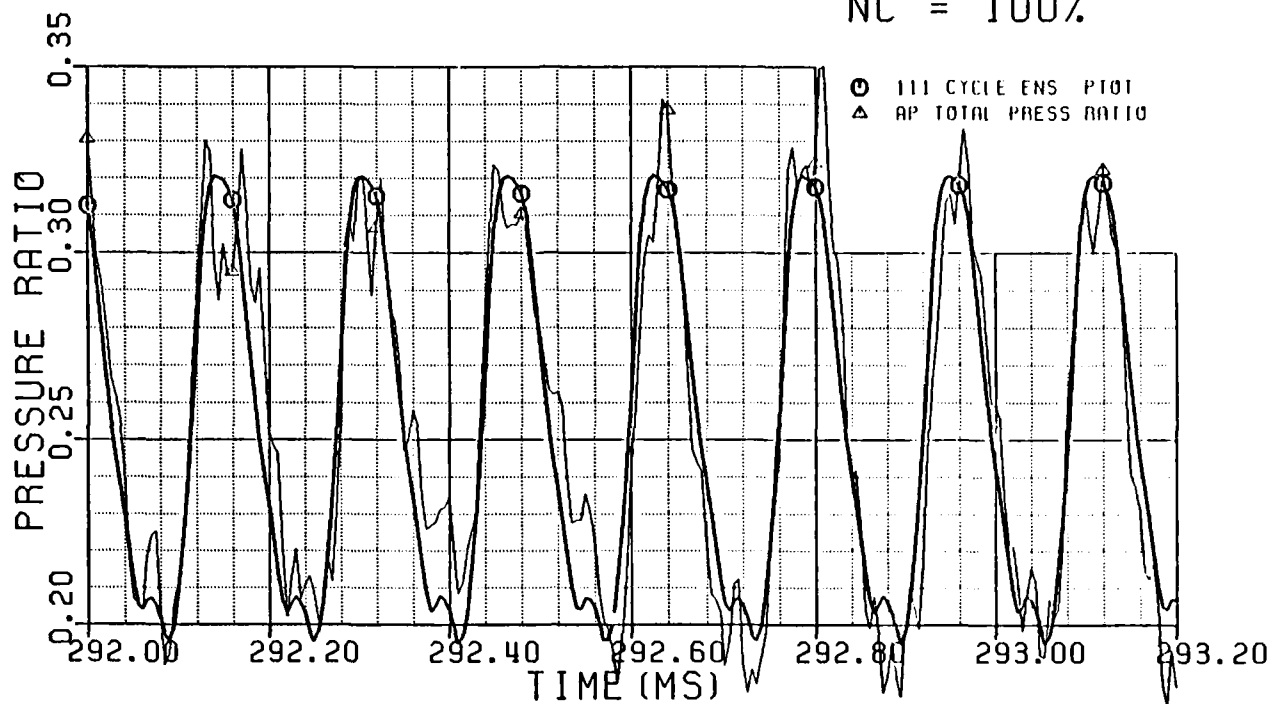
NC = 100%
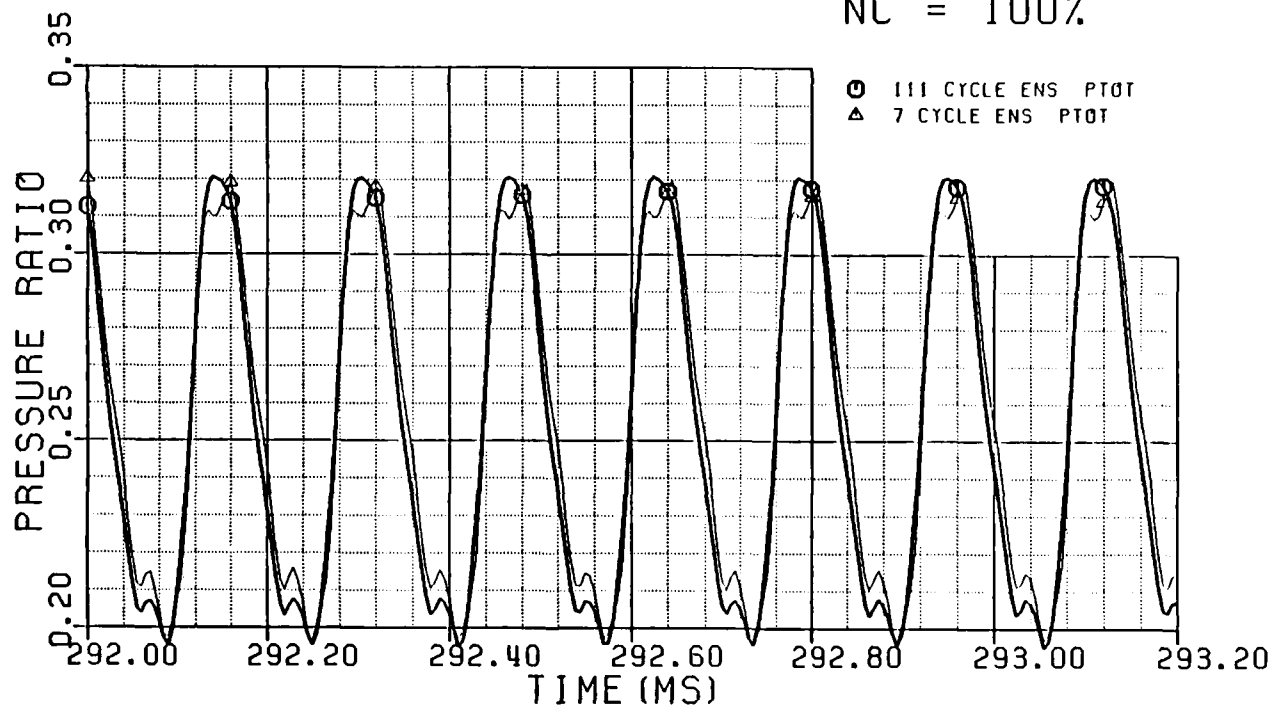
Figure 4-3B: Ensemble Average of Total Pressure Ratio with
111 Cycle, NC=100%; Comparison of 111 and 7
Cycle Ensemble Averages, Time=292 msec

NC = 125%
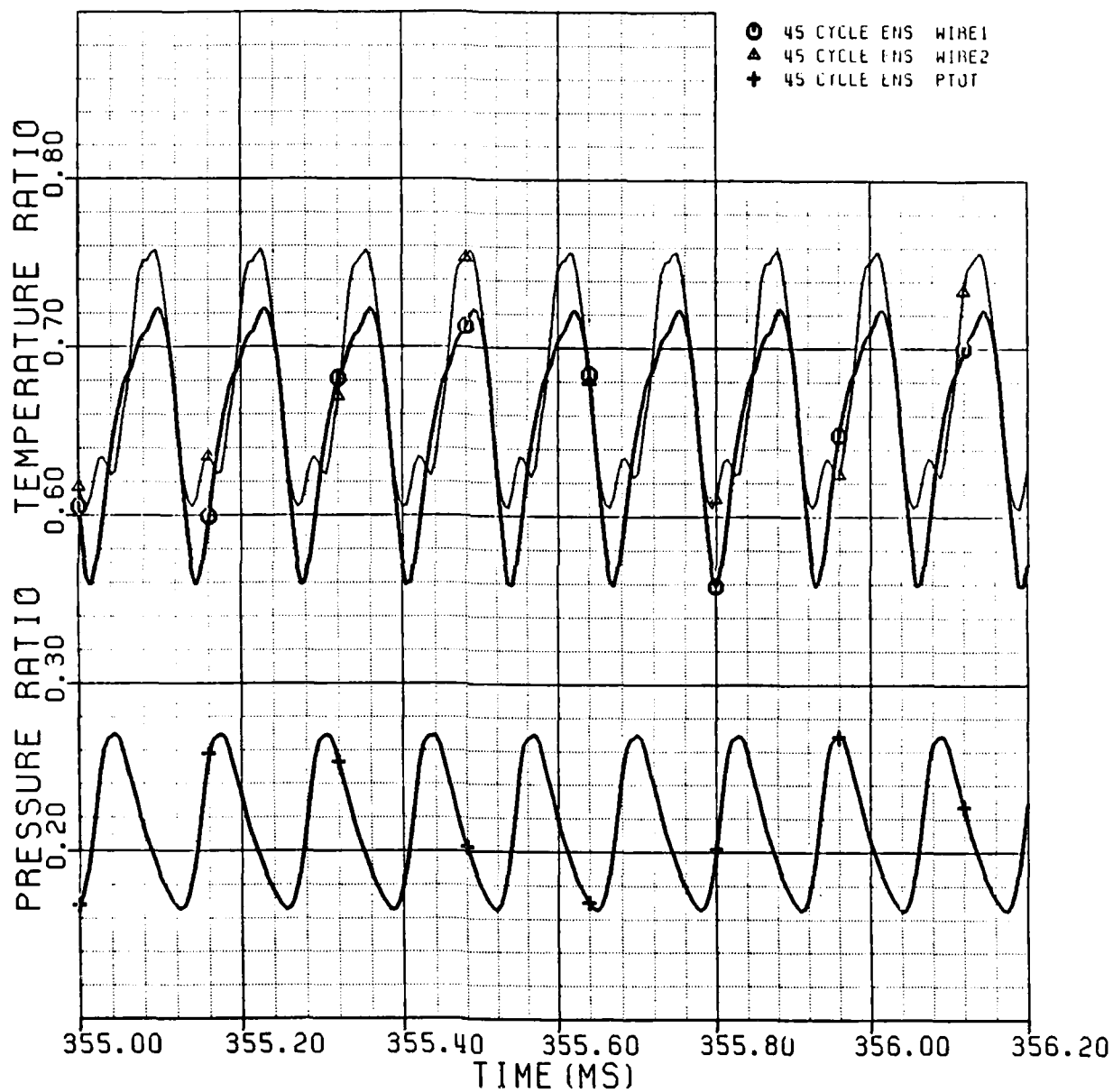
Figure 4-14: Total Temperature and Total Pressure Ratio
at Time=355 msec and NC=125%

NC = 125%
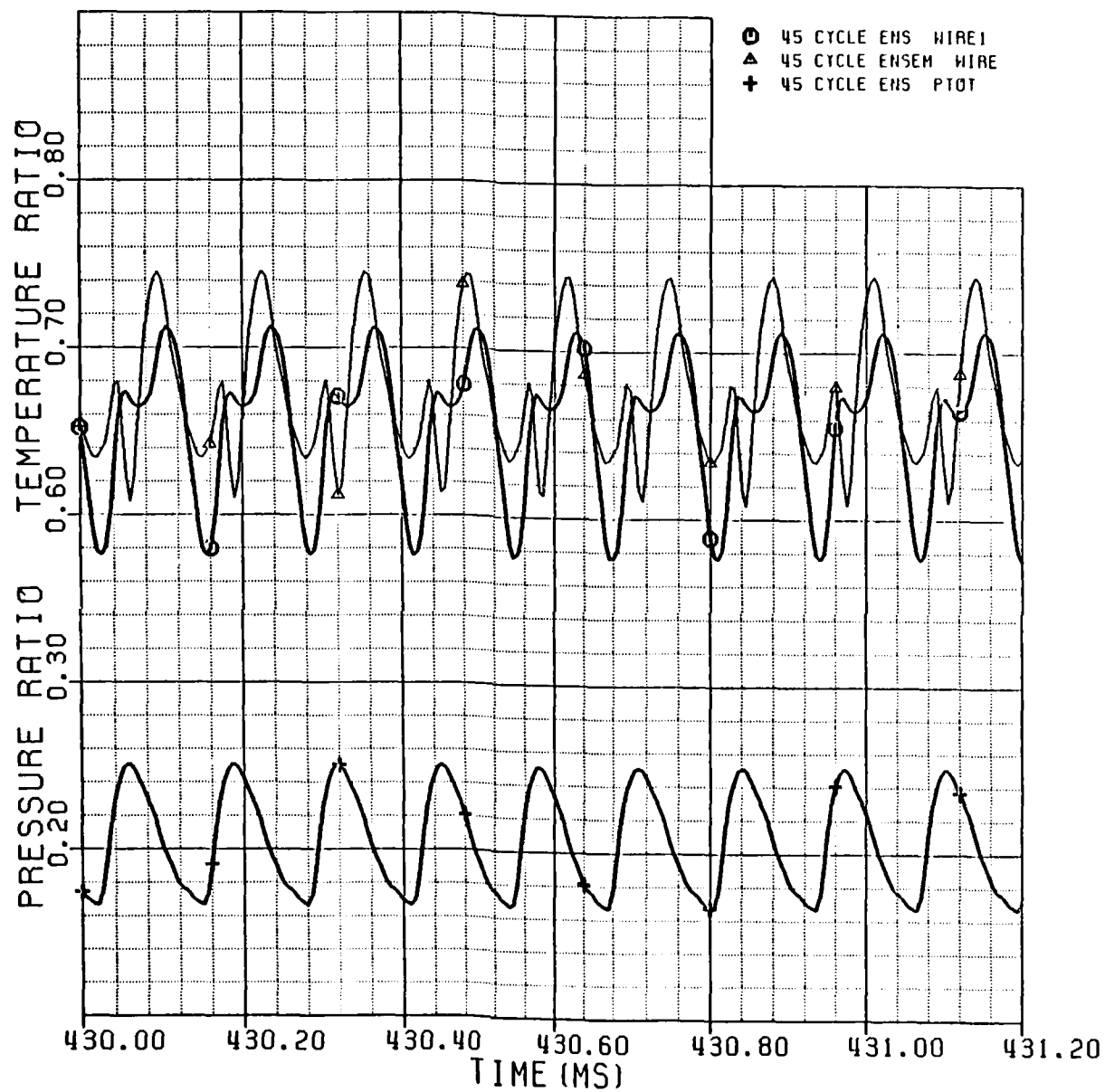
Figure 4-15: Total Temperature and Total Pressure Ratio
at Time=430 msec and NC=125%

NC = 80%
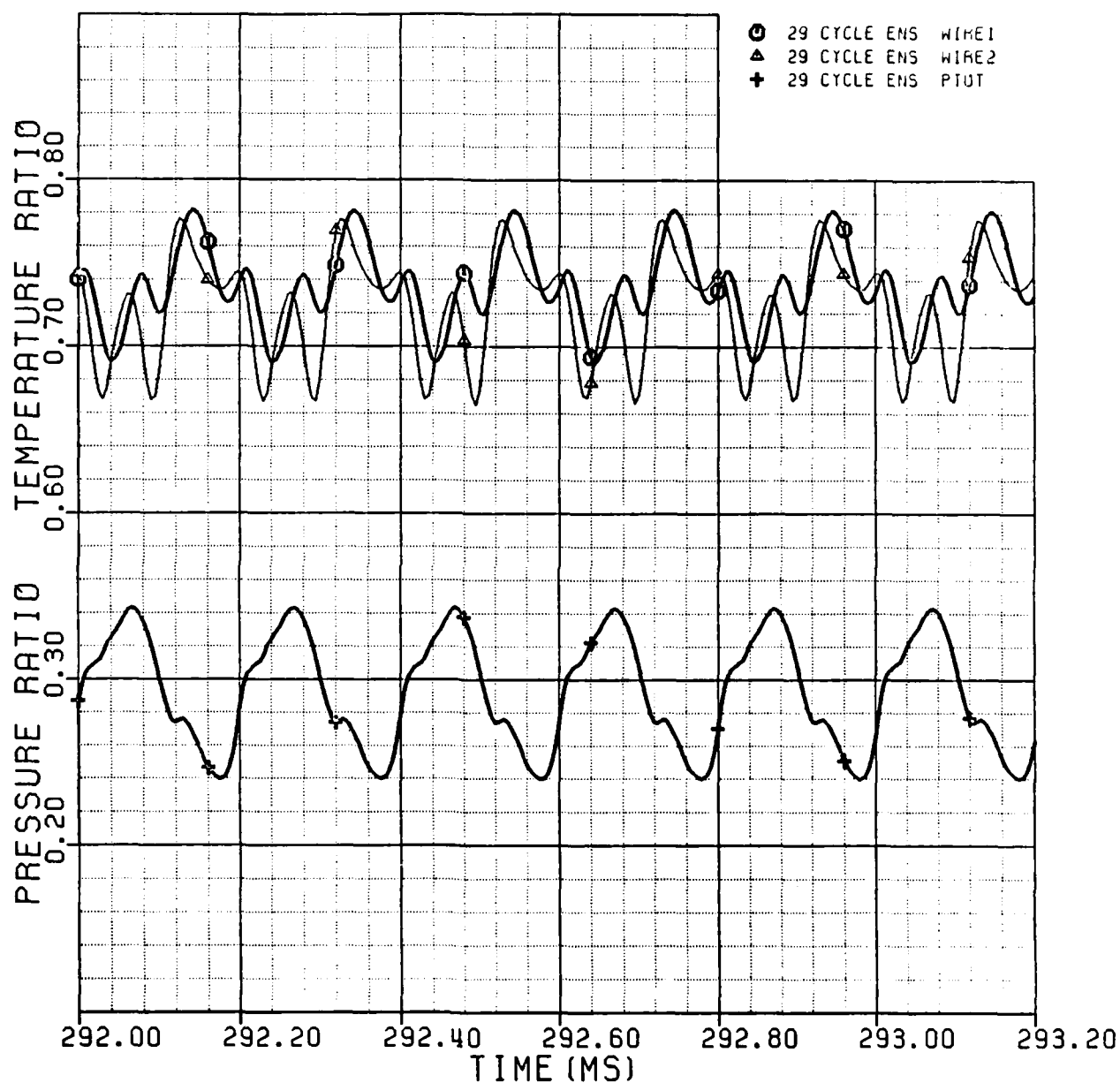
Figure 4-16: Total Temperature and Total Pressure Ratio
at Time=292 msec and NC=80%

NC = 80%

Figure 4-17: Total Temperature and Total Pressure Ratio
at Time=365 msec and NC=80%

NC = 80%

Figure 4-18: Total Temperature and Total Pressure Ratio
at Time=430 msec and NC=80%

NC = 100%

Figure 4-19: Absolute and Relative Tangential Flow
Angle Versus Time

NC = 100%

⊙ TOTAL PRESSURE
▲ ABSOLUTE MACH NUMB
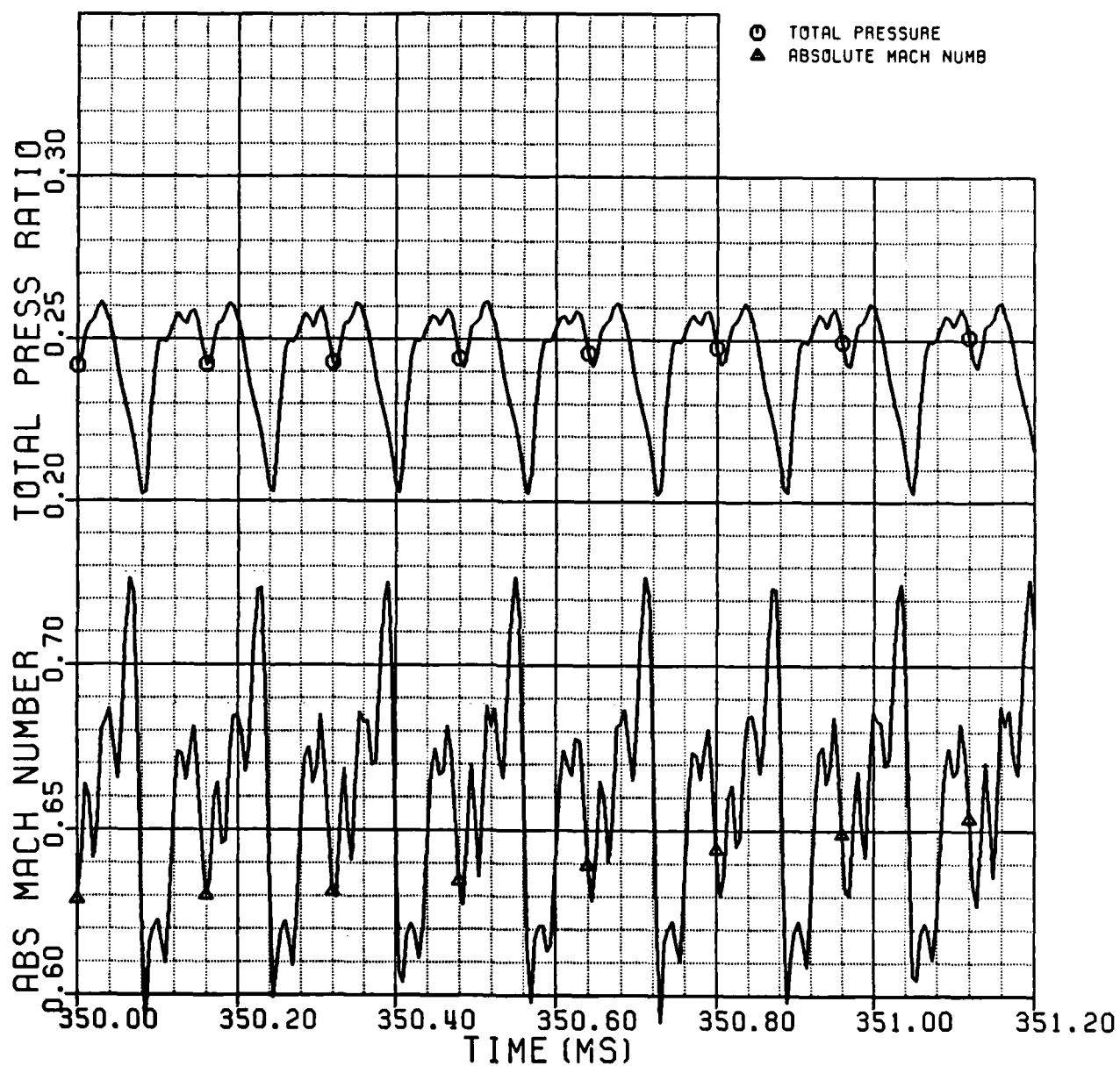
Figure 4-20: Total Pressure Ratio and Absolute Mach
Number Versus Time

Figure 4-21: Total Pressure Ratio and Axial Mach Number
Versus Time
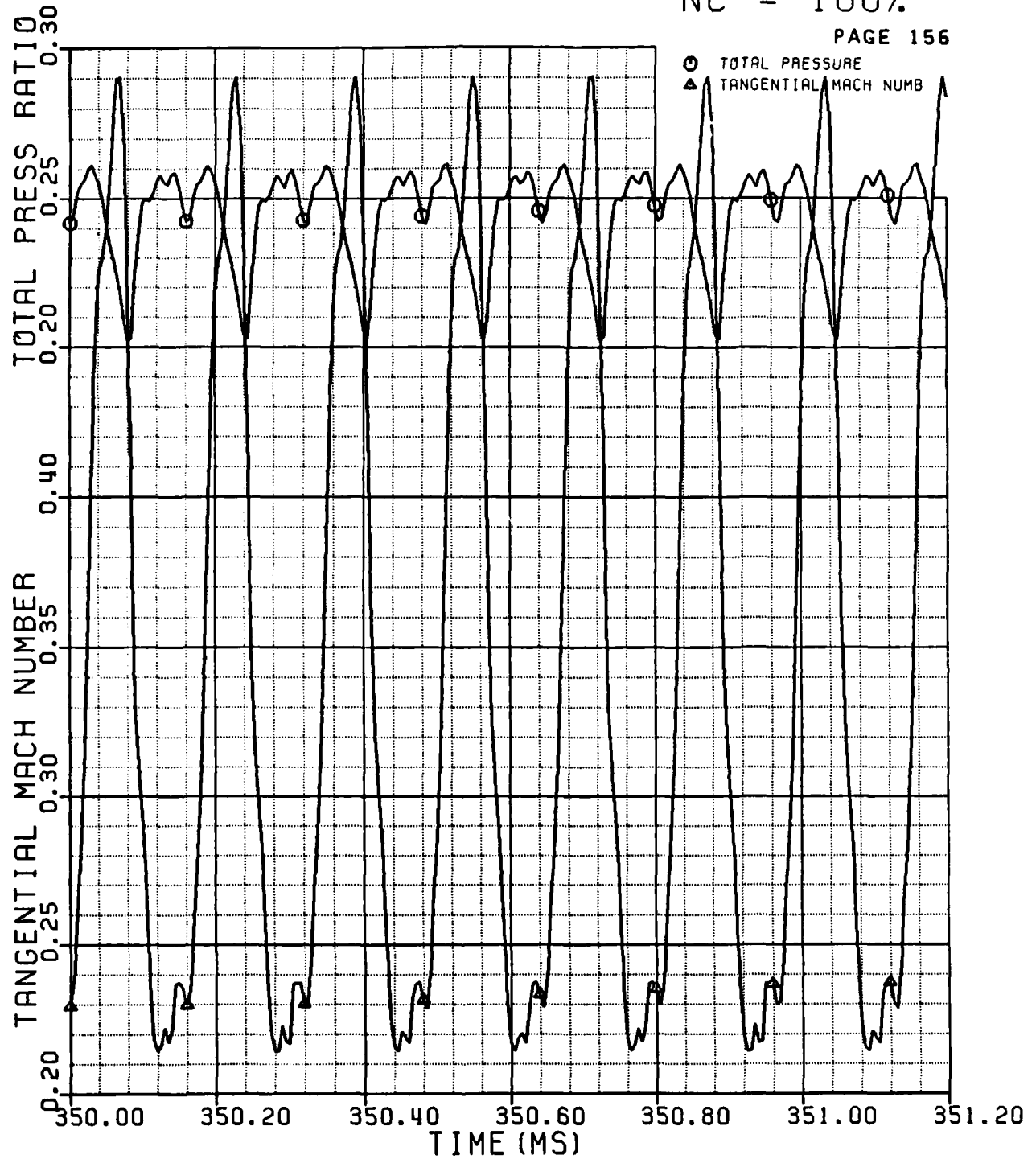
Figure 4-22:   Total Pressure Ratio and Tangential Mach
Number Versus Time
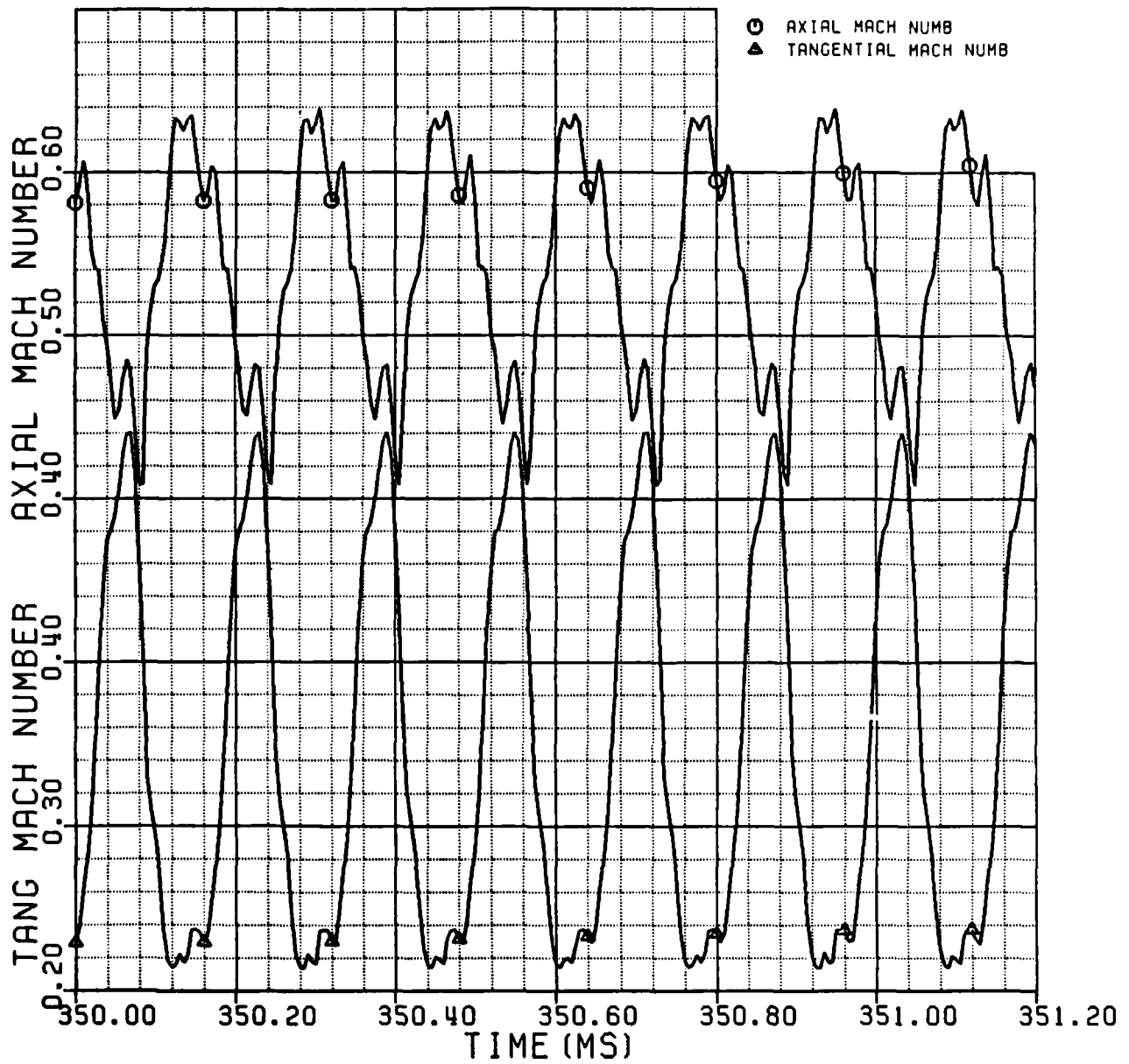
NC = 100%

Figure 4-23: Axial and Tangential Mach Number Versus Time

NC = 100%

○ TOTAL PRESSURE
△ STATIC PRESSURE
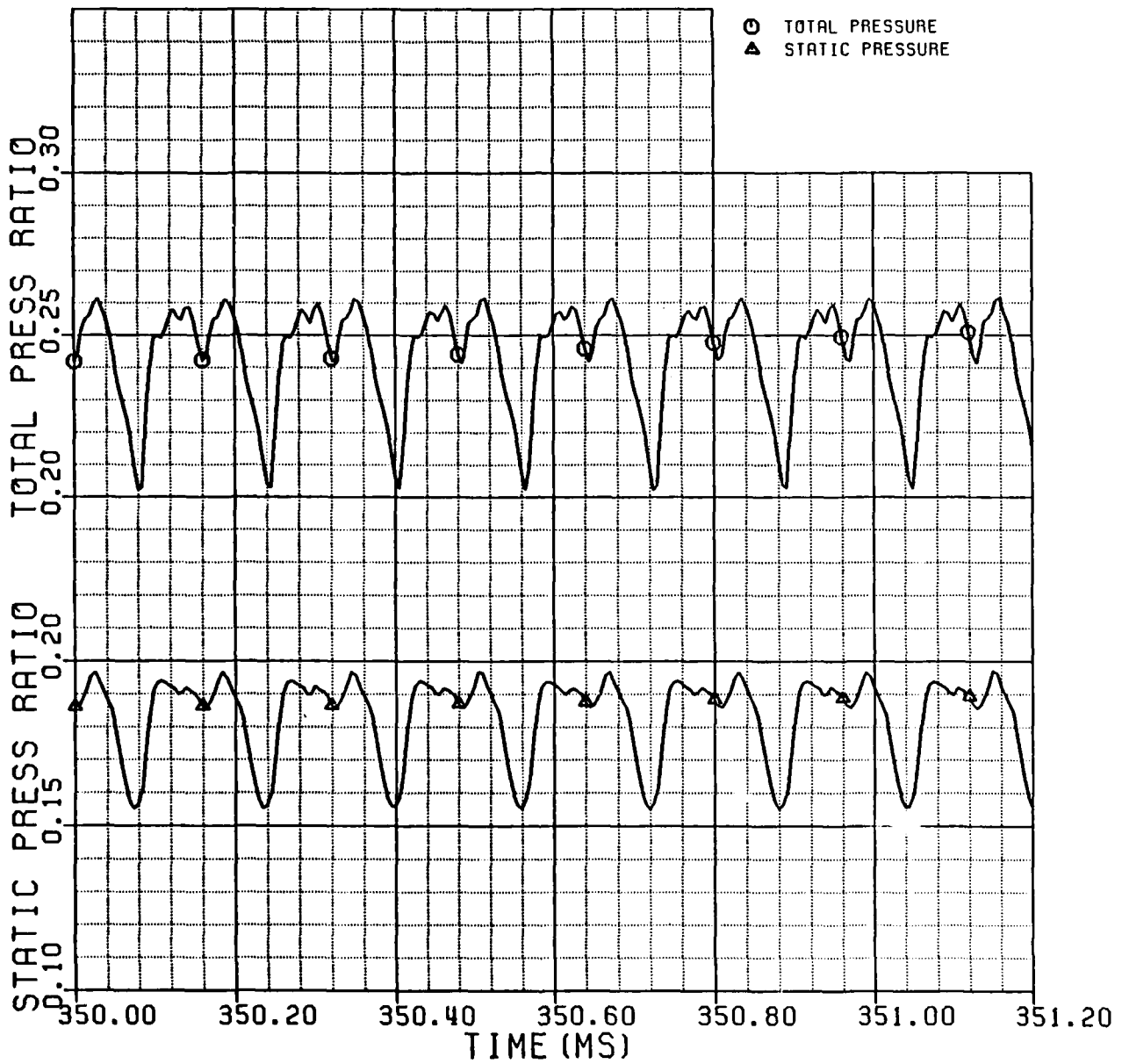
Figure 4-24: Total and Static Pressure Ratios Versus
Time
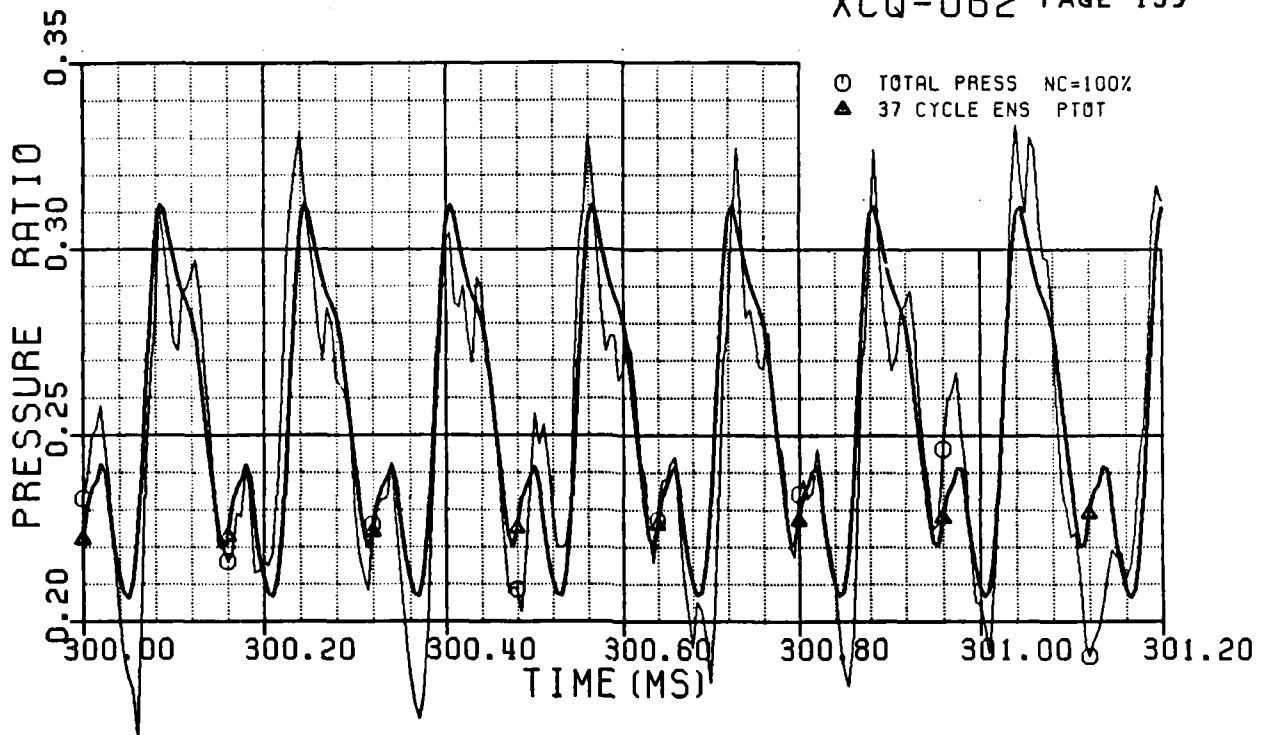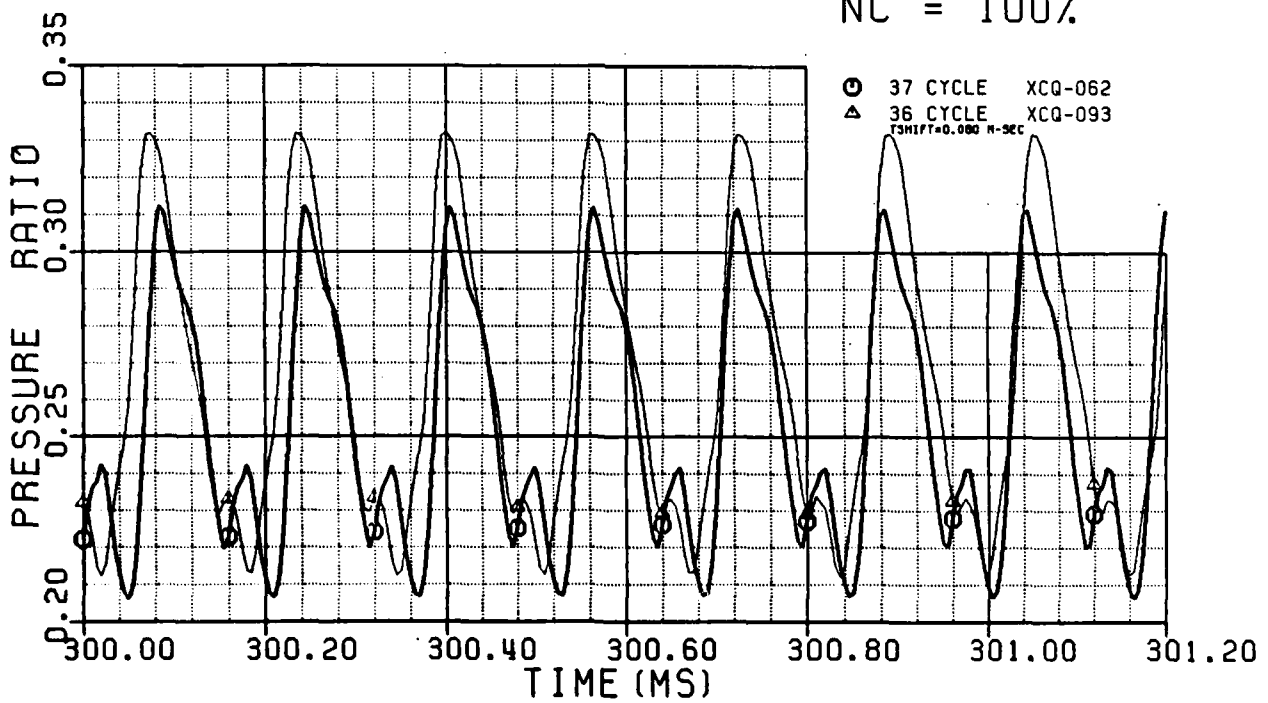
Figure 4-25: Comparison of Total Pressure Ratio as
Measured by XCQ-Ø93 and XCQ-Ø63 Silicon
Diaphragm Pressure Transducers
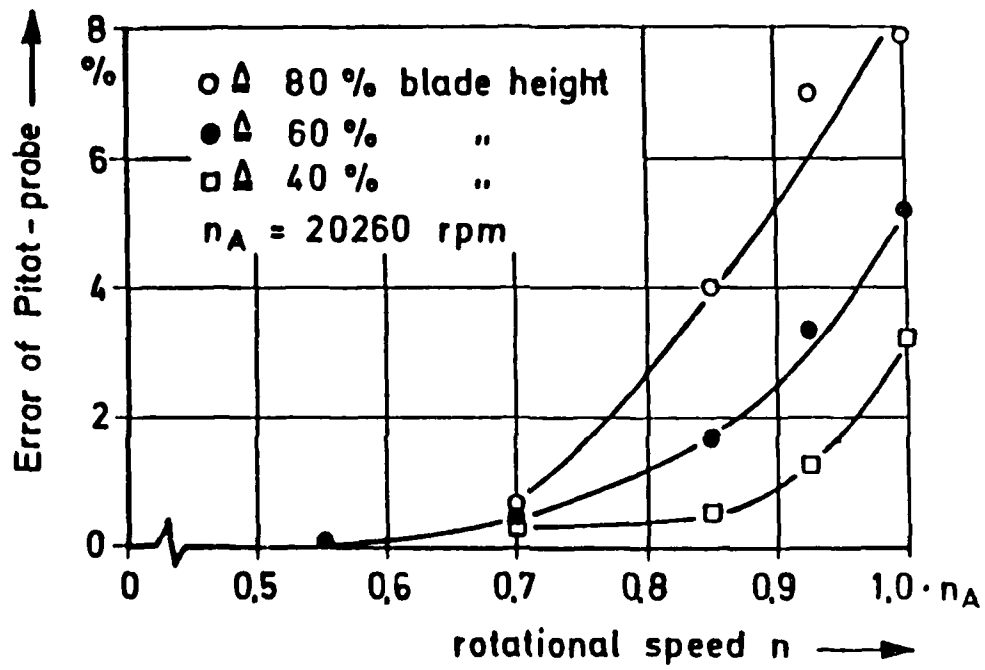
Figure 4-26: Error of Conventional Pitot-Probe Measurement
a Quarter of Chord Downstream of a Transonic
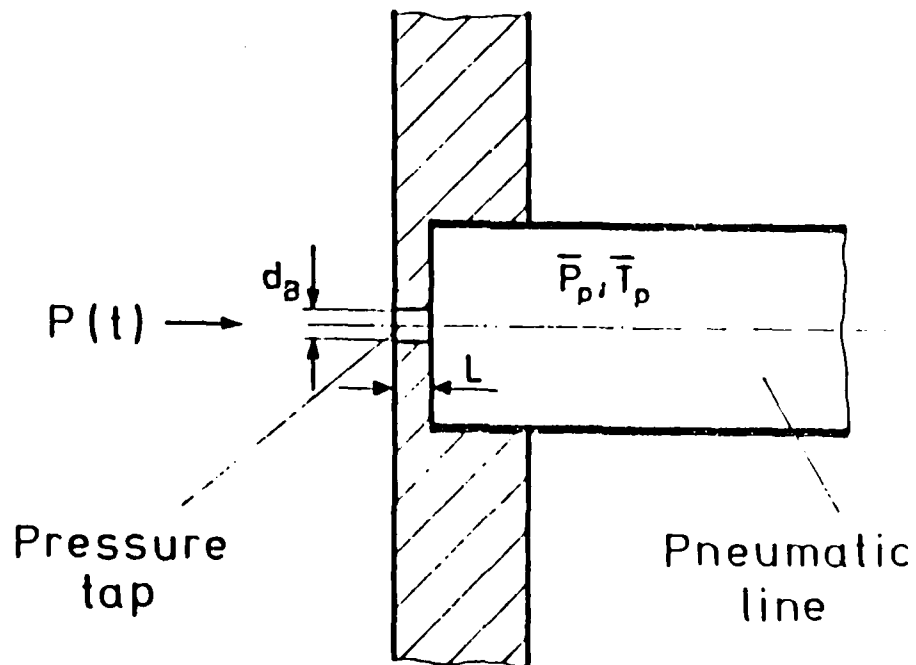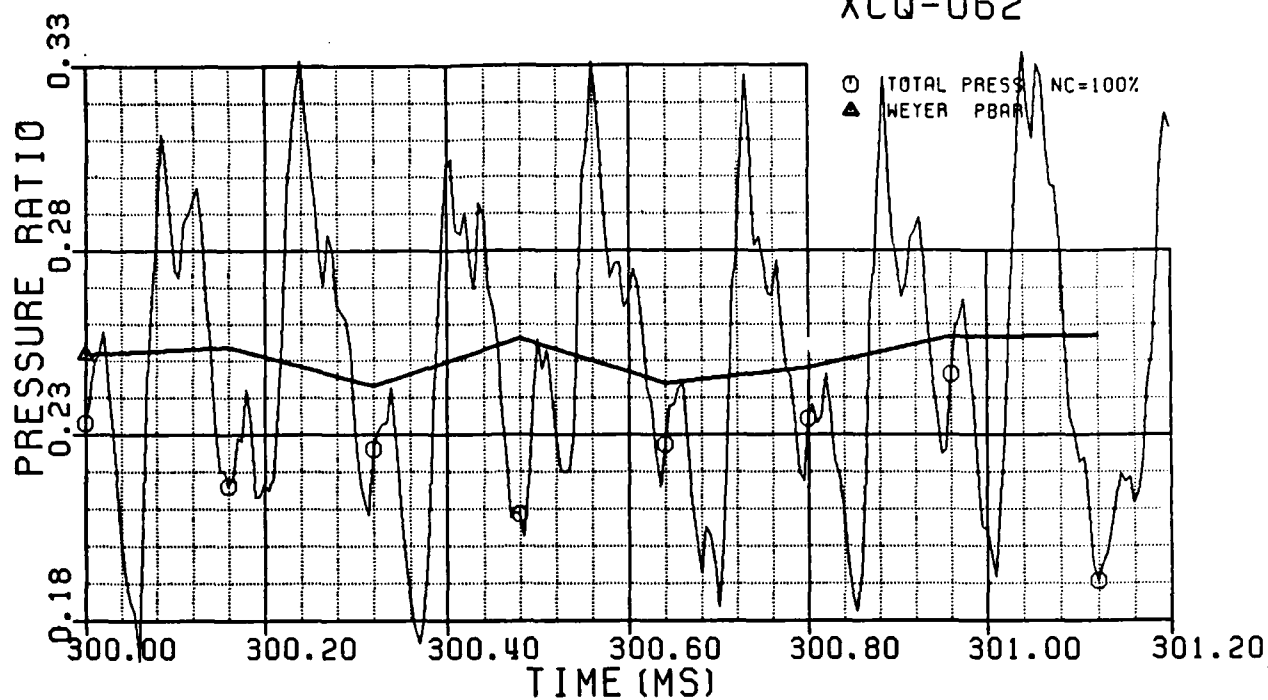Axial Compressor Rotor (from [33])

Figure 4-27: Sketch of Conventional Pressure Probe Tap and Pneumatic Line as Modeled by Weyer (from [33])
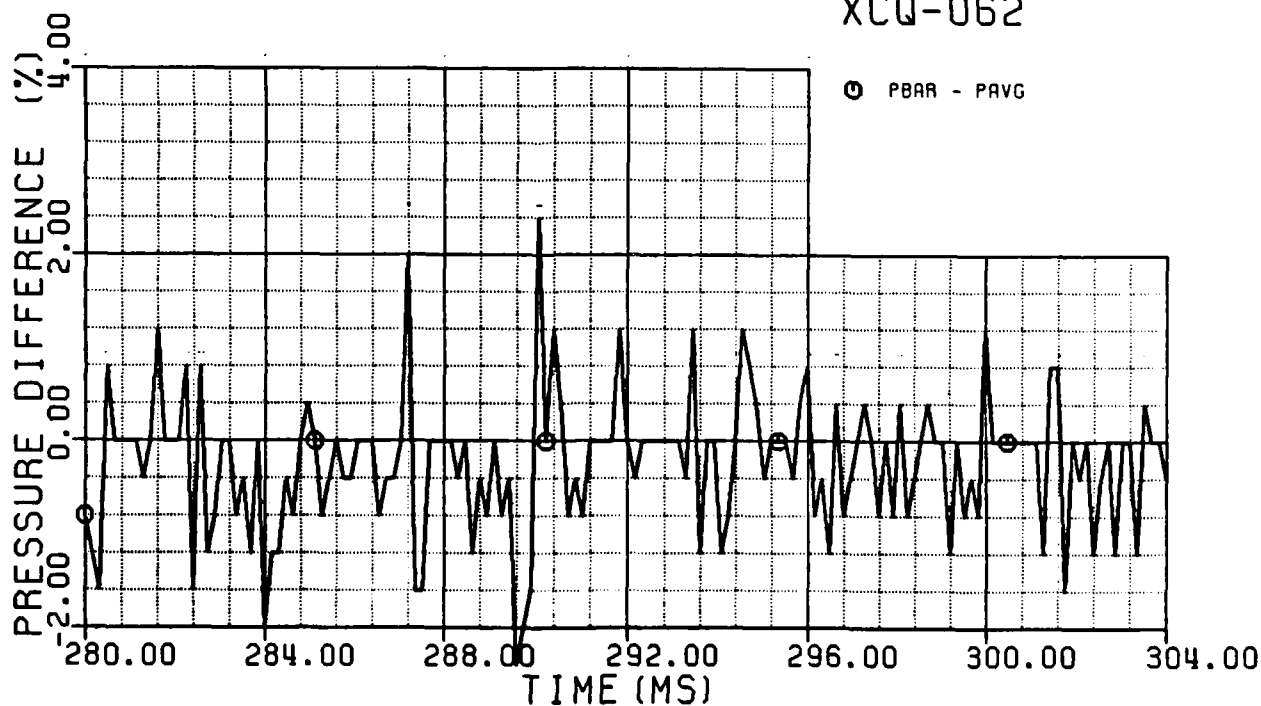
XCQ-062

XCQ-062

Figure 4-28: A) Total Pressure Ratio and PBAR (Weyer Time Average) Versus Time; B) Percent Difference Between PBAR and Time Averaged Pressure
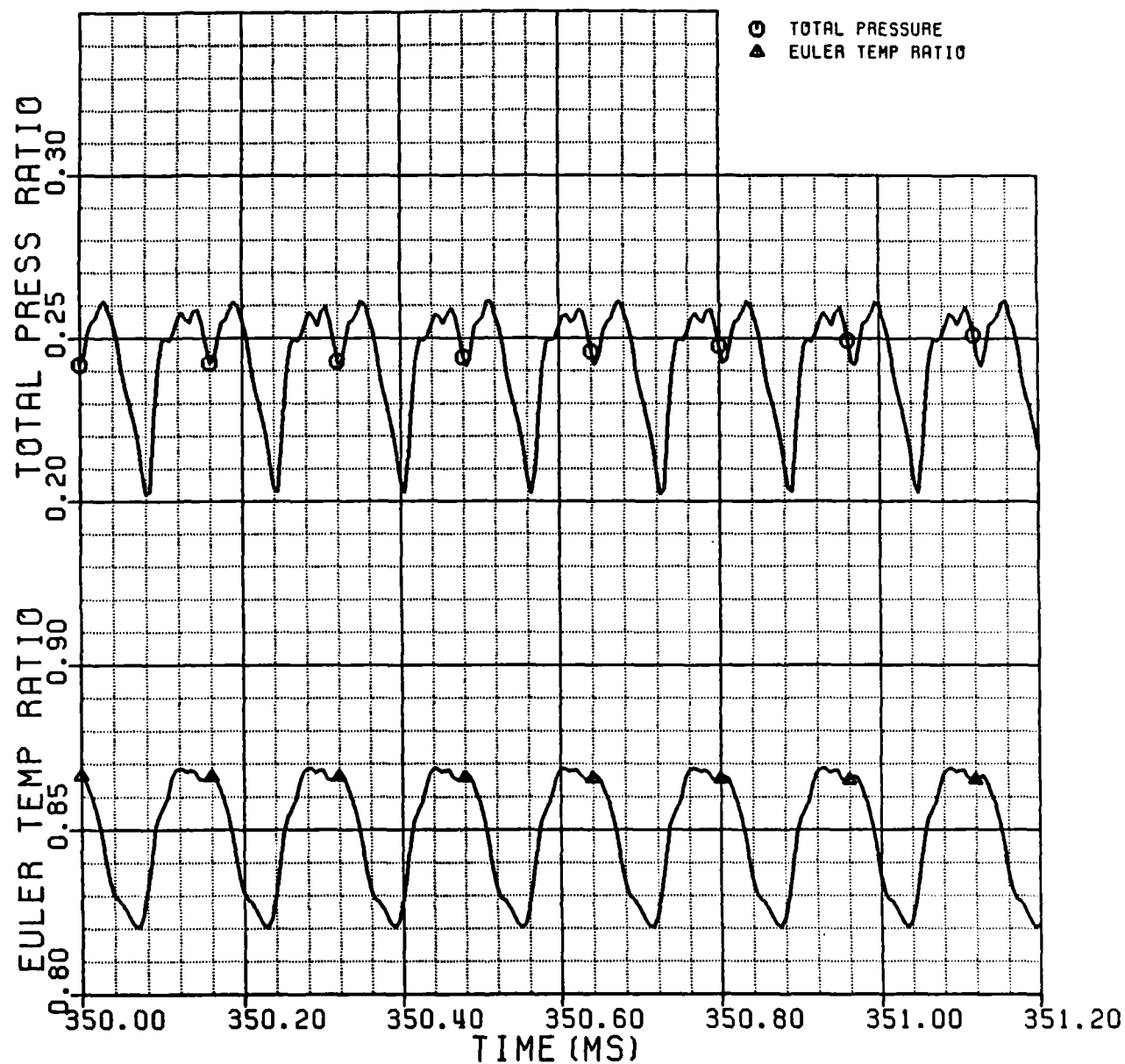
NC = 100%

Figure 4-29: Euler Temperature Ratio and Total Pressure
             Ratio Versus Time

END

FILMED

10-85

DTIC